Molecular Dynamics Studies on Structure and Phase Transitions of Nanoconfined Water

Inaugural-Dissertation

to obtain the academic degree
Doctor rerum naturalium (Dr. rer. nat.)

submitted to
The Department of Biology, Chemistry and Pharmacy
of Freie Universität Berlin

by
SHUJUAN LI
from SHANDONG, CHINA

2019

This work was prepared under supervision of

PD. DR. BURKHARD SCHMIDT (FREIE UNIVERSITÄT BERLIN)

from

OCTOBER 2011 UNTIL JULY 2019

1. Gutachter	PD.DR. BURKHARD SCHMIDT
2. Gutachter	PROF. DR. BEATE PAULUS
Date of Defense	July 10^{th}, 2019

Abstract

The properties of nanoconfined water are studied systematically with respect to three novel and important aspects. First, we derive accurate Lennard-Jones (LJ) potential models for the interaction between water and carbon sheets of different curvature. Second, we investigate the intriguing quasi—one—dimensional (quasi—1D) water in single-walled carbon nanotubes (CNTs). Third, we study the behavior of quasi—two-–dimensional (quasi—2D) water in graphene nanocapillaries. We obtain several novel phase transitions from one ice structure to another, by combining enhanced sampling strategies with mulecular dynamics (MD) simulations. These simulations are performed with more attractive and anisotropic LJ potentials of water—carbon interaction than the potentials that are used in the literature.

In the first part, we develop two sets of simple and reliable LJ parameters. They are derived from high—level ab initio quantum chemistry calculations of water interacting with CNTs. These LJ models are used for calculating the water adsorption energies of the water that is inside and outside the CNTs of different curvatures. These adsorption energies display a different curvature dependence, depending on the water that is inside and outside the CNTs. These LJ models can also be used to carry out a series of MD investigations on water confined inside CNTs and graphene capillaries.

After summarizing the necessary theoretical background, the second part of this thesis thoroughly explores the water occupancy and dynamic properties of water confined in CNTs for various force fields, using MD methods. Quasi—1D water chains and single—walled ice nanotubes (INTs) are found inside the CNTs (n, n) with $5 \leq n \leq 10$. The arrangement of water is analyzed by investigating its hydrogen bond patterns and proton–ordering with replica–exchange molecular dynamics (REMD) simulations. Second—order phase transitions from one ice structure to another, e.g., helix—helix and helix—prism transitions, are reported. These transitions change not only the arrangements of the hydrogen-–bonding patterns but also the proton ordering. Melting–like first—order phase transitions are presented as well.

In the third part, we study water confined between fixed graphene nanocapillaries at a distance of 0.65 nm with REMD simulations. Different minimum energy structures of quasi—2D ice are characterized by the networks of the oxygen atoms, partly with ferroelectric, ferrielectric and antiferroelectric proton ordering. Different phase transitions between these structures are found in our REMD simulations. We present a systematic study of this behavior using different water force fields, i.e., SPCE, TIP3P, TIP4P, TIP4P/ICE, TIP5P.

Kurzzusammenfassung

Die Eigenschaften von Wasser in Nanostrukturen werden systematisch in Bezug auf drei neue und wichtige Aspekte untersucht. Erstens leiten wir genaue Lennard-Jones (LJ) Potenzialmodelle für die Interaktion zwischen Wasser und Kohlenstoffschichten unterschiedlicher Krümmung her. Zweitens untersuchen wir quasi-eindimensionales (quasi-1D) Wasser in einwandigen Kohlenstoff-Nanoröhrchen (CNTs). Drittens studieren wir das Verhalten von quasi-zweidimensionalem (quasi-2D) Wasser in Graphen-Nanokapillaren. Dabei beobachten wir mehrere neue Phasenübergänge von einer Eisstruktur zur anderen, indem wir verbesserte Samplingstrategien mit Moleküldynamik-Simulationen (MD) kombinieren. Diese Simulationen werden mit attraktiveren und anisotroperen LJ-Potentialen der Wasser-Kohlenstoff-Interaktion durchgef—"uhrt als bisher in der Literatur verwendet wurden.

Im ersten Teil entwickeln wir zwei Sätze von einfachen und zuverlässigen LJ-Parametern. Sie stammen aus quantenchemischen ab-initio-Berechnungen von Wasser in Interaktion mit CNTs. Diese LJ-Modelle werden verwendet, um die Adsorptionsenergien von Wasser außerhalb und innerhalb von CNTs verschiedener Krümmungen zu berechnen. Diese Adsorptionsenergien zeigen innerhalb bzw. außerhalb der Röhrchen eine unterschiedliche Abhängigkeit von der Krümmung. Mit diesen LJ-Modellen können auch eine Reihe von MD-Untersuchungen an Wasser durchgeführt werden, das in CNTs und Graphenkapillaren eingeschlossen ist.

Nach der Zusammenfassung des notwendigen theoretischen Hintergrundes, erforscht der zweite Teil dieser Arbeit die dynamischen Eigenschaften von Wasser in CNTs für verschiedene Kraftfelder mit MD-Methoden. Quasi-eindimensionale Wasserketten und einwandige Eis-Nanoröhrchen (INTs) finden sich in den CNTs (n, n) mit $5 \leq n \leq 10$. Die Anordnung der Wasserteilchen wird durch Untersuchung seiner Wasserstoffbindungsmuster und Protonenanordnung mit Replikat-Austausch-Moleküldynamik (REMD)-Simulationen analysiert. Phasenübergänge zweiter Ordnung von einer Eisstruktur zur anderen, z.B. Helix-Helix- und Helix-Prisma-Übergänge, werden dokumentiert. Diese Übergänge verändern nicht nur die Anordnung der Wasserstoffbindungsmuster, sondern auch die Protonenanordnung. Schmelzartige Phasenübergänge erster Ordnung werden ebenfalls präsentiert.

Im dritten Teil untersuchen wir Wasser, das zwischen festen Graphen-Nanokapillaren in einem Abstand von 0,65 nm eingeschlossen ist, mit REMD-Simulationen. Unterschiedliche energieminimierende Strukturen quasi-zweidimensionalen Eises sind durch die Netzwerke der Sauerstoffatome charakterisiert, teilweise mit ferroelektrischer, ferrielektrischer oder antiferroelektrischer Protonenanordnung. Unterschiedliche Phasenübergänge zwischen diesen Strukturen finden sich in unseren REMD-Simulationen. Wir präsentieren eine systematische Untersuchung dieses Verhaltens mit verschiedenen Wasserkraftfeldern, z.B. SPCE, TIP3P, TIP4P, TIP4P/ICE, TIP5P.

Contents

List of Publications **xi**

1 Introduction **1**

2 Theoretical Background **7**
2.1 Ensemble Theory and Partition Function . . . 7
2.2 Molecular Dynamics Simulations . . . 9
2.2.1 Time Integration Algorithms in MD . . . 10
2.2.2 The Ergodic Hypothesis . . . 10
2.2.3 Replica–Exchange Molecular Dynamics Simulations . . . 11
2.2.4 Force Field . . . 12
2.2.5 Thermostat and Barostat . . . 14
2.2.6 Periodic Boundary Condition . . . 15
2.3 Setup of the Simulations . . . 15
2.3.1 MD Simulations of Water Filling . . . 15
2.3.2 REMD Simulations of Confined Water . . . 16
2.3.3 Energy Minimization . . . 17

3 Publications **19**
Paper A1 . . . 21
Paper A2 . . . 31
Paper A3 . . . 47

4 Summary **91**

5 Outlook **103**

Bibliography **105**

Acknowledgement **119**

List of Publications

Potential Models

Paper A1 Shulai Lei, Beate Paulus, Shujuan Li, and Burkhard Schmidt

"Curvature–Dependent Adsorption of Water Inside and Outside Armchair Carbon Nanotubes"

J. Comput. Chem. **37**, 1313–1320 (2016)

DOI: 10.1002/jcc.24342

Water inside CNTs

Paper A2 Shujuan Li, Burkhard Schmidt

"Molecular dynamics simulations of proton-ordered water confined in low-diameter carbon nanotubes"

Phys. Chem. Chem. Phys. **17**, 7303–7316 (2015)

DOI: 10.1039/c5cp00236b

Water inside Graphene Sheets

Paper A3 Shujuan Li, Burkhard Schmidt

"Replica Exchange MD Simulations of Two–Dimensional Water in Graphene Nanocapillaries: Rhombic Versus Square Structures, Proton Ordering, and Phase Transitions"

Phys. Chem. Chem. Phys.

under review

Chapter 1

Introduction

Water is ubiquitous on earth, and there is no doubt that it is one of the most essential substance that exists on our planet. Water shows anomalies in almost all of its thermodynamic properties, among which the most widely known ones are its high heat capacity and its density anomalies. These anomalies not only make water unique but also have crucial real-world impacts. For instance, water covers 70% of the earth surface and its high heat capacity plays an important role in balancing the temperature on the earth. As far as its density anomaly is concerned, the density of water achieves a maximum at a temperature of 4°C,[1] which is in contrast to most liquids that exhibit monotonous increase of density with decreasing temperature. In scientific community, it is widely believed that these features can be attributed to the formation of hydrogen bonds. However, a full understanding of the formation of these features is still not available, even if much research effort has been denoted to studying water both experimentally and theoretically. As another interesting phenomenon related to water, we know that when water freezes it forms ice. A less known fact is that different kinds of ice structures can be obtained by freezing water under different pressure and temperature conditions. The familiar ice (structure) Ih is just one of at least 17 crystalline phases[2, 3] depending on the way the ice crystals are arranged.

Due to the rapid advancement of nanotechnology, the study of the low–dimensional ice–like structures of water, when it is confined in nanocapillaries or adsorbed at nanointerfaces, has gained more and more research attentions in recent years. It has been noticed that, when water is confined in nanometer scale, its phase behavior becomes significantly different from its bulk counterpart, which often leads to much richer phenomena. Understanding the novel properties and the mechanisms that are responsible for the unusual properties of water at nanoscale can help us not only understand the functioning of biological systems,[4, 5] but also provide the theoretical foundation for the development of nanoscale electronic devices.[6–10]

While a number of experimental techniques have been developed and been used to study the nano–confined ice, detailed investigation for the dynamical behavior of the metastable structures of

nanoconfined ice requires high resolution of the dynamics and therefore is still a very challenging task in experiment. With the enhancement of computers and the development of computational methods, computational approaches, i.e., MD simulation methods, have been applied to the study of nanoconfined water. The MD simulation treats atoms and molecules as particles and inspects their dynamic properties on femtosecond and atomic level.

The first goal of this thesis is to gain accurate Lennard-Jones (LJ) parameters for water and carbon materials. In MD simulations, these parameters appear in the LJ potentials which are widely used in modeling the non–bonded water–carbon interactions. In previous studies, empirical force fields are widely used in MD simulations of water in CNTs. which typically involve a large number of particles. Thanks to the computational simplicity of empirical force fields, they are made available in most of the MD software packages, *e.g.*, the OPLS-AA force field[11, 12] implemented in the GROMACS program package,[13–15] providing an efficient way to simulate systems even with millions of atoms. However, there are large discrepancies in the values of the empirical LJ parameters that have been used in previous studies of water confined in CNTs. In fact, already in one of the first simulation studies of water conduction in CNTs, it has been noticed that small changes in modeling the nanotube–water interaction can induce large differences in the water occupancy, as well as in the water filling kinetics and thermodynamics. What is more, both the structure and the dynamics of ice nanotubes confined inside CNTs were found to be sensitively dependent on the parameters of LJ potentials. These studies indicate that obtaining quantitatively correct values of these parameters is crucial in MD simulations. As an alternative approach, density functional theory (DFT) can be used to fit the LJ parameters, by applying it to the interaction of water with CNT systems.[16] However, they may be unreliable, due to problems related to quantitatively description of the van der Waals (vdW) dispersion interaction.

With the recent advances in computational resources, paralleled by the progresses in the developments of methods and algorithms, high–level quantum chemical methods have become available, even for rather complex systems, such as the ones studied in paper A1. As pointed out in paper A1, to the best of our knowledge, until recently there are few high level *ab initio* results for the interaction of water with CNT systems. Only density functional theory (DFT) results exist.[16] Hence, we recently started to investigate these systems at a highly accurate quantum–chemistry level, namely an incremental density-fitting local coupled cluster treatment with single and double excitations and perturbative triples (DF-LCCSD(T)), investigating the curvature dependent adsorption properties of a water molecule inside and outside (n, n) CNT (n=4, 5, 6, 7, 8, 10) fragments. In order to save computational effort and to be able to treat even larger systems, the focus of this work is on a comparison of the computationally very demanding DF-LCCSD(T) method with different, less expensive methods: (a) the

computationally cheaper dispersion corrected DFT variants which are, however, not systematically improvable as the CCSD(T) method and (b) even cheaper LJ force fields for classical MD simulations for larger CNTs, thus bridging the gap between CNTs of increasing radius and flat graphene sheets.

It should be noted that, The uniqueness of low-dimensional materials is particularly distinguished from bulk materials. Nanotubes (NTs), especially, the carbon nano-tubes (CNTs) have aroused a widespread concern since their discovery in 1991[17] due to their particular structure and electronic nature.[18–20] Physicists, chemists and material scientists are curious in exploiting potential application for CNTs as nanoscale electronic devices; nanofluidic devices, *e.g.*, filters;[21–23] molecular channels conducting water,[24–30] protons, ions, polymers, and nucleic acids.

Although, the CNT is hydrophobic, regarding the first report from Hummer et al.,[24] it can absorb water molecules. On the first hand, water molecules adopt novel exotic properties inside the CNTs that differ from those of the bulk. Great progress has been made in understanding them. Like limited experimental studies have made some progress, see e.g. Refs.[31–40] There is, however, an extensive body of theoretical investigations.[38–65] They concluded CNT can be water-permeable by a quasi one-dimensional ordered water chain.[24, 51–54] From (7,7) CNTs (diameter 0.94 nm) onwards, however, the water molecules tend to form so-called ice nanotubes (INTs), it was predicted that INTs can even exist at room temperature.[33, 58] Simulation studies produce that, INTs can be found as chiral forms, i.e., water helices [55–58, 64, 65] or as achiral forms,[56, 58, 59, 62, 66–68] i.e. stacked water polygons. Under a room temperature and pressure conditions, Mashl et.al [69] defined that water molecules inside CNT (9,9) can form 6-gon ice structure, but inside CNT (7,7), (8,8), (10,10), there are no manifest of n-gon ice structures. However, Kolesnikov et al.[31] realized water inside (10,10) can form an 8-gon ice natube (INT) and in the center of INT, there is a one-dimensional water chain. Soon after, Kolesnikov et al. concluded that there are 8-gon structure inside (9,9).[37]

Meanwhile, in order to explore a new ordered ice phase in CNT, the low-temperature/high-pressure conditions will be a good method logical option. (Bai et al.,[57] Koga et al.,[62] Luo et al.,[70] Mikami et al.,[71]) carried many investigation and achieved a variety of INTs. Such as 4-, 5- and 6-gonal INTs were observed respectively in (14,14), (15,15) and (16,16) CNTs (Koga et al.,[62]). There have been many investigations about the water structure inside the CNTs, but the results are significantly different. Wang et.al[72] believes that the difference is due to the different LJ parameter used in the simulations. Our first research work in Paper A1 analyzed the above discrepancies and derived reliable LJ parameters.

On the second hand, One more anomalous behavior of water inside CNTs is that INT has ferroelectric.[70, 73] Every water molecule carries a tiny electric field. But because water molecules usually freeze in a somewhat random arrangement, with their bonds pointing in different directions, the ice's total elec-

tric field tends to cancel out. For bulk water the concept of ferroelectricity is still elusive. Ferroelectric ice is thought to be extremely rare; in fact, scientists are still investigating whether or not pure three–dimensional ferroelectric ice exists in nature. Some researchers have proposed that ferroelectric ice may exist on Uranus, Nepture, or Pluto. While already predicted by Pauling in the 1930s,[74] there is no experimental evidence yet for the existence of ferroelectric ice XI under natural conditions on earth. However, for ice wires and ice nanotubes in the quasi-1D confinement of low-diameter carbon nanotubes (CNTs), various ferroelectric, ferrielectric and anti-ferroelectric[53, 63, 75] arrangements of water molecules could be identified in the last few years, however, only in simulations.

On the third hand, Once the large number of new topologies of INTs confined in CNTs have been explored, another main aspect of the present work is related to the phase behavior of INTs. Which of the above–mentioned water structures prevails at which temperature, and how can we characterize the phase transitions behavior between them? It is expected that the melting and freezing behavior of nanoconfined water will be qualitatively different from that of bulk water[33, 58, 62, 63, 76, 77] and comprehensively studied in the Paper A2.

Another type of carbon nano matrices is graphene that analyzed extensively for confinement in this thesis. Graphene is only an one-atom thick layer of carbon atoms of the mineral graphite. Its lattice is structured in a strictly two-dimensional honeycomb grid. Previous to 2004, scientific community generally considered that such a strict two-dimensional layer is extremely unstable due to the existence of thermodynamic fluctuations at a finite temperature. However, this attitude has fundamentally changed with the discovery of the graphene experimentally by Andre Geim research group of the University of Manchester. Thanks to this finding, Andre Geim was awarded the prestigious Nobel Prize in Physics in 2010 jointly with Konstantin Novoselov. As the mother of CNTs and fullerene materials, graphene provides a broad prospects for applications. It is commonly known that CNTs and fullerene are all rolled from graphene.

As talked about water inside CNTs, we already know that low-dimensional water in nanoscale confinement exhibits profound differences both in structural and dynamic properties compared with bulk water and great progress has been made in understanding them. While experimental studies are still not much for quasi–2D water locked between two parallel plates comprising of graphene or other materials,[78–82] but there is a growing interest in theoretical investigation[83–118].

Our work in paper A3 is motivated by a recent high-resolution electron miscroscopy imaging study by Algara-Siller et al. who found a strictly square ice lattice which is also supported by accompanying molecular dynamics (MD) simulations.[82] Subsequently, the existence of nanoconfined 'square ice' at room temperature was confirmed both by density functional theory (DFT) calculations[117, 118] and

conventional MD simulations.[108] However, in other studies of the lattice structure of quasi-2D ice alternative structures were found, e.g. flat nearly square,[106] flat rhombic,[115] puckered rhombic,[86] puckered square,[106, 108] flat hexagonal,[111] puckered nearly square,[119] and even Archimedean $4 \cdot 8^2$ tiling structures have been reported.[115]

In addition to the determination of the above structures of the oxygen ions, also the question of proton ordering of the water molecules inside graphene slit is a highly interesting topic. Our paper A3 deals with the question whether nanoconfined quasi–2D ice can also be ferroelectric for which there is indeed (limited) experimental evidence. Thin ferroelectric ice layers can be grown on platinum surfaces[120, 121] or can be found in hydration shells surrounding proteins.[122] Also an atomic force microscopy imaging study probably suggests the possibility of ferroelectric water monolayers adsorbed on mica surfaces.[123] However, there is no experimental evidence yet for ferroelectricity of water monolayers sandwiched between graphene plates. So far, ferroelectric ordering in such systems has only been reported in MD simulation studies.[86, 115]

Once the large number of new topologies of monolayer ice confined in nanocapillaries has been explored, further main aspect of the present work is related to the phase behaviour of quasi–2D water. Which of the above–mentioned water structures prevails at which temperature, and how can we characterize the phase transitions behavior between them? It is expected that the melting and freezing behavior of nanoconfined water will be qualitatively different from that of bulk water. For example, this has been shown for quasi–2D water confined inside nanocapillaries. For this case, there are different computational studies on the effect of different thermodynamic variables and for different confining surfaces.[49, 88, 92, 94, 105, 106, 108, 118] However, the effects of finite temperature on monolayer water confined between graphene sheets, in particular the nature of the underlying phase transitions, are yet to be comprehensively studied in our paper A3.

The work in paper A3 aims at a systematic study of structures of quasi–2D nanoconfined water, including proton ordering, and the corresponding phase behavior. Even though, as detailed above, there is already a substantial body of literature, a direct comparison is often not straightforward due to two different reasons. First, different values of the underlying thermodynamic parameters, such as temperature, pressure and slit width were used. Second, the simulations were often based on different force fields, both for the water–graphene and the water–water interaction. Hence, a main focus of our study will be on the effect of different force fields. For the water–graphene force field, we will use parametrizations based on high–level quantum chemical calculations, as we already did in our previous simulation studies of water in CNTs.[63, 124, 125] For the water–water force field, we will be using five standard water models, i.e. SPCE,[126] TIP3P,[127] TIP4P,[127, 128] TIP4P/ICE[129] and TIP5P.[130]

Moreover, note that all studies presented here are for water confined in between parallel graphene sheets at a distance 0.65 nm.

Finally, we mention another aspect not covered sufficiently in most of the literature on quasi–2D water. The coexistence of largely different minimum energy structures with very similar energies but very different water orientational properties (e.g. ferroelectric, ferrielectric water and antiferroelectric water structures) presents a major challenge to finite temperature MD simulations of structure and dynamics of the nanoconfined ice. This is because the various water structures are highly metastable, with high barriers that typically cannot be overcome on a nanosecond timescale in conventional MD simulations for e. g. $T = 300$ K. Hence, in order to obtain a valid sampling of configurational space, we resort here to replica-exchange molecular dynamics (REMD)[131–134] simulation techniques which are based on swapping between different temperatures simulated in parallel.

First, new effective LJ models for the water—carbon interaction are derived from high-level *ab initio* calculations of water interacting with CNTs. Furthermore, this thesis presents a critical analysis of the structure and dynamics of water confined inside single–walled carbon natubes and water confined between two parallel graphene sheets. Hydrogen bond patterns, proton ordering, and phase transitions of low–dimensional ice are emphasized. The CNTs and graphene capillaries can serve as prototypes for one-dimensional and two–dimensional molecular channel. And, the advantage and disadvantage of different force field in determining some special properties of low-dimensional water are described thoroughly.

This dissertation is structured as follows. The chapter Theoretical Background gives a brief introduction to the basic molecular dynamics concepts used in this thesis. The chapter Publications contains all the papers that have been published as part of my doctoral studies. Here, the contributions by the individual authors are clearly outlined. Finally, the central findings of all publications are summarized and put into context in the chapter Summary.

Chapter 2

Theoretical Background

This chapter provides a brief overview of the theoretical framework behind this thesis. It includes ensemble theory and partition function, molecular dynamics simulations and setup of simulations.

2.1 Ensemble Theory and Partition Function

Fenomenological thermodynamics is based on several axioms resulting from observations of nature. It provides us with many useful relations between measurable quantities of macroscopic systems, but it does not have any tool for determination of concrete values of these characteristic quantities. It considers the system as a black box without a microscopic structure. The goal of statistical thermodynamics is to determine thermodynamic quantities based on interactions between particles constituting the system.

Ensembles represent an imaginary collection of a large system in different states and specified by several different thermodynamic parameters, such as: constant number of particles (N), temperature (T), volume (V), pressure(P) and energy (E). An ensemble in statistical mechanics is a theoretical tool which is used for analyzing the evolution of a thermodynamic system. There are two broad categories of ensembles as shown following. The first category is closed system includes microcanonical (NVE), canonical (NVT) and isothermal-isobaric (NPT) ensembles. In contrast, the second category is grand canonical ensemble which is appropriate for an open system in which the number of particles can vary. Examples for the most important ensembles in statistical mechanics are given in Table 2.1, Where $\beta = \frac{1}{k_B T}$ the inverse temperature, with Boltzmann's constant k_B and temperature T. The ensemble which used in the simulation must be in the same thermodynamic conditions as real system.

In the Hamilton mechanics, an abstract space is introduced which commonly referred to as phase space Γ. Phase space specifies positions (r) and momenta (p) of all particles as coordinates, and all these coordinates connect into a curve with varying time which is called trajectory. In phase space, particles can only move by the hypersurface. The dimensionality of space Γ is $6N$ which must be

Ensemble	Constraints	Densities ρ
Microcanonical	N, V, E	$Z_{NVE}^{-1}\delta(H(r,p)-E)$
Canonical	N, V, T	$Z_{NVT}^{-1}e^{-\beta H(r,p)}$
Isothermal-Isobaric	N, P, T	$Z_{NPT}^{-1}e^{-\beta(H(r,p)+PV)}$

Table 2.1: ensembles example

very large for the molecular systems with a large N. The probability density $\rho(r,p)$ represents the probability of observing the $\Gamma = (r,p)$ state and can be normalized as follows:

$$\int dr^{3N} \int dp^{3N} \rho(r,p) = 1 \tag{2.1}$$

The ensemble average of any dynamic observable macroscopic quantity A can be obtained from the relationship:

$$\langle A \rangle_\rho = \int dr^{3N} \int dp^{3N} A(r,p)\rho(r,p) \tag{2.2}$$

Where the angled brackets denote an ensemble average. This probability depends on the energy associated with the phase point according to Boltzmann's law, which for the NVT ensemble reads:

$$\rho(r,p) = Z^{-1} e^{-H(r,p)/k_B T} \tag{2.3}$$

Where Z the system partition function is equal to the integral of the density over state space, and H is the total energy.

$$Z = \int dr^{3N} \int dp^{3N} e^{-H(r,p)/k_B T} \tag{2.4}$$

In addition, $\langle A \rangle$ is an integral over all positions and momenta and determined by the value of $\rho(r,p)$. The total energy function Hamiltonian $H(r,p)$ occurring in the definitions of the ensembles is possible to be separated into two parts, the first part is a kinetic $K(p)$, which depends only on the momenta, and the second part is potential $U(r)$ that likewise depends only on the position coordinates, which is often referred to as the force field:

$$H(r,p) = K(p) + U(r) \tag{2.5}$$

In addition, the kinetic energy is quadratic in the momenta

$$K(p) = \sum_i^N \frac{p_{ix}^2 + p_{iy}^2 + p_{iz}^2}{2m_i} \tag{2.6}$$

where m_i is the mass of particle i, p_{ix}, p_{iy} and p_{iz} are momenta of particle i in three different directions.

In the microcanonical (NVE) ensemble, all copies of the system have the same number of particles (N), the same volume (V) and the same energy (E). This is an isolated system, each microsystem shares the same fixed thermodynamic properties N, V, and E. Due to the case isolation of NVE, the microscopic state Hamilton $H(r, p)$ is conserved,[135] NVE ensemble is rarely used to simulate molecular systems. In our simulations, only NVT and NPT ensembles are chosen.

The canonical ensemble (NVT) is an idealization of a system which is allowed to interchange energy with a thermal source at constant temperature while keeping fixed the number of particles (N), the volume (V) and the temperature of the system (T). Assume the experimental system is maintained at temperature T and at a fixed number of particles in volume V. This condition can be achieved if the system is immersed in a heat reservoir of temperature T. Canonical ensemble (NVT) is very convenient for this application to simulate that experiment.

The isotherml-isobaric ensemble (NPT) is a statistical mechanical ensemble that maintains a constant temperature T, a constant pressure P. and a constant of the number of particles N. This ensemble plays an important role in chemistry due to the chemical reactions, which are usually carried out under a constant pressure condition. According to the equations 2.2 and 2.3, if we know the partition function Z corresponding to a certain ensemble, we can calculate $\langle A \rangle$ straightforwardly.

2.2 Molecular Dynamics Simulations

Estimating the partition function Z requires extensive sampling, common methods for sampling of molecular systems include but not limited to Monte Carlo (MC) [136, 137] and MD simulations [138]. However, MC is known to be inefficient for high dimensional many body systems. So, MD simulation is the most commonly used to estimate $\langle A \rangle$.

MD simulations solve the equations of motion based on the force between atoms in an initial configuration in order to find out the next configuration.[139] MD computes the movement of atoms in light of the new positions, velocities, and orientations with respect to time. Thus MD produces a series of configurations based on the initial configuration and velocities. Several numerical integration algorithms can be used to calculate the equations of motion.

The molecular dynamics simulation method is based on Newton's second law. In this method it is assumed that every particle in the system behaves like a Newtonian particle and the quantum behavior is completely ignored. This means that electronic motions [140] are not considered and electrons are assumed to remain in their ground state and adjust their dynamics instantly when atomic positions change. [140–142] Indeed, only classical mechanics are used to describe the motion of the particles. Hence, the equation of motion, $F = ma$, applies on the particles where F is the force, m is mass and a is

the particle's acceleration. Once the positions and velocities of each atom are known, the state of the system can be predicted, and new positions and velocities can be calculated. The procedure can be repeatedly, and in this way a trajectory of atomic motions is obtained. As mentioned before, there are several algorithms to solve Newton's equations of motion by integration. The verlet integrator and the leap-frog integrator are two common algorithms that are used by GROMACS software.[139, 143]

2.2.1 Time Integration Algorithms in MD

The Verlet algorithm [144] is one of the simplest algorithms and at the same time one of the best for most cases. It gives good long time accuracy at the cost of a quite poor short time accuracy which leads to shorter allowed time steps. This also implies that the velocities will be know first after the next time step is calculated.

Velocity verlet algorithm[145] is the complete form of verlet algorithm. In this algorithm both the atomic positions and velocities are calculated at the same time. In other words, positions, velocities and accelerations are obtained from the same time .

Similar to verlet algorithm, the leap-frog algorithm is also made from two steps.[11] In this algorithm, first the velocities are calculated. By using this velocity as an initial velocity we can calculate the positions. In this way, the velocities leap over the positions, and then the positions leap over the velocities.

2.2.2 The Ergodic Hypothesis

Directly integrate equation 2.4 over the high dimensional (6N) space of all positions and momenta is a formidable task. Nonetheless, according to MD simulations, we estimate the time average $\overline{A}$,

$$\overline{A} = \frac{1}{t}\int_0^\infty dt A(r(t), p(t)) \tag{2.7}$$

where t is the duration of time, sufficiently long for the system to evolve from the initial to final time to make the time average meaningful. where the positions and momenta are given as functions of time $(r(t), p(t))$. In the ensemble theory of statistical mechanics it is postulated that: *the time average* $\overline{A}$ *may be replaced by the ensemble average* $\langle A \rangle$.

$$\overline{A} = \frac{1}{t}\int_0^\infty dt A(r(t), p(t)) \tag{2.8}$$

where the positions and momenta are given as functions of time $(r(t), p(t))$. In the ensemble theory of statistical mechanics it is postulated that: *the time average* $\overline{A}$ *may be replaced by the ensemble average*

$\langle A \rangle$.

The ergodic hypothesis allows us to evaluate thermodynamic quantities of the system from the sufficiently long MD trajectory. This hypothesis can be expressed in the form of an equation,

$$\langle A \rangle_\rho = \overline{A} \tag{2.9}$$

2.2.3 Replica–Exchange Molecular Dynamics Simulations

Equations 2.8 and 2.9 indicate that to accurately estimate $\langle A \rangle$, one need to run MD simulation to infinite length. However, this is impossible. In practice, if the length of MD simulation is much longer than the slowest relaxation timescales, one can obtain a relatively accurate estimate of $\langle A \rangle$.

In this thesis, when using conventional MD simulation techniques there are insufficient sampling problems connected with the rare events[146] of transitions between metastable structures of water confined in the CNTs and graphene sheets. The limitation is due to rough energy landscapes of different metastable structures, with many local minima separated by high-energy barriers. In the past few decades methods have been developed that address the sampling problem, such as umbrella sampling, [147] replica-exchange molecular dynamics and metadynamics.[133] The enhanced sampling method - replica exchange molecular dynamics method can effectively extend the timescale, so that it improves greatly the thermodynamics and kinetics calculation ability of the molecular simulations.

This method employs independent parallel Monte Carlo random walks[137, 148, 149] between several parallel simulations carried out at different temperatures. System states, defined by positions and momenta of atoms are exchanged depending on temperature and energy differences between selected simulations. By using Monte Carlo weights to determine the probability of exchanging systems states, REMD assures that the probability of exchange is quickly determined from the system's characteristics. This approach furnishes efficient free random walks on the "replica space", namely temperature and potential energy spaces.

In analogy to conventional Metropolis Monte Carlo simulations[148] building on random walks in configuration space, the REMD algorithm represents a random walk in temperature space. The motivation is that broader sampling can be obtained at high temperatures, from where the configurations can swap to the lower temperatures. Thus, the simulated systems can overcome barriers between local minima of the energy through exchanging configurations between two neighboring temperatures.[131–133] The exchange between temperatures i and j is governed by a Metropolis-Hasting algorithm,[148] which satisfies the detailed balance condition.[133] The resulting exchange probability

given by

$$P_{ij} = \min\{1, \exp[(\beta_i - \beta_j)(U(r_i) - U(r_j)]\} \tag{2.10}$$

where $U(r_i)$ and $U(r_j)$ specify the potential energy of the configurations for the two temperatures and $\beta_{i,j} = \frac{1}{k_B T_{i,j}}$ is the inverse temperature and k_B is the Boltzmann constant.

2.2.4 Force Field

The first step in molecular dynamics simulation is to build a realistic atomistic model to evaluate the atomic interactions of a molecular system.[137, 150] In principle, accurate Hamiltonnia should be obtained according to quantum mechanics. However, this is too expensive for high dimensional many body systems. Instead, force field is a classical approximation to describe this interactions.

In the force field, the potential energy is calculated as bonded and non-bonded interactions. The non-bonded interaction only contains the pair potential and neglect three body and higher order interactions.[142, 150] The non-bonded interaction energy that reflects Van der Waals interaction and columbic interactions between electrostatic charge.

Van der Waals interactions The interaction is modeled by pairwise additive Lennard-Jones (LJ)[151] potential energy functions

$$U = 4\sum_{ij} \epsilon_{ij} \left[\left(\frac{\sigma_{ij}}{r_{ij}} \right)^{12} - \left(\frac{\sigma_{ij}}{r_{ij}} \right)^{6} \right] \tag{2.11}$$

where the attractive part varies as r_{ij}^{-6} and the repulsive part varies as r_{ij}^{-12} and where the summation extends over all atoms (i) of the water molecules and all atoms (j).

There are different ways to obtain these potentionals. These quantities can be obtained from fitting to the results from experimental measurements.[152, 153] Another way can be from the calculations of potential parameters to the results of *ab initio* or density functional theory.[124, 153]

The two sets of adjustable parameters used in thesis are chosen as follows: the collision diameters σ_{ij} are deduced from standard vdW radii: $\sigma_{CO} = 0.3157$ nm, $\sigma_{CH} = 0.2726$ nm. The well depth parameters for water-carbon were parametrized previously by fitting to CCSD(T) high level quantum calculations for the water-graphene interaction.[124, 154] In those works, the overall interaction strength (η) and the dimensionless anisotropy parameter (δ) are defined as follows:

$$\eta = \epsilon_{CO} + 2\epsilon_{CH}, \quad \delta = 1 - (\epsilon_{CO} - 2\epsilon_{CH})/\eta \tag{2.12}$$

A relatively strong water-carbon interaction, η =1 kJ/mol, and a notable anisotropy parameter $\delta = 1$

between water and carbon are used in this thesis. Those results were also confirmed by our subsequent work[125] where the overall water-carbon interaction strength and anisotropy were obtained from fitting to DF-CCSD(T) results for water interacting with CNTs.

Coulomb potential All partial charges present in a molecular system interact through a Coulomb potential U_C.

$$U_C(r_{ij}) = \frac{q_a q_b}{4\pi\varepsilon_0 r_{ij}} \tag{2.13}$$

where q_a and q_b represent the partial charges on atoms of type a and b respectively, ε_0 is the vacuum permittivity, r_{ij} is the inter-atomic distance. Coulomb potential is the long range interactions in molecular dynamics. Since Coulomb interactions decay slowly in comparison to van der Waals interactions, Coulomb force computation is the most time consuming part of the force computing process in molecular dynamics.[150]

The most simple method is the implmentation of a cut off distance which means that the forces are computing until a fixed distance afterward the interaction is neglected. Methodologies such us Ewald summation, cell multipole method[137] and particle mesh approach [155] have been studied.

Water models The water-water interaction is modeled with water models, the same rigid molecular structure is applied. However, the charge distribution is different in different models. Intuitively, the point charge of the SPC[156], SPCE[126] and TIP3P[127] models distribute on each nuclei; in TIP4P[128, 157] and TIP4PICE[129] models the negative charge is placed on fictive site towards the atom of hydrogen. In the TIP5P[130] the negative charges are situated such as to mimic the lone-pair directions. In usual MD simulations water is treated as a rigid molecule with a negative partial charge located at or close to the oxygen and with positive charges on hydrogens. A water model can be polarizable or non-polarizable; This thesis will focus on the latter. In spite of its simplicity, TIP4P describes the phase diagram of water relatively well. It was further improved and TIP4P-like family of water models now contains TIP4P/Ice,[129] developed by Vega and coworkers. The second way of development is to add additional interaction sites. In case of the TIP5P model,[130] the negative charge is situated on the lone electron pairs. As was mentioned above, TIP4P is able to reproduce the shape of the phase diagram of water including several ice phases, but it is shifted to lower temperatures by 40 K.

Obviously, the advantage of models SPC, SPCE and TIP3P can be achieved in a shorter scale of time. However, the TIP4P model could be better to describe a phase diagram than in other models. In fact for the TIP4P/ICE, the predictions for both the densities and the coexistence curves are better than for TIP4P, which previously yielded the best estimations of the ice properties. That can be come from the different force field parameters as shown in Tab. 2.2. TIP5P model reproduce the anomalous

parameters and units	SCP	SPCE	TIP3P	TIP4P	TIP5P	TIP4P/ICE
loop dipole, [debye]	2.27	2.35	2.35	2.18	2.29	2.43
r_0^{OH}, [nm]	0.1	0.1	0.09572	0.09572	0.09572	0.09572
$\angle HOH$, [deg]	109.47	109.47	104.52	104.52	104.52	104.52
ε_0,[kJ/mol]	0.6502	0.6502	0.6364	0.6485	0.6694	0.8822
σ,[nm]	0.3166	0.3166	0.3151	0.3154	0.3120	0.3167
q^O, $[e]$	-0.82	-0.8476	-0.834	0	0	0
q^H, $[e]$	0.41	0.4238	0.417	0.52	0.241	0.5897
q^M, $[e]$	0	0	0	-1.04	-0.241	-1.179
r^{OM},[nm]	0	0	0	0.015	0.07	0.0156
$\angle MOM$,[deg]					109.47	0

Table 2.2: Monomer geometry and parameters for potential functions

density maxmum at 277 K and the melting point. In addition, TIP5P can also simulate the structure and thermodynamic properties of water very effectively.

2.2.5 Thermostat and Barostat

A constant temperature simulation may be required for determining how the behaviour of the system changes according to the temperature. The temperature of the systerm is related to the time average of the kinetic energy for an unconstrained system. Thermostats are designed to help a simulation sample from the correct ensemble (i.e., NVT or NPT) by modulating the temperature of the system in some way. Another reason to simulate using a thermostat is to avoid steady energy drifts caused by the accumulation of numerical errors during MD simulations. An obvious way to alter the temperature of the system is velocity scaling.[158] One problem with this approach is that it does not allow fluctuations in temperature which are present in the canonical ensemble.

A weaker formulation of this approach is the Berendsen thermostat.[159] To maintain the temperature, the system is coupled to an external heat bath with fixed Temperature. The velocities are scaled at each step, such that the rate of change of temperature is proportional to the difference in temperature. The Berendsen weak-coupling algorithm is extremely efficient for relaxing a system to the target temperature, but once the system has reached equilibrium it might be more important to probe a correct canonical ensemble. This is unfortunately not the case for the weak-coupling scheme. Using weak coupling you get a strongly damped exponential relaxation, while the Nosé-Hoover[160, 161] approach produces an oscillatory relaxation.

Similar with the temperature coupling, the system can also be coupled to a pressure bath. Berendsen algorithm scales coordinates and box vectors every step, the extended-ensemble Parrinello-Rahman approach,[162] and for the velocity Verlet variants, the Martyna-Tuckerman-Tobias-Klein (MTTK) implementation of pressure control.[163, 164] Parrinello-Rahman and Berendsen can be combined with any

of the temperature coupling methods. MTTK can only be used with Nosé-Hoover temperature control.[163] Afterwards, it can only be used when the system does not have constraints.

2.2.6 Periodic Boundary Condition

When perform molecular dynamics simulations, finite size can cause the boundary effects. To avoid these problems, periodic boundary conditions (PBCs) are used.[165] When we want to calculate bulk gasses, liquids, crystals or mixture, PBCs are usually applied and make the system more like an infinite one. Usually, we carry on simulations on the molecular systems with a very large size. The implementation of PBCs can reduce the computational cost of a simulation.[166] In addition, a small sample size means that periodic boundary conditions are required unless special attention is paid to surface effects.

2.3 Setup of the Simulations

2.3.1 MD Simulations of Water Filling

Molecular dynamics simulations are performed to determine the number of water molecules, N_W, by using the GROMACS 4.5 software package[167] within the NPT ensemble. The equations of motion are integrated using the leap-frog algorithm with a timestep of 1 fs with periodic boundary conditions in all directions and he duration of the simulations is 10 ns with an initial equilibration period of 1 ns. LJ part of the water-water interaction a cutoff radius 0.9 nm is applied while the Coulombic part is treated by a real space cutoff at 0.9 nm and the reciprocal part is described by the Particle-Mesh Ewald (PME) method.[155, 168] The temperature $T = 300$ K is controlled by the velocity-rescale thermostat with a coupling constant $\tau = 0.2$ ps[169] and the pressure $P = 1$ bar is controlled by the pressure coupling Berendsen barostat[159] which is isotropic in X, Y and Z direction. For water inside CNTs, nine different CNTs were investigated simulataneously in one (periodic) simulation box of $14 \times 14 \times 20$ nm^3 which is large enough to safely neglect interaction between the CNTs. The length of the armchair CNTs (n, n) is 10.07 nm (41 unit cells of $\sqrt{3}a = 245.6$ pm each), whereas the length of the zigzag CNTs $(n, 0)$ is 10.21 nm All tested CNTs are kept frozen during these simulations and the internal coordinates of water molecules are constrained by the SETTLE algorithm.[170]

Second for water inside graphene, the distance h between the graphene planes is 0.65 nm allowing one mono-layer of water to be accommodated within the capillary. 2000 water molecules in the two sides of a simulation box separated by two graphene walls. The cross section of the simulation box is given by $l_x = 3.689$ nm, and $l_y = 4.626$ nm and its length is initially $l_z = 8.032$ nm. During the initial

equilibration period of 5 ns, the desired temperature, $T = 300$ K, is controlled by the velocity-rescaling thermostat with a coupling constant of $\tau = 0.2$ ps[169] and the pressure, $P = 0.1$ MPa or $P = 1000$ MPa, is controlled by the pressure coupling Berendsen barostat[159] acting along the z direction. This choice of thermostat/barostat provides an efficient means to reach a stable state at the beginning of a run. During the subsequent production run of another 5 ns length, the temperature is controlled by the Nosé-Hoover thermostat with a coupling constant $\tau = 0.2$ ps[160, 161] and the pressure is controlled by the pressure coupling Parrinello-Rahman barostat[157, 162] which are known to yield more stable NPT conditions than the velocity-rescaling thermostat and the Berendsen barostat, respectively.

2.3.2 REMD Simulations of Confined Water

REMD simulations are carried out within the NVT ensemble, with constant number of water molecules in the capillary, N_W, taken from the MD filling simulations as described above. The temperature, $T = 300$ K, is controlled by the velocity-rescaling thermostat. The size of the nanocapillary area is 5.964 nm $\times$ 5.658 nm.

Our REMD simulations are performed using MPI GROMACS 5.0[167] in an NVT ensemble. The N_T temperatures are distributed exponentially according to

$$T_i = T_0 e^{ki}, \quad 0 \leq i \leq N_T \tag{2.14}$$

where the temperatures range between $T_{min} = T_0$ and $T_{max} = T_0 e^{kN_T}$ and where the parameter k can be tuned to obtain temperature intervals allowing for sufficient acceptance probabilities P_{ij} which should be typically within $0.2 \ldots 0.3$.[167] In some cases, however, it proved necessary to manually adjust the temperatures to meet this requirement. In our simulations of water confined in CNTs and graphene nanocapillary, the temperature distributions are ranging from $T_{min} = 200$ K, where all the water structures are practically frozen, to different $T_{max} \approx 600$ K where replicas are not trapped in local energy minima anymore. The number of temperatures, N_T, depends on the acceptance probabilities.

In practice, the REMD scheme is initialized by running conventional MD simulations of 1 ns length, to achieve equilibration for each of the temperatures separately. Then short REMD simulations (100 ps) were carried out to validate the acceptance probability between adjacent replicas and/or to calibrate the above parameter k where exchanges are attempted every 1 ps. Afterwards, long REMD simulations (with a total length of 20 ns) are performed which are the basis of our analyis.

2.3.3 Energy Minimization

This section is concerned with energy minimization of water that is confined within CNTs and graphene sheets. In order to sample the multitude of local minima of the high-dimensional potential energy landscape, the study performed a steepest decent algorithm that is implemented in the GROMACS 5.0 software packag. [167] The structures of water inside CNTs and water in between graphene sheets are initialized from their snapshots of REMD trajectories. These calculations performe within the NVT ensemble and with periodic boundary conditions along CNTs and the ice plane, respectively.

Chapter 3

Publications

The following chapter contains the scientific papers published in the context of this thesis. These publications are ordered thematically, belonging to three main topics: the use of DF–LCCSD(T) results to parameterize LJ force fields for the interaction of water both with the inner and outer sides of CNTs and with graphene representing the zero curvature limit; the investigation of quasi– 1D water in carbon nanotubes and the investigation of quasi–2D water in graphene nanocapillaries. For each publication, the contributions by the individual authors are outlined.

Paper A1

"Curvature–Dependent Adsorption of Water Inside and Outside Armchair Carbon Nan–otubes"

Shulai Lei, Beate Paulus, Shujuan Li, and Burkhard Schmidt

J. Comput. Chem. **37**, 1313-1320 (2016)

DOI: 10.1002/jcc.24342

URL: http://dx.doi.org/10.1002/jcc.24342

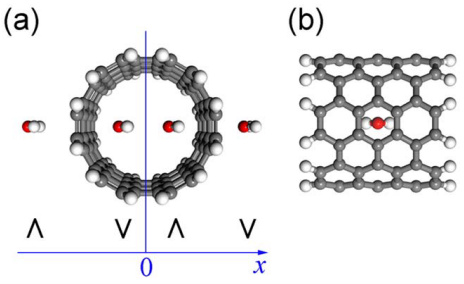

Figure 3.1: Adsorption structures of a water molecule inside and outside a (6,6) CNT fragment

Author's contributions

The idea behind this work on the curvature dependence of the physisorption properties of a water molecule inside and outside an armchair carbon nanotube (CNT) was conceived by Beate Paulus and Burkhard Schmidt. Shulai Lei performed quantum chemical calculations using an incremental density–tting local coupled cluster treatment with single and double excitations and perturbative triples (DF–LCCSD(T)) study.

I used the DF–LCCSD(T) results to parameterize Lennard–Jones (LJ) force fields for the interaction of water with the inner and outer sides and with graphene representing the zero curvature limit. The graphical representation of those results was done by Shulai Lei and myself. The first part of the manuscript that (DF–LCCSD(T)) study was written by Shulai Lei and Beate Paulus; the second part of Lennard-Jones (LJ) force fields fitting was written by Burkhard Schmidt and Shujuan Li. All coauthors contributed to the final version of this manuscript.

Paper A2

"Molecular dynamics simulations of proton–ordered water confined in low–diameter carbon nanotubes"

Shujuan Li, and Burkhard Schmidt

Phys. Chem. Chem. Phys. **17**, 7303-7316 (2015)

DOI: 10.1039/c5cp00236b

URL: http://dx.doi.org/10.1039/C5CP00236B

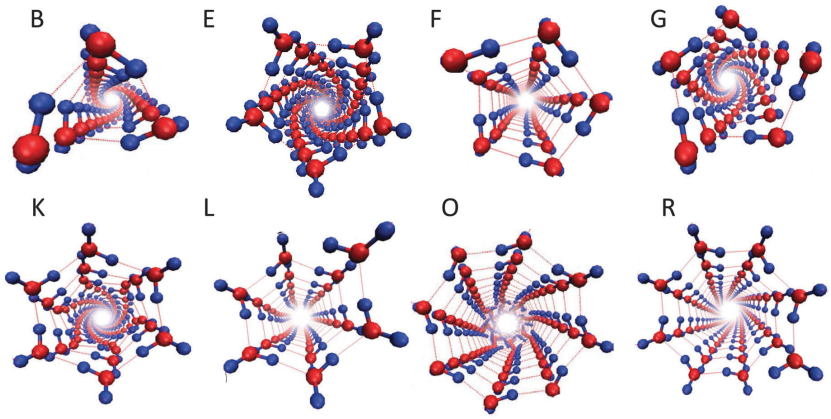

Figure 3.2: End views of selected minimum energy structures of INTs confined inside low diameter CNTs.

Author's contributions

The main idea of this work and the methodology were conceived by Burkhard Schmidt. I did all the MD calculations and prepared a preliminary text on the results as well as figures to visualize those results. Burkhard Schmidt and I equally contributed to the final implementation of the methodology and the preparation of the results. The manuscript was written by Burkhard Schmidt and myself.

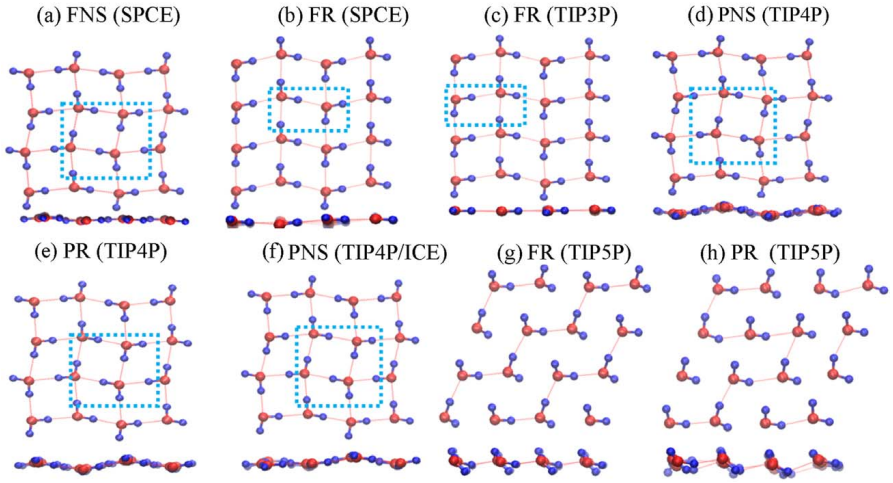

Figure 3.3: Minimum energy structures of water confined inside a graphene nanocapillary for various water models indicated in brackets.

Paper A3

"Replica Exchange MD Simulations of Two–Dimensional Water in Graphene Nanocapillaries: Rhombic Versus Square Structures, Proton Ordering, and Phase Transitions"

Shujuan Li, and Burkhard Schmidt

Phys. Chem. Chem. Phys.

under review

Author's contributions

The project was initially conceived by Burkhard Schmidt and myself. Burkhard Schmidt proposed the preliminary ideas of simulating water confined inside graphene. I implementated this idea, performed the extensive molecular dynamics simulations and replica–exchange molecular dynamics simulations, and prepared the figures for visualizing the results. The introduction and discussion sections in the manuscript were written by myself with significant modification from Burkhard Schmidt; the conclusion section of the manuscript was written by Burkhard Schmidt.

Replica Exchange MD simulations of Two–Dimensional Water in Graphene Nanocapillaries: Rhombic Versus Square Structures, Proton Ordering, and Phase Transitions

Shujuan Li and Burkhard Schmidt

Institute for Mathematics, Freie Universität Berlin

Arnimallee 6, D-14195 Berlin, Germany

(Dated: June 3, 2019)

Abstract

Hydrogen bond patterns, proton ordering, and phase transitions of monolayer ice in two-dimensional hydrophobic confinement are fundamentally different from those found for bulk ice. To investigate the behavior of quasi–2D ice, we perform molecular dynamics simulations of water confined between fixed graphene plates at a distance of 0.65 nm. While experimental results are still limited and theoretical investigations are often based on a single, often empirically based force field model, this work presents a systematic study modeling the water–graphene interaction by effective Lennard-Jones potentials previously derived from high–level ab initio CCSD(T) calculations of water adsorbed on graphene [Phys. Chem. Chem. Phys. **15**, 4995 (2013)]. For the water–water interaction different water force fields, i. e. SPCE, TIP3P, TIP4P, TIP4P/ICE, TIP5P, are used. The water occupancy of the graphene capillary at a pressure of 1000 MPa is determined to be between 13.5 and 13.9 water molecules per square nanometer, depending on the choice of the water force field. Based on these densities, we explore the structure and dynamics of quasi–2D water for temperatures ranging from 200 K to about 600 K for each of the five force fields. To ensure complete sampling of the configurational space and to overcome barriers separating metastable structures, these simulations are based on the replica exchange molecular dynamics technique. We report different tetragonal hydrogen bond patterns which are classified as nearly square or as rhombic. While many of these arrangements are essentially flat, in some cases puckered arrangements are found, too. Also the proton ordering of the quasi-2D water structures is considered, allowing to identify them as ferroelectric, ferrielectric or antiferroelectric. For temperatures between 200 K and 400 K we find several second–order phase transitions from one ice structure to another, changing in many cases both the arrangements of the oxygen atoms and the proton ordering. For temperatures between 400 K and 600 K there are melting–like transitions from a monolayer of ice to a monolayer of liquid water. These first–order phase transitions have a latent heat between 3.4 and 4.0 kJ/mol. Both the values of the transition temperatures and of the latent heats display considerable model dependence for the five different water models investigated here.

I. INTRODUCTION

Understanding the structure and phase behavior of water is of great interest due to its extraordinary properties and ubiquitous existence in our daily life. Under different conditions of pressure and temperature, bulk water can form numerous crystal structures, with the familiar ice Ih being just one of at least 17 crystalline phases [1, 2]. Less obvious are the low–dimensional ice–like structures of water confined in nanocapillaries or adsorbed at nanointerfaces which is a subject of considerable scientific interest due to important implications on biological systems, geological systems, and nanotechnological application [3–7]. Low-dimensional water in nanoscale confinement exhibits profound differences both in structural and dynamic properties compared with bulk water and great progress has been made in understanding them. While experimental studies are still rare, see e. g. work on one dimensional confined water [8–17], and two dimensional confined water [18–22], there is an extensive body of theoretical investigations. One part of these simulation studies is devoted to quasi–1D water confined in low–diameter nanotubes or other nanopores [23–38], while another part is concerned with quasi–2D water locked between two parallel plates comprising of graphene or other materials [39–75].

This work presents a computational study of the structure and dynamics of monolayer (quasi-2D) water confined between two parallel graphene sheets, a prototypical model system for hydrophobic confinement. It is motivated by a recent high-resolution electron miscroscopy imaging study by Algara-Siller et al. who found a strictly square ice lattice which is also supported by accompanying molecular dynamics (MD) simulations [22]. Subsequently, the existence of nanoconfined 'square ice' at room temperature was confirmed both by density functional theory (DFT) calculations [73, 74] and conventional MD simulations [64]. However, in other studies of the lattice structure of quasi-2D ice alternative structures were found, e. g. flat nearly square [62], flat rhombic [71], puckered rhombic [42], puckered square [62, 64], flat hexagonal [67], puckered nearly square [76], and even Archimedean $4 \cdot 8^2$ tiling structures have been reported [71].

In addition to the determination of the above structures of the oxygen ions, also the question of proton ordering or the orientation of the permanent dipole moments of the water molecules is a highly interesting topic. For bulk water the concept of ferroelectricity is still elusive. While already predicted by Pauling in the 1930s [77], there is no experimen-

tal evidence yet for the existence of ferroelectric ice XI under natural conditions on earth. However, for ice wires and ice nanotubes in the quasi-1D confinement of low-diameter carbon nanotubes (CNTs), various ferroelectric, ferrielectric and anti-ferroelectric [28, 38, 78] arrangements of water molecules could be identified in the last few years, however, only in simulations. The present work deals with the question whether nanoconfined quasi–2D ice can also be ferroelectric for which there is indeed (limited) experimental evidence. Thin ferroelectric ice layers can be grown on platinum surfaces [79, 80] or can be found in hydration shells surrounding proteins [81]. Also an atomic force microscopy imaging study probably suggests the possibility of ferroelectric water monolayers adsorbed on mica surfaces [82]. However, there is no experimental evidence yet for ferroelectricity of water monolayers sandwiched between graphene plates. So far, ferroelectric ordering in such systems has only been reported in MD simulation studies [42, 71].

Once the large number of new topologies of monolayer ice confined in nanocapillaries has been explored, another main aspect of the present work is related to the phase behaviour of quasi–2D water. Which of the above–mentioned water structures prevails at which temperature, and how can we characterize the phase transitions behavior between them? It is expected that the melting and freezing behavior of nanoconfined water will be qualitatively different from that of bulk water. For example, this has been shown for quasi–1D water in low-diameter CNTs [33, 37, 38] and also for quasi–2D water confined inside nanocapillaries. For the latter case, there are different computational studies on the effect of different thermodynamic variables and for different confining surfaces [24, 44, 48, 50, 61, 62, 64, 74]. However, the effects of finite temperature on monolayer water confined between graphene sheets, in particular the nature of the underlying phase transitions, are yet to be comprehensively studied in the present work.

The present work aims at a systematic study of structures of quasi–2D nanoconfined water, including proton ordering, and the corresponding phase behavior. Even though, as detailed above, there is already a substantial body of literature, a direct comparison is often not straightforward due to two different reasons. First, different values of the underlying thermodynamic parameters, such as temperature, pressure and slit width were used. Second, the simulations were often based on different force fields, both for the water–graphene and the water–water interaction. Hence, a main focus of our study will be on the effect of different force fields. For the water–graphene force field, we will use parametrizations based

on high–level quantum chemical calculations, as we already did in our previous simulation studies of water in CNTs [38, 83, 84]. For the water–water force field, we will be using five standard water models, i. e. SPCE [85], TIP3P [86], TIP4P [86, 87], TIP4P/ICE [88] and TIP5P [89]. Moreover, note that all studies presented here are for water confined in between parallel graphene sheets at a distance 0.65 nm.

Finally, we mention another aspect not covered sufficiently in most of the literature on quasi–2D water. The coexistence of largely different minimum energy structures with very similar energies but very different water orientational properties (e. g. ferroelectric, ferrielectric water and antiferroelectric water structures) presents a major challenge to finite temperature MD simulations of structure and dynamics of the nanoconfined ice. This is because the various water structures are highly metastable, with high barriers that typically cannot be overcome on a nanosecond timescale in conventional MD simulations for e. g. $T = 300$ K. Hence, in order to obtain a valid sampling of configurational space, we resort here to replica-exchange molecular dynamics (REMD) [90–93] simulation techniques which are based on swapping between different temperatures simulated in parallel.

II. SIMULATION METHODS

A. Force Fields

The water–carbon interaction is modeled by pairwise additive Lennard-Jones (LJ) potential energy functions

$$U = 4 \sum_{ij} \epsilon_{ij} \left[\left(\frac{\sigma_{ij}}{r_{ij}} \right)^{12} - \left(\frac{\sigma_{ij}}{r_{ij}} \right)^{6} \right] \tag{1}$$

where the attractive part varies as r_{ij}^{-6} and the repulsive part varies as r_{ij}^{-12} and where the summation extends over all atoms (i) of the water molecules and all atoms (j) in the graphene slab. The two sets of adjustable parameters are chosen as follows: the collision diameters σ_{ij} are deduced from standard vdW radii: $\sigma_{CO} = 0.3157$ nm, $\sigma_{CH} = 0.2726$ nm. The well depth parameters for water–carbon were parametrized previously by fitting to CCSD(T) high level quantum calculations for the water–graphene interaction [83, 94]. In those works, the overall interaction strength (η) and the dimensionless anisotropy parameter

(δ) are defined as follows:

$$\eta = \epsilon_{CO} + 2\epsilon_{CH}, \quad \delta = 1 - (\epsilon_{CO} - 2\epsilon_{CH})/\eta \tag{2}$$

A relatively strong water–carbon interaction, η =1 kJ/mol, and a notable anisotropy parameter $\delta = 1$ between water and carbon were obtained in the mentioned publications. Those results were also confirmed by our subsequent work where the overall water–carbon interaction strength and anisotropy were obtained from fitting to DF-CCSD(T) results for water interacting with CNTs [84].

For the water–water interaction, we use five different water models, namely the three–particle models SPCE and TIP3P, the four–particle models TIP4P and its variant TIP4P/ICE, and the five–particle model TIP5P.

B. MD Simulations of Water Filling a Nanocapillary

The number of water molecules, N_W, spontaneously entering a parallel graphene slit is obtained from molecular dynamics (MD) simulations for given temperature and pressure. Our MD simulation system contains 2000 molecules in the two sides of a simulation box separated by two graphene walls, see Fig. 1. The cross section of the simulation box is given by $l_x = 3.689$ nm, and $l_y = 4.626$ nm and its length is initially $l_z = 8.032$ nm. The parts are connected by a nanocapillary which consists of two parallel graphene sheets the length and width of which are 3.689 nm and 3.692 nm. The distance h between the graphene planes is 0.65 nm allowing one mono-layer of water to be accommodated within the capillary. The MD-simulations were carried out using the GROMACS 5.0.2 software package [95] within the NPT ensemble. The water–water interaction is modeled in terms of five different water models, and the water molecules and the graphene are assumed to interact through the LJ potential energy functions introduced in Sec. II A. The graphene walls as well as the nanocapillary are kept frozen during these simulations and the internal coordinates of the water molecules are constrained by the SETTLE algorithm [96].

During the initial equilibration period of 5 ns, the desired temperature, $T = 300$ K, is controlled by the velocity-rescaling thermostat with a coupling constant of $\tau = 0.2$ ps [97] and the pressure, $P = 0.1$ MPa or $P = 1000$ MPa, is controlled by the pressure coupling Berendsen barostat [98] acting along the z direction. This choice of thermostat/barostat provides

an efficient means to reach a stable state at the beginning of a run. During the subsequent production run of another 5 ns length, the temperature is controlled by the Nosé-Hoover thermostat with a coupling constant $\tau = 0.2$ ps [99, 100] and the pressure is controlled by the pressure coupling Parrinello-Rahman barostat [101, 102] which are known to yield more stable NPT conditions than the velocity-rescaling thermostat and the Berendsen barostat, respectively. The equations of motion are integrated using the leap-frog algorithm with a timestep of 1 fs with periodic boundary conditions in all directions. For the LJ part of the water–water and the water–carbon interaction a cutoff radius of 0.9 nm is applied. The Coulombic interaction of the water partial charges is treated by a real-space cutoff at 0.9 nm and the reciprocal part is treated by the Particle–Mesh Ewald (PME) method [103, 104].

In some of the simulations presented in Sec. III C, it was necessary to determine the (solid or liquid) phase of the quasi-2D ice confined in the nanocapillary. We analyzed the mobility of the water molecules by calculating the mean square displacement (MSD), i. e.,

$$\langle r^2(t)\rangle = \frac{1}{N_W}\sum_{i=0}^{N_W}\left(r_i(t) - r_i(0)\right)^2 \tag{3}$$

Here, N_W is the number of the water molecules, and $r_i(t) - r_i(0)$ is the average distance they travel in a given time t, here three nanoseconds. If the MSD grows linearly with time, its slope can be related to the self-diffusion constant D through the Einstein relation:

$$D = \frac{1}{2d}\frac{\partial}{\partial t}\langle r^2(t)\rangle \tag{4}$$

where d stands for the number of spatial dimensions, in this case two for the in-plane diffusion.

C. REMD Simulations of Confined Water

Replica exchange molecular dynamics (REMD) simulations are performed to study the structure and dynamics of water confined inside a 0.65 nm wide graphene slit, now without the surrounding water reservoirs. These simulations are carried out within the NVT ensemble, with constant number of water molecules in the capillary, N_W, taken from the MD filling simulations as described above. The force field between water and graphene is the same as in the filling simulations, see also Sec. II A. Again, we use the five different water models listed there. The temperature, $T = 300$ K, is controlled by the velocity-rescaling thermostat. The size of the nanocapillary area is 5.964 nm $\times$ 5.658 nm.

When using conventional MD simulation techniques there are sampling problems connected with the rare events of transitions between metastable structures of water confined in the graphene slit. This is illustrated here for the dimensionless polarization $\langle\mu\rangle$ which is defined as the sum of the water dipoles projected onto the graphene planes, divided by the number of water molecules, N_W, and by the dipole moment, μ_0, of a single water molecule which is 2.35 D [105], 2.35 D [89, 102], 2.18 D [89, 102, 105], 2.43 D [88] and 2.29 D [89] for the SPCE, TIP3P, TIP4P, TIP4P/Ice, and TIP5P models, respectively.

$$\langle\mu\rangle = \frac{1}{N_W \mu_0} \sum_{i=1}^{N_W} |\mu_i| \tag{5}$$

where μ_i is the dipole moment for the i-th water molecule along the graphene planes. As an example, Fig. 2 shows the time evolution of the dimensionless polarization $\langle\mu\rangle$ for 467 water molecules inside a graphene slit for $T = 300$ K simulated with the SPCE water model. Even though the simulation period is rather long (200 ns), we observe only very few transition events between various metastable water states for this trajectory. Obviously, the reason why such events are so rare is because they involve concerted rotations of many (or even all!) water molecules. Hence, it is computationally too expensive to sample the whole phase space of the system with conventional MD simulations. Instead, in the present work we make use of the REMD technique which is based on an ensemble of non-interacting MD simulations for different temperatures. In analogy to conventional Metropolis Monte Carlo simulations building on random walks in configuration space, the REMD algorithm represents a random walk in temperature space. The motivation is that broader sampling can be obtained at high temperatures, from where the configurations can swap to the lower temperatures. Thus, the simulated systems can overcome barriers between local minima of the energy through exchanging configurations between two neighboring temperatures [90–92]. The exchange between temperatures i and j is governed by a Metropolis-Hasting algorithm [106], which satisfies the detailed balance condition [92]. The resulting exchange probability is given by

$$P_{ij} = \min\{1, \exp[(\beta_i - \beta_j)(U(r_i) - U(r_j)]\} \tag{6}$$

where $U(r_i)$ and $U(r_j)$ specify the potential energy of the configurations for the two temperatures and $\beta_{i,j} = \frac{1}{k_B T_{i,j}}$ is the inverse temperature and k_B is the Boltzmann constant.

Our REMD simulations are performed using MPI GROMACS 5.0 [95] in an NVT en-

semble. The N_T temperatures are distributed exponentially according to

$$T_i = T_0 e^{ki}, \quad 0 \leq i \leq N_T \tag{7}$$

where the temperatures range between $T_{min} = T_0$ and $T_{max} = T_0 e^{kN_T}$ and where the parameter k can be tuned to obtain temperature intervals allowing for sufficient acceptance probabilities P_{ij} which should be typically within $0.2 \ldots 0.3$ [95]. In some cases, however, it proved necessary to manually adjust the temperatures to meet this requirement, see Tab. I. In our simulations of water confined in a graphene nanocapillary, the temperature distributions are ranging from $T_{min} = 200$ K, where all the water structures are practically frozen, to different $T_{max} \approx 600$ K where replicas are not trapped in local energy minima anymore. The number of temperatures, N_T, which is 28 for SPCE and 30 for the other four water models, depends on the acceptance probabilities.

In practice, the REMD scheme is initialized by running conventional MD simulations of 1 ns length, to achieve equilibration for each of the temperatures separately. Then short REMD simulations (100 ps) were carried out to validate the acceptance probability between adjacent replicas and/or to calibrate the above parameter k where exchanges are attempted every 1 ps. Afterwards, long REMD simulations (with a total length of 20 ns) are performed which are the basis of our analyis given in Sec. III C.

III. RESULTS AND DISCUSSION

A. Determination of Graphene Nanocapillary Water Filling

Before investigating the structure and dynamics of confined water, we first have to determine the water occupancy of the graphene capillary, i. e. the number of water molecules entering spontaneously the graphene slit which connects the two water reservoirs containing 1000 water molecules each as shown in Fig. 1. Similar filling studies have been carried out previously for water inside CNTs, see *e. g.*, Refs. [38, 83, 107]. For water inside graphene nanocapillaries, however, a systematic investigation of the effects of different (water-water and water-carbon) force fields is still missing. In this part of our investigation, MD simulations using the NPT approach of Sec. II B are applied to investigate the spontaneous filling process and determine the number of water molecules N_W (per square nanometer 1 nm^2) for

different temperatures and different pressures. In order to study the influence of the force fields, three series of simulations are performed.

First, the effect of the water–carbon interaction strength η on the water occupancy is investigated for different water–water interaction models. Our results for isotropic water–carbon interaction ($\delta = 0$) are shown in Fig. 3 a, for $T = 300$ K and for two different pressures, 0.1 MPa and 1000 MPa. By varying the interaction strength η between 0.25 kJ/mol and 1.5 kJ/mol, we simulate the transition from hydrophobic to hydrophilic graphene for the water models SPCE, TIP3P, TIP4P, TIP4P/ICE, and TIP5P. For ambient pressure, $P = 0.1$ MPa, water is repelled from the interior of the graphene nanocapillary below a certain value of η. Interestingly, that threshold appears to be similar ($\eta \approx 0.5$ kJ/mol) for four out of five water models. Only for the TIP3P model, water spontaneously fills the graphene slit for $P = 0.1$ MPa already for $\eta = 0.25$ kJ/mol. Above the respective threshold values, the water filling quickly rises and reaches saturation. For high pressure (1000 MPa), water can fill the graphene slit practically without barrier, independent of the interaction strength, but the density is only slightly higher than for ambient pressure 0.1 MPa.

Second, the effect of the anisotropy δ of the water–carbon interaction on the water occupancy is investigated, again for different water models. In contrast to the effect of the interaction strength η, the anisotropy δ does not affect N_W notably, as shown in Fig. 3 (b) for ambient pressure $P = 0.1$ MPa and high pressure $P = 1000$ MPa. In contrast to bulk water at ambient conditions, where the difference in the water density simulated with different water models is negligible [108], this is not the case for our results shown in Fig. 3 (a) and Fig. 3 (b), where the water occupancy reaches notably different values. Hence, this difference can be considered as an effect of quasi–2D confinement in the graphene slit. On the contrary, for $P = 1000$ MPa, the water densities display much less differences between the different water models.

Finally, the effect of pressure P on the water occupancy is shown in panel (c) of Fig. 3, in this case for the TIP4P water model only. The values N_W increase nearly linearly with the pressure for $T = 200$ K and $T = 400$ K, where as for $T = 300$ K the increase is first fast and then slows down. Overall, the number N_W for low temperature is higher than for high temperature, which can be caused by the different structures adopted at different temperatures, see below.

In summary, the above calculations show that the water occupancy of a graphene slit

reached by spontaneous filling depends much more sensitively on the choice of the water model for ambient conditions than for high pressure (1000 MPa). In the former case, there is a threshold with the effect of interaction strength η at ambient conditions for all investigated water models but not for TIP3P. Throughout the remainder of this work, a value of $\eta = 1$ kJ/mol and $\delta = 1$ will be used which is in agreement with our previous CCSD studies [84] and also with our previous simulations of water confined inside CNTs [38]. The resulting water densities found for the five different water models at $P = 1000$ MPa high pressure condition are listed in Tab. II. These values will be used consistently both for the mimimum energy configurations and for the finite temperature REMD simulations described in the following two subsections.

B. Minimum Energy Structures

This section is concerned with structure and polarization of water confined inside a graphene slit of 0.65 nm width within which water can form quasi-two-dimensional, single layer ice structures. First, we will discuss minimum energy structures which are obtained by means of a steepest decent algorithm implemented in the GROMACS 5.0 software package [95]. In order to sample the multitude of local minima of the high–dimensional potential energy landscape, a large number of minimizations were performed, which were initialized from snapshots of REMD trajectories (see Sec. II C), performed within the NVT ensemble with periodic boundary conditions along the ice plane. In these calculations, the number of water molecules, N_W, is taken from the results of the filling simulations of a graphene nanocapillary with an area of 33.74 nm^2 under 1000 MPa, as discussed above. By appropriate scaling of the water occupancy summarized in Tab. II, we obtained $N_W = 467, 462, 458, 467, 457$ for SPCE, TIP3P, TIP4P, TIP4P/ICE and TIP5P, respectively.

The H-bond networks of the quasi-2D water minimum energy structures are characterized in Fig. 4 and Tab. III where we use the following abbreviations: F, flat; P, puckered; S, square; R, rhombic; and N, nearly. The classification of the tetragons is mainly based on the distributions of the oxygen-oxygen-oxygen angles, α, defined between the nearest neighboring water molecules, see Fig. 5. Depending on the tilt angle, τ, we distinguish between nearly square (NS) ($|\tau| \leq 5^\circ$) and rhombic (R) else.

The proton ordering of the confined water can be quantified on the basis of the dimension-

less polarization $\langle\mu\rangle$ introduced in Sec. II C. Here we classify minimum energy structures as ferroelectric (FE) for $0.9 \leq \langle\mu\rangle < 1$, ferrielectric water (FI) for $0.1 \leq \langle\mu\rangle < 0.9$ and antiferroelectric (AF) with $\langle\mu\rangle < 0.1$.

The water–water and water–carbon interaction energies are also given in Tab. III. Note that in the following only the most stable, ordered minimum energy structures are discussed for each of the five water models under consideration.

1. SPCE Water Model

The minimum energy structures for water inside a graphene slit simulated by the traditional three-site SPCE water model can be assigned to two different classes of monolayer ice, a flat nearly square (FNS) structure a and a flat rhombic (FR) structure b. The top view of Fig. 4 shows that structure a (FNS) is almost square ice which can be also seen from the corresponding angle α distribution in Fig. 5 where the peaks are centered at 90°, 75° and 105°. Note that the strength of the 90° peak matches the sum of the other two. Additionally, the peak at 165° listed in Tab. III and shown in Fig. 5 represents the slightly zigzag lines connecting the oxygen atoms. The end view of structure a (FNS) shows that the water molecules are nearly in one plane, i.e. the ice layer is indeed almost flat.

Structure b (FR) is flat rhombic with sharp angular peaks located at $\alpha = 77°$ and 103° in Fig. 5. Furthermore, the peaks at 152° and 179° indicate that there are zigzag (horizontal) lines and straight (vertical) lines in the network of the O atoms in Fig. 4. Finally, the end view of structure b (FR) shows that the water molecules are again nearly in the same plane.

While the networks of the O-atoms differ only slightly, the proton ordering of structures a and b is completely different, see also the average dipole moments $\langle\mu\rangle$ in the fourth column of Table III. For structure a (FNS) we find a very low polarization $\langle\mu\rangle = 0.05$ thus rendering this structure AF. We can see that within each unit cell (light blue rectangle in Fig. 4) the four dipole vectors add up to nearly zero. For structure b (FR), however, the water dipoles point toward two different directions forming an angle of 82°, thus rendering this structure FI with polarization $\langle\mu\rangle = 0.75$, in agreement with $\cos 41° = 0.755$. While the water–water interaction energy E_{W-W} is 0.65 kJ/mol (or 1.5 %) lower for structure a (FNS) than for structure b (FR), the water–carbon interaction energies E_{W-C} are essentially identical.

2. TIP3P Water Model

For the TIP3P water model, another traditional three-site water force field, we found only one minimum energy ice structure, the flat rhombic (FR) structure c. In the top view of Fig. 4 and angle distribution of Fig. 5, it can be seen that structure c consists of two different rhombic sub-structures. Tab. III reveals that they are distinguished by two sets of angles α, centered at 77° and 103° versus 80° and 100°. Note that the former substructure is almost the same as structure b (FR) found for the SPCE water model. Again, the angle peaks at 156° and 179° indicate that the network of O atoms can be characterized by (horizontal) zigzag oxygen lines and straight (vertical) oxygen lines, again similar to structure b (FR). Also the water molecules of structure c (FR) are in one plane as displayed in the end view of Fig. 4 (c).

In analogy to structure b (FR), also structure c (FR) is found to be FI with a moderately high polarization $\langle\mu\rangle = 0.74$. Here the water dipoles are oriented along two different directions that form an angle of approximately 85° with each other.

3. TIP4P Water Model

For the four-site TIP4P water model, we found two types of minimum energy ice structures. The puckered nearly square (PNS) structure d with angle α peaked around 90°, 75° and 105° is very similar to structure a (FNS) found for the SPCE water model. Again, the strength of the 90° peak matches the strength of the sum of the other two. In addition, the angle distribution of structure d displays minor peaks near 81° and 99°. In both dimensions of the ice monolayer, the oxygen atoms are connected by zigzag lines with angles around α=163°. In addition, we also find a puckered rhombic (PR) minimum energy structure e. In the top view of Fig. 4 and angle distribution of Fig. 5 we can see that structure e consists of two different rhombic sub-structures distinguished by two sets of angular peaks, see also Tab. III. The angular peaks at 152° and 168° indicate that there are zigzag oxygen lines in both dimensions, but with a different curvature. Even though the difference between structure d (PNS) and e (PR) appears to be not very pronounced in Fig. 4, the angle distribution in Fig. 5 shows that almost half of the intensity for structure d (PNS) is found at 90°, whereas there is weak tilting (85°, 95°) in structure e (PR). Note that both in structure

d (PNS) and e (PR) the water layer is puckered, in marked contrast to the flat structures a, b and c observed in calculations for the SPCE and TIP3P water models. Obviously, this puckering is a consequence of moving the negative charge from the O–atom to a fourth potential site (dummy atom) located on the H–O–H bisector while keeping the LJ–term on the O–atom in the TIP4P model. Thus, slight puckering can reduce the LJ-repulsion while increasing the Coulomb attraction between nearest neighbor water molecules.

Finally, both structures d (PNS) and e (PR) are AF with polarization $\langle \mu \rangle$ near zero, hence in that respect very similar to structure a (FNS). The energy E_{W-W} is 0.72 kJ/mol lower for structure d (PNS) than for structure e (PR).

4. TIP4P/ICE Water Model

The TIP4P/ICE model is a modification of the original TIP4P model, aiming at an improved reproduction of the phase diagram of bulk water, but without a deterioration of the remaining bulk water properties. In our work on quasi-2D ice, we found one puckered nearly square (PNS) configuration f for the water model TIP4P/ICE, which is quite similar to structure d (PNS) found for the original TIP4P water model, as shown in Figs. 4 and 5. Also the AF proton ordering of structure f (PNS) is quite similar to that of structure d (PNS). However, the oxygen network of the former one appears to be a bit less puckered.

5. TIP5P Water Model

The five-site TIP5P water model was originally introduced to reproduce the bulk water density over a very wide range of pressures, including the density maximum near $T \approx 277$ K at ambient pressure. When using this water model in simulations of quasi-2D water confined in a graphene nanocapillary, we found two minimum energy ice forms, namely the flat rhombic (FR) structure g and the puckered rhombic (PR) structure h. With the angular peaks located at 71°, 101° and 116°, the FR structure g is regular but more tilted than the rhombic structures discussed above. Moreover, the peaks are not symmetric around 90° for water model TIP5P. Finally, there is another peak at 172° which indicates a slight curvature of the O–atom connectors.

The puckered rhombic (PR) structure h does not present a single crystalline form like all

structures mentioned thus far, but rather it contains different rhombic sub-structures. This is confirmed by the angle distribution in Fig. 5, displaying several groups of peaks around 60° and around 115°. Again the peak at 169° shows that there are zigzag oxygen lines in both dimensions similar to structure g (FR).

In contrast to our findings for the three– and four–site water models, both in structures g and h some of the O–H...O arrangements deviate substantially from linearity. Hence, H-bonds are not always drawn in Fig. 4 g and h. The reason for this is the tetrahedral arrangement of the charges in the TIP5P model mimicking the lone pair electrons [109]. Another consequence is that most of the H atoms are located in two different planes above and below the plane spanned by the O-atoms, as indicated in the side views. While in structure g (FR) the H–atoms are distributed equally between the two planes, the arrangement of the H–atoms of structure h (PR) appears to be more disordered. Nonetheless, as far as the proton ordering is concerned, both structures g (FR) and h (PR) are FE with very high polarizations of 0.97 and 0.94, respectively.

C. Temperature Effects and Structural Transitions

In this section we discuss the results of our REMD simulations within the NVT setting for the quasi-2D water system confined between two graphene layers. Special emphasis is on thermal effects and structural transitions within a temperature range between 200 K and about 600 K, for technical details see Sec. II C. Where possible, we want to identify the 2D minimum energy structures introduced in Sec. III B and try to estimate at which temperatures they occur. In that context, interesting observations are the temperature dependence of the distributions of oxygen angles α shown in Fig. 6 and the distributions of the (dimensionless) polarization $\langle\mu\rangle$ in Fig. 7 allowing to identify FE, FI and AF arrangements of the protons. In addition, we analyze the caloric curves along with a decomposition of the averaged energies into kinetic energy, LJ (water–carbon and water–water) and Coulomb (water–water only) potential energies, see Fig. 8. We shall use the water–water potential energy to determine at which temperature structural transitions occur and, where possible, to determine the latent heat for 2D ice structural transitions. Moreover, the structural transitions can be classified according to the definition of phase transitions. In first–order transitions first derivatives of the energy undergo discontinuous changes. In second–order

transitions first derivatives of the energy are continuous but the second derivatives are discontinuous. In addition, we distinguish liquid from solid phases by analyzing the self-diffusion constant from Eq. (4), based on normal NVT simulations for selected temperatures.

To further analyze the structure of water confined in a graphene nanocapillary, we also analyze the H-bonding networks obtained from our REMD simulations as shown in Fig. 9. To go beyond the number of H–bonds each water molecule is engaged in, the pattern of H–bonding between nearest neighbors is characterized here by joint probabilities p_{n_a,n_d} of a water molecule to act n_d times as a donor and n_a times as an acceptor at the same time [109]. To account for the floppy arrangement of water molecules in our simulations, we use a relaxed criterion for the detection of H-bonds, i. e. , O–O distance up to 0.35 nm and deviation from linearity of the O–H $\cdots$ O arrangement up to 45 degrees.

1. SPCE Water Model

From $T = 200$ K to $T = 283$ K, the distribution of peaks in the angle histogram of Fig. 6 indicates that the oxygen atoms are organized in a flat nearly square (FNS) phase as shown in Fig. 4 (a) with peaks around 72°, 90°, 108°, and 160°. At $T = 283$ K the sharp peaks become blurred indicating that the FNS–like structure starts to undergo a change. When the temperature further increases up to $T = 296$ K, suddenly two wide angular peaks appear to 72°, 108° which corresponds to the flat rhombic (FR) phase as shown in Fig. 4 (b). Hence, between $T = 283$ K and $T = 296$ K there is a structural transition from phase FNS to phase FR. However, the proton ordering shows a more complicated behavior, see the distribution of the polarization $\langle\mu\rangle$ in Fig. 7. From $T = 200$ K to $T = 313$ K, the ice phase is essentially AF with a very low polarization value, similar to that of FNS structure a. From $T = 329$ K to $T = 345$ K, the ice phase is FI with the polarization taking on several intermediate values with $0.25 \leq \langle\mu\rangle \leq 0.45$, indicating coexistence of different sub-domains of structure a (FNS) and b (FR). From $T = 364$ K to $T = 577$ K, the ice phase is still FI but displaying a higher polarization $\langle\mu\rangle \approx 0.75$, similar to the corresponding value of FR structure b. Other quantities of interest such as the caloric curves (Fig. 8) and hydrogen bonding pattern (Fig. 9), however, are not affected by the above transition, because the phases a (FNS) and b (FR) are nearly iso-energetic and share the same number of hydrogen bonds. Hence, the solid–solid structural transition between $T = 283$ K and $T = 296$ K is

classified as a second–order phase transition.

Fig. 6 shows another phase transition between $T = 577$ K and $T = 596$ K, marked by the disappearance of the peaks in the angular distribution at 72° and 108°. For temperatures above this transition, we observe a loss of the rhombic structure, leading to a liquid-like phase which is also confirmed by the abrupt rise of the self-diffusion constant D, see Eq. (4). Note that this is in contrast to the work by Maiti *et al.* for ambient pressure (0.1 MPa) where such a transition is found in the temperature range between 290 K and 300 K [110].

In the angular histogram of Fig. 6, a new peak arises around 60°, mainly caused by nearly triangular configurations appearing in the irregular liquid structure. Also between 120° and 140° the intensity increases smoothly, indicating the coexistence with irregular tetragons and pentagons. The detection of this melting-like transition is also supported by the temperature dependence of the hydrogen–bonding patterns shown in Fig. 9. At $T = 577$ K the probability of fourfold coordination, $p_{2,2}$, starts to decrease drastically while that for three-fold coordination, $p_{1,2}$, starts to rise. Moreover, Fig. 7 shows that there is also a substantial loss of proton ordering in the same temperature range, leading from FI to AF arrangements. In summary, this transition from an ordered quasi-2D crystal to a liquid-like phase is a first-order transition, which is also clear from Fig. 8 showing a sudden increase of the total water potential energy by nearly 4.0 kJ/mol (obtained from linear fits to the water–water potential energy below and above the transition temperature). This latent heat is higher than the bulk ice melting energy of 3.1 kJ/mol obtained for SPCE water simulations which, however, largely underestimates the experimental value of 6.029 kJ/mol [111] at 273 K for ambient pressure (0.1 MPa), see also Tab. IV. Obviously, the confinement of water inside a graphene capillary with a high pressure of 1000 MPa causes the substantial increase of the transition temperature from 215 K to 577 K for SPCE water model.

Thermodynamic stability: rhombic vs. nearly square ice phases

For the example of the SPCE water model, we further investigate the question of thermodynamic stability of rhombic (FR) vs. nearly square (FNS) ice quantitatively. The respective conformational probabilities, P_{FR} and P_{FNS} at different simulation temperatures, are obtained from the oxygen–oxygen–oxygen angle histograms shown in Fig. 6. The corresponding Helmholtz free energy difference ΔA can then be calculated via the van't Hoff

isotherm [112]

$$\Delta A(T) = -RT \ln K(T) \tag{8}$$

where the equilibrium constant is $K = P_{FR}/P_{FNS}$ and R is the ideal gas constant. From the relation

$$\Delta A(T) = \Delta U - T\Delta S \tag{9}$$

we obtain the entropy difference ($\Delta S \approx 0.02\,\mathrm{kJ/mol/K}$), see Fig.10 (a). Further, ΔU is obtained via the Gibbs-Helmholtz equation [113]

$$\frac{\partial}{\partial T}\Big(\frac{\Delta A}{T}\Big)_V = -\frac{\Delta U}{T^2} \tag{10}$$

which yields approximately 5.67 kJ/mol, see Fig. 10 (b).

In summary, the FNS ice phase is energetically favorable. However, the entropy of the FR phase is higher. Hence, ΔA becomes negative for $T > 283$ K. Thus, the transition temperature nearly coincides with the results from our structural analysis given above.

2. TIP3P Water Model

At $T = 200$ K the distribution of peaks in the angle histograms in Fig. 6 indicates that the oxygen atoms are organized in a flat rhombic (FR) arrangement, similar to that shown in Fig. 4 c, with sharp peaks centered at 77° and 103°. However, with the temperature increasing from $T = 200$ K to $T = 532$ K, the peaks become blurred which indicates that the phase c (FR) is gradually disappearing. Within that temperature range, the quasi-2D ice is FI with the polarization $\langle\mu\rangle \approx 0.74$ being practically constant, see Fig. 7. The two quantities show a clear structural transition from the ordered structure c (FR) to a liquid-like phase occurring between $T = 532$ K and $T = 551$ K. As for the SPC/E results discussed above, this melting-like transition can also be detected from characteristic changes of the O angles as well as from the loss of proton ordering. This transition also shows up in the self-diffusion constant D as well as in the energy decomposition shown in Fig. 8 where all curves show an inflection at 532 K with a latent heat around 3.4 kJ/mol which is much higher than the bulk water melting energy of 1.3 kJ/mol from TIP3P simulations. Again,

the melting temperature of the quasi-2D water is much higher than for bulk water, which is due to the confinement and the high pressure of 1000 MPa.

The melting-like transition is also reflected in the structure of the H–bonding networks. Fig. 9 shows that from $T = 200$ K to $T = 532$ K the joint probability $p_{2,2}$ decreases continuously indicating that the quasi-2D ice structure disappears. Between $T = 551$ K and $T = 617$ K the joint probability $p_{2,2}$ decreases further (but more slowly) while there are increasing probabilities of defects with two–, three–, and even five–fold coordination.

3. TIP4P Water Model

At $T = 200$ K, the distribution of the peaks in the angle histogram of Fig. 6 shows that the oxygen atoms are organized in a nearly square (PNS) fashion, similar to that shown in Fig. 4 (d), with peaks at 75°, 90°, and 105°. From $T = 200$ K to $T = 245$ K, the sharp peak at 90° becomes blurred and eventually vanishes for $T = 256$ K while the other peaks at 75° and 105° remain essentially unchanged. This indicates a structural change of the quasi-2D ice from nearly square phase d (PNS) to rhombic phase e (PR) in the temperature range between $T = 245$ K and $T = 256$ K. Moreover, the transition from phase d to phase e is confirmed by the distributions of polarization $\langle\mu\rangle$ in Fig. 7. However, there the transition between the phases (both of which are AF) is found at a higher temperature of $T = 359$ K. The temperature dependence of the energy decomposition, see Fig. 8, and of the hydrogen bonding pattern, see Fig. 9, however, are less sensitive to this transition because the two phases are nearly isoenergetic and share the same hydrogen bonding pattern. Again, this solid–solid structural transition is classified as a second–order phase transition. It is worth mentioning that both the square and the rhombic TIP4P quasi-2D phases are puckered which is quite different from the water structures obtained for the SPCE and TIP3P water models.

Both Figs. 6 and 7 show another phase transition between $T = 424$ K and $T = 434$ K with the sudden disappearance of the peaks in the two types of histograms. Again, this is a melting-like transition from a solid to a liquid-like phase, similar to those discussed for the three-site water models. This first–order transition is also detected in the H-bond patterns shown in Fig. 9 and in the energy decomposition shown in Fig. 8. There, all curves for water show an inflection at $T = 424$ K which is much higher than the melting temperature

for TIP4P bulk water at $T = 232$ K. Our value for the quasi-2D water latent heat around 3.3 kJ/mol is below the bulk water melting energy 4.4 kJ/mol from TIP4P simulations, see Tab. IV.

4. TIP4P/ICE Water Model

The TIP4P/ICE model is a variant of the original TIP4P model, intended to improve the properties of ice and the phase diagram for bulk water. In particular, the predicted melting temperature of hexagonal ice (Ih) at 0.1 MPa is now at a much more realistic value of 272.2 K. The results of our simulations for quasi-2D water using the TIP4P/ICE model can be seen in the angle histograms of Fig. 6. At $T = 200$ K, the peaks at 75°, 90°, and 105° suggest that the oxygen atoms are organized in a nearly square fashion corresponding to phase f (PNS), see Fig. 4 (f). From $T = 200$ K to $T = 515$ K, the three peaks become more and more blurred, thus indicating an increasing flexibility of the quasi-2D ice structure. Throughout this temperature range, the polarization $\langle\mu\rangle$ remains very low (see Fig. 7), in accordance with the AF character of structure f.

Between $T = 515$ K to $T = 529$ K, both the oxygen and hydrogen atoms become disordered and the structure changes from solid to liquid-like. The temperature for this melting-like transition is considerably higher than for the original TIP4P model. Again, this transition is a first–order phase transition which is confirmed the hydrogen bonding pattern (Fig. 9) as well as the energy decomposition (Fig. 8). The latent heat of 3.8 kJ/mol is less than the bulk water melting energy 5.4 kJ/mol from TIP4P/ICE simulation, both of which are notably higher than the corresponding values for the TIP4P model, see again Tab. IV.

5. TIP5P Water Model

From $T = 200$ K to $T = 229$ K, the distribution of peaks in the angle histograms in Fig. 6 indicates a flat rhombic oxygen structure. The peaks are located around 70° and 110° resembling those found for structure g (FR) which is also confirmed by the high polarization (FE) of $\langle\mu\rangle \approx 0.97$ in Fig. 7. From $T = 238$ K to $T = 297$ K, the angular peaks shift and their distribution becomes broader, thus becoming similar to structure h (PR) as shown

in Fig. 4, with the oxygen atoms being more irregular and also weakly puckered. This ice phase is also FE with very high polarization value $\langle\mu\rangle \approx 0.95$, but slightly lower than for the lowest temperature phase, as shown in Fig. 7. The transition between the FR and PR phases occuring in the temperature range from $T = 229$ K to $T = 238$ K is a second-order transition since no latent heat is involved, see the energy decomposition shown in Fig. 8.

Between $T = 309$ K and $T = 533$ K, the angular distributions in Fig. 6 does not change notably. The low self–diffusion constant D indicates that the water is still solid–like, but a careful inspection of snapshots of the structures reveals that the ice is amorphous. In this temperature range, the polarization $\langle\mu\rangle$ is gradually decreasing, corresponding to a transformation from FE to FI proton arrangement, as shown in Fig. 7. Note that both the LJ and the Coulombic parts of the water–water interaction energy displays a slight inflection upon the transition from ordered to amorphous ice, occurring between temperature $T = 297$ K and $T = 309$ K. Because of the different signs of the energy changes of the two contributions, they almost cancel each other, thus rendering also this transition second ordered phase transition.

When raising the temperature to 553 K, there is a rapid onset of self-diffusion with D rising from values below 0.1 to about 0.7 nm^2/ns indicating a melting-like phase transition between $T = 533$ K and $T = 553$ K. Interestingly, this transition is hardly visible in the angular distributions of Fig. 6, neither does the polarization shown in Fig. 7 reflect this transition clearly. Also the latent heat is negligible; it cannot be compared with the value for bulk water melting (7.3 kJ/mol from simulation and 6.029 kJ/mol from experiments at 273 K and 0.1 MPa pressure) as shown in Tab. IV.

IV. SUMMARY AND CONCLUSIONS

In the present work we have investigated the structure and dynamics of quasi–2D water confined in between two layers of graphene at a distance of 0.65 nm. In a first series of simulations we determined the water occupancy of the nanocapillary for five different water–water interaction models using MD simulations. It is found that the differences in the water occupancy at high pressure (1000 MPa) are negligible. Furthermore, neither the total water–carbon interaction strength, η, nor the corresponding anisotropy parameter, δ, have notable effects on the water occupancy.

Based on the water occupancies obtained from these filling simulations, we studied minimum energy quasi–2D ice structures for the different water models. The main difference from bulk ice is the complete absence of hexagonal structure; instead only tetragonal arrangements are found. Depending on the tilt angle, τ, these tetragons are classified as nearly square or as rhombic. Both these classes of structures are found for the SPCE and TIP4P water models at very similar energy. However, only nearly square patterns are observed for water model TIP4P/ICE whereas in other cases (TIP3P, TIP5P) only rhombic minimum energy structures are detected. Note the analogy with our previous studies of water confined inside low–diameter carbon nanotubes (CNTs) [38]. When unrolling the single–walled ice nanotubes (INTs), very similar water networks were found. For near–zero, medium, or strong tilt of the tetragons, the INT structures could be classified as prism-like, single helix, or double helix, respectively.

In addition, we studied the effect of using different water models on the proton ordering of quasi-2D ice. Our calculations revealed antiferroelectric structures for SPCE, TIP4P and TIP4P/ICE, whereas ferrielectric arrangements are found for SPCE and TIP3P. Only for TIP5P also ferroelectric quasi-2D ice was detected, which is partly different from our previous results for single walled INTs inside CNTs where also various ferrielectric and antiferroelectric structures were found [38].

In conclusion, by comparing both oxygen arrangements and proton ordering, we showed that the choice of water models plays a key role in determining the outcome of our simulations. Obviously, this makes a direct comparison with previous work in the literature difficult. In addition, such comparisons are hampered by different values for the pressure, temperature and the graphene slit width, as well as different assumptions for the water–graphene interaction. One should keep in mind that our potential energy function, based on high–level electronic structure calculations [83, 84], is less hydrophobic and more anisotropic than in most calculations found in the literature [22, 44, 62, 64, 71, 76]. The experimental evidence of square monolayer ice is of key importance, see Ref. [22] . In that work also simulation results were reported for SPCE water, indicating nearly square networks of water molecules, very similar to our findings for the same water model. Also Ref. [64] is of particular importance, where it is shown that these nearly square quasi–2D ice structures for TIP4P water are found only when the pressure exceeds the compression limit of a few hundred MPa, and that these structures are flat only when the slit width is below 0.67 nm.

Such ice structures were also found in other simulation studies of TIP4P water but confined between other hydrophobic surfaces [44]. In contrast to our results, nearly square ice was also detected in TIP5P simulations, however, for lower temperature and pressure [76].

Rhombic quasi-2D arrangements, which we found for almost all water models investigated, were also predicted in the TIP5P water simulations of Ref. [71], however, for lower temperature, lower pressure, and narrower graphene slits. In addition, such ice structures were also found in other simulation studies based on the TIP4P water model [62, 68] as well as TIP5P water model [42] but for water confined in capillaries of other hydrophobic materials.

Apart from simple tetragonal ice structures, also certain Archimedean tiling patterns were obtained for water adsorbed on a fully hydroxylated silica surface based on density-functional theory (DFT) calculations [114]. Subsequently, such patterns were also found in TIP5P simulations of water confined in graphene slits, however, for rather low water density and hundreds of MPa negative lateral pressure [71, 76].

Note that also hexagonal quasi-2D ice phases were observed in TIP5P water but only for lower water densities, narrower graphene slits, weaker lateral pressures and lower temperatures than in our simulations [71]. Similar structures were also predicted for SPCE water confined between hydrophobic plates [67].

While there is no experimental evidence yet for ferroelectricity of water monolayers inside graphene nanocapillaries, an atomic force microscopy (AFM) imaging work suggests the possibility that water monolayers adsorbed on mica surfaces are ferroelectric [82]. Subsequently, ferroelectric proton ordering was found in TIP5P MD simulations both for the above-mentioned hexagonal and rhombic monolayer ice [71]. Note that those proton ordered rhombic structures are comparable to our results for the same water model. In other studies based on the TIP5P water model, however, neither ferroelectric nor ferrielectric water orientations were found [76], probably due to different pressures applied.

To the best of our knowledge, quasi-2D ferrielectric ice structures for SPCE and TIP3P water models were observed in our work for the first time. Our finding of anti-ferroelectric ice structures for four–site water models is in agreement with previous results [62, 64], despite the different assumptions, i.e. hydrophobic water–graphene force field and isotropic water–graphene interaction.

The resulting temperature-dependence of the structural properties of quasi-2D water

reveals intriguing transition phenomena: In particular, we encountered two classes of phase transitions. Firstly, there are structural transitions between different solid phases which, in most cases, are similar to some of the minimum energy structures mentioned above. Because these structures are normally very close in energy, the transitions between them are classified as second–order transitions, without latent heat involved. Examples are the FNS–FR transition found for the SPCE water model between $T = 283$ K and $T = 296$ K, the PNS–PR transition found for TIP4P between $T = 245$ K and $T = 256$ K and the FR–PR transition found for TIP5P between $T = 229$ K and $T = 238$ K. Second, there are melting–like transitions between solid and liquid phases of quasi-2D water. These transitions are classified as first–order transitions, with a notable latent heat (with TIP5P being an exception). The value of the latent heat, however, is model dependent. It ranges from 3.3 kJ/mol (TIP4P) to 4.0 kJ/mol (SPCE), which is in all cases different from the respective simulation results for bulk water which in turn are considerably below the experimental value of 6 kJ/mol for bulk water. Also the temperatures at which those melting–like transitions occur are strongly dependent on the water model: The transition temperatures range from 424 K (TIP4P) to 577 K (SPCE). All of these temperatures are much higher (factor 1.5 to almost 3) than the corresponding temperatures found in simulations of bulk water using the same water models. Interestingly, those temperatures are comparable with the phase transition temperatures of water confined inside carbon nanotubes observed using Raman spectroscopy [115], revealing reversible melting between 378 K and 424 K (360 K and 390 K) for 1.05 nm (1.06 nm) diameter single-walled carbon nanotubes, respectively.

ACKNOWLEDGMENTS

S. L. is grateful to the Chinese Scholarship Council for financial support. The authors would like to thank the HPC Service of ZEDAT, Freie Universität Berlin, for computing time.

---

[1] Q. Zheng, D. J. Durben, G. H. Wolf, and C. A. Angell, Science **254**, 829 (1991).

[2] P. H. Poole, F. Sciortino, U. Essmann, and H. E. Stanley, Nature **360**, 324 (1992).

[3] J. L. Finney, Philos. Trans. R. Soc. B Biol. Sci. **359**, 1145 (2004).

[4] D. Chandler, Nature **437**, 640 (2005).

[5] C. E. Bertrand, Y. Zhang, and S.-H. Chen, Phys. Chem. Chem. Phys. **15**, 721 (2013).

[6] J. Carrasco, A. Hodgson, and A. Michaelides, Nat. Mater. **11**, 667 (2012).

[7] Y. Gao, S. Kim, S. Zhou, H.-C. Chiu, D. Nélias, C. Berger, W. de Heer, L. Polloni, R. Sordan, A. Bongiorno, and E. Riedo, Nat. Mater. **14**, 714 (2015).

[8] A. Kolesnikov, J.-M. Zanotti, C.-K. Loong, P. Thiyagarajan, A. Moravsky, R. Loutfy, and C. Burnham, Phys. Rev. Lett. **93**, 035503 (2004).

[9] H. Kyakuno, M. Fukasawa, R. Ichimura, K. Matsuda, Y. Nakai, Y. Miyata, T. Saito, and Y. Maniwa, J. Chem. Phys. **145**, 064514 (2016).

[10] H. Kyakuno, K. Matsuda, H. Yahiro, Y. Inami, T. Fukuoka, Y. Miyata, K. Yanagi, Y. Maniwa, H. Kataura, T. Saito, M. Yumura, and S. Iijima, J. Chem. Phys. **134**, 244501 (2011).

[11] S. Cambré, B. Schoeters, S. Luyckx, E. Goovaerts, and W. Wenseleers, Phys. Rev. Lett. **104**, 207401 (2010).

[12] H.-J. Wang, X.-K. Xi, A. Kleinhammes, and Y. Wu, Science **322**, 80 (2008).

[13] Y. Maniwa, H. Kataura, M. Abe, S. Suzuki, Y. Achiba, H. Kira, and K. Matsuda, J. Phys. Soc. Japan **71**, 2863 (2002).

[14] A.I. Kolesnikov, C.-K. Loong, N. R. de Souza, C. J. Burnham, and A. P. Moravsky, Phys. B Condens. Matter **385-386**, 272 (2006).

[15] J. K. Holt, H. G. Park, Y. Wang, M. Stadermann, A. B. Artyukhin, C. P. Grigoropoulos, A. Noy, and O. Bakajin, Science **312**, 1034 (2006).

[16] O. Byl, J.-C. Liu, Y. Wang, W.-L. Yim, J. K. Johnson, and J. T. Yates, J. Am. Chem. Soc. **128**, 12090 (2006).

[17] Y. Maniwa, H. Kataura, M. Abe, A. Udaka, S. Suzuki, Y. Achiba, H. Kira, K. Matsuda, H. Kadowaki, and Y. Okabe, Chem. Phys. Lett. **401**, 534 (2005).

[18] K. T. He, J. D. Wood, G. P. Doidge, E. Pop, and J. W. Lyding, Nano Lett. **12**, 2665 (2012).

[19] D.-S. Yang and A. H. Zewail, Proc. Natl. Acad. Sci. **106**, 4122 (2009).

[20] Y. Zheng, C. Su, J. Lu, and K. P. Loh, Angew. Chemie Int. Ed. **52**, 8708 (2013).

[21] G. a. Kimmel, J. Matthiesen, M. Baer, C. J. Mundy, N. G. Petrik, R. S. Smith, Z. Dohnalek, and B. D. Kay, J. Am. Chem. Soc. **131**, 12838 (2009).

[22] G. Algara-Siller, O. Lehtinen, F. C. Wang, R. R. Nair, U. Kaiser, H. A. Wu, A. K. Geim,

and I. V. Grigorieva, Nature **519**, 443 (2015).

[23] G. Hummer, J. C. Rasaiah, and J. P. Noworyta, Nature **414**, 188 (2001).

[24] L. Xu and V. Molinero, J. Phys. Chem. B **115**, 14210 (2011).

[25] F. Klameth and M. Vogel, J. Chem. Phys. **138**, 134503 (2013).

[26] A. Berezhkovskii and G. Hummer, Phys. Rev. Lett. **89**, 064503 (2002).

[27] C. Dellago, M. Naor, and G. Hummer, Phys. Rev. Lett. **90**, 105902 (2003).

[28] J. Köfinger, G. Hummer, and C. Dellago, Proc. Natl. Acad. Sci. U. S. A. **105**, 13218 (2008).

[29] L. Wang, J. Zhao, F. Li, H. Fang, and J. P. Lu, J. Phys. Chem. C **113**, 5368 (2009).

[30] W. H. Noon, K. D. Ausman, R. E. Smalley, and J. Ma, Chem. Phys. Lett. **355**, 445 (2002).

[31] J. Wang, Y. Zhu, J. Zhou, and X.-H. Lu, Phys. Chem. Chem. Phys. **6**, 829 (2004).

[32] J. Bai, J. Wang, and X. C. Zeng, Proc. Natl. Acad. Sci. U. S. A. **103**, 19664 (2006).

[33] D. Takaiwa, I. Hatano, K. Koga, and H. Tanaka, Proc. Natl. Acad. Sci. U. S. A. **105**, 39 (2008).

[34] A. Alexiadis and S. Kassinos, Chem. Rev. **108**, 5014 (2008).

[35] J. Bai, C.-R. Su, R. D. Parra, X. C. Zeng, H. Tanaka, K. Koga, and J.-M. Li, J. Chem. Phys. **118**, 3913 (2003).

[36] K. Koga, R. D. Parra, H. Tanaka, and X. C. Zeng, J. Chem. Phys. **113**, 5037 (2000).

[37] K. Koga, G. T. Gao, H. Tanaka, and X. C. Zeng, Nature **412**, 802 (2001).

[38] S. Li and B. Schmidt, Phys. Chem. Chem. Phys. **17**, 7303 (2015).

[39] R. Zangi, J. Phys. Condens. Matter **16**, S5371 (2004).

[40] R. Zangi and A. E. Mark, J. Chem. Phys. **120**, 7123 (2004).

[41] J. C. Johnston, N. Kastelowitz, and V. Molinero, J. Chem. Phys. **133**, 154516 (2010).

[42] R. Zangi and A. E. Mark, Phys. Rev. Lett. **91**, 025502 (2003).

[43] R. Zangi and A. E. Mark, J. Chem. Phys. **119**, 1694 (2003).

[44] T. Kaneko, J. Bai, K. Yasuoka, A. Mitsutake, and X. C. Zeng, J. Chem. Phys. **140**, 184507 (2014).

[45] F. de los Santos and G. Franzese, Phys. Rev. E **85**, 010602 (2012).

[46] E. G. Strekalova, M. G. Mazza, H. E. Stanley, and G. Franzese, Phys. Rev. Lett. **106**, 145701 (2011).

[47] M. G. Mazza, K. Stokely, H. E. Stanley, and G. Franzese, J. Chem. Phys. **137**, 204502 (2012).

[48] S. Han, M. Y. Choi, P. Kumar, and H. E. Stanley, Nat. Phys. **6**, 685 (2010).

[49] J. Bai and X. C. Zeng, Proc. Natl. Acad. Sci. **109**, 21240 (2012).

[50] N. Giovambattista, P. J. Rossky, and P. G. Debenedetti, Phys. Rev. Lett. **102**, 050603 (2009).

[51] J. Bai, X. C. Zeng, K. Koga, and H. Tanaka, Mol. Simul. **29**, 619 (2003).

[52] L. B. Krott and M. C. Barbosa, J. Chem. Phys. **138**, 084505 (2013).

[53] K. Koga, X. C. Zeng, and H. Tanaka, Phys. Rev. Lett. **79**, 5262 (1997).

[54] N. Giovambattista, P. J. Rossky, and P. G. Debenedetti, Phys. Rev. E **73**, 041604 (2006).

[55] P. Kumar, S. V. Buldyrev, F. W. Starr, N. Giovambattista, and H. E. Stanley, Phys. Rev. E **72**, 051503 (2005).

[56] M. Meyer and H. E. Stanley, J. Phys. Chem. B **103**, 9728 (1999).

[57] P. Kumar, F. W. Starr, S. V. Buldyrev, and H. E. Stanley, Phys. Rev. E **75**, 011202 (2007).

[58] H. Mosaddeghi, S. Alavi, M. H. Kowsari, and B. Najafi, J. Chem. Phys. **137**, 184703 (2012).

[59] F. Corsetti, J. Zubeltzu, and E. Artacho, Phys. Rev. Lett. **116**, 1 (2016).

[60] W.-H. Zhao, J. Bai, L. Wang, L.-F. Yuan, J. Yang, J. S. Francisco, and X. C. Zeng, J. Mater. Chem. A **3**, 5547 (2015).

[61] K. Koga, H. Tanaka, and X. C. Zeng, Nature **408**, 564 (2000).

[62] K. Koga and H. Tanaka, J. Chem. Phys. **122**, 104711 (2005).

[63] T. Werder, J. H. Walther, R. L. Jaffe, T. Halicioglu, and P. Koumoutsakos, J. Phys. Chem. B **107**, 1345 (2003).

[64] Y. Zhu, F. Wang, J. Bai, X. C. Zeng, and H. Wu, ACS Nano **9**, 12197 (2015).

[65] W.-H. Zhao, L. Wang, J. Bai, L.-F. Yuan, J. Yang, and X. C. Zeng, Acc. Chem. Res. **47**, 2505 (2014).

[66] G. Cicero, J. C. Grossman, E. Schwegler, F. Gygi, and G. Galli, J. Am. Chem. Soc **130**, 1871 (2008).

[67] A. L. Ferguson, N. Giovambattista, P. J. Rossky, A. Z. Panagiotopoulos, and P. G. Debenedetti, J. Chem. Phys. **137**, 144501 (2012).

[68] T. Kaneko, J. Bai, K. Yasuoka, A. Mitsutake, and X. C. Zeng, J. Chem. Theory Comput. **9**, 3299 (2013).

[69] H. Qiu and W. Guo, Phys. Rev. Lett. **110**, 195701 (2013).

[70] I. Strauss, H. Chan, and P. Král, J. Am. Chem. Soc. **136**, 1170 (2014).

[71] W.-H. Zhao, J. Bai, L.-F. Yuan, J. Yang, and X. C. Zeng, Chem. Sci. **5**, 1757 (2014).

[72] M. Sobrino Fernandez Mario, M. Neek-Amal, and F. M. Peeters, Phys. Rev. B **92**, 245428 (2015).

[73] F. Corsetti, P. Matthews, and E. Artacho, Sci. Rep. **6**, 18651 (2016).

[74] J. Chen, G. Schusteritsch, C. J. Pickard, C. G. Salzmann, and A. Michaelides, Phys. Rev. Lett. **116**, 025501 (2016).

[75] N. Raghav, S. Chakraborty, and P. K. Maiti, Phys. Chem. Chem. Phys. **17**, 20557 (2015).

[76] J. Bai, C. A. Angell, and X. C. Zeng, Proc. Natl. Acad. Sci. **107**, 5718 (2010).

[77] L. Pauling, J. Am. Chem. Soc. **57**, 2680 (1935).

[78] Y. Nakamura and T. Ohno, Mater. Chem. Phys. **132**, 682 (2012).

[79] X. Su, L. Lianos, Y. R. Shen, and G. A. Somorjai, Phys. Rev. Lett. **80**, 1533 (1998).

[80] M. J. Iedema, M. J. Dresser, D. L. Doering, J. B. Rowland, W. P. Hess, A. A. Tsekouras, and J. P. Cowin, J. Phys. Chem. B **102**, 9203 (1998).

[81] D. N. LeBard and D. V. Matyushov, J. Phys. Chem. B **114**, 9246 (2010).

[82] C. Spagnoli, K. Loos, A. Ulman, and M. K. Cowman, J. Am. Chem. Soc. **125**, 7124 (2003).

[83] G. Pérez-Hernández and B. Schmidt, Phys. Chem. Chem. Phys. **15**, 4995 (2013).

[84] S. Lei, B. Paulus, S. Li, and B. Schmidt, J. Comput. Chem. **37**, 1313 (2016).

[85] H. J. C. Berendsen, J. R. Grigera, and T. P. Straatsma, J. Phys. Chem. **91**, 6269 (1987).

[86] W. L. Jorgensen, J. Chandrasekhar, J. D. Madura, R. W. Impey, and M. L. Klein, J. Chem. Phys. **79**, 926 (1983).

[87] W. L. Jorgensen and J. D. Madura, Mol. Phys. **56**, 1381 (1985).

[88] J. L. F. Abascal, E. Sanz, R. García Fernández, and C. Vega, J. Chem. Phys. **122**, 234511 (2005).

[89] M. W. Mahoney and W. L. Jorgensen, J. Chem. Phys. **112**, 8910 (2000).

[90] R. Swendsen and J. Wang, Phys. Rev. Lett. **57**, 2607 (1986).

[91] U. H. Hansmann, Chem. Phys. Lett. **281**, 140 (1997).

[92] Y. Sugita and Y. Okamoto, Chem. Phys. Lett. **314**, 141 (1999).

[93] S. Trebst, M. Troyer, and U. H. E. Hansmann, J. Chem. Phys. **124**, 174903 (2006).

[94] E. Voloshina, D. Usvyat, M. Schütz, Y. Dedkov, and B. Paulus, Phys. Chem. Chem. Phys. **13**, 12041 (2011).

[95] B. Hess, C. Kutzner, D. van der Spoel, and E. Lindahl, J. Chem. Theory Comput. **4**, 435

(2008).

[96] S. Miyamoto and P. A. Kollman, J. Comput. Chem. **13**, 952 (1992).

[97] G. Bussi, D. Donadio, and M. Parrinello, J. Chem. Phys. **126**, 014101 (2007).

[98] H. J. C. Berendsen, J. P. M. Postma, W. F. van Gunsteren, A. DiNola, and J. R. Haak, J. Chem. Phys. **81**, 3684 (1984).

[99] S. Nosé, Mol. Phys. **52**, 255 (1984).

[100] W. G. Hoover, Phys. Rev. A **31**, 1695 (1985).

[101] M. Parrinello and A. Rahman, J. Appl. Phys. **52**, 7182 (1981).

[102] W. L. Jorgensen, J. Chandrasekhar, J. D. Madura, R. W. Impey, and M. L. Klein, J. Chem. Phys. **79**, 926 (1983).

[103] T. Darden, D. York, and L. Pedersen, J. Chem. Phys. **98**, 10089 (1993).

[104] U. Essmann, L. Perera, M. L. Berkowitz, T. Darden, H. Lee, and L. G. Pedersen, J. Chem. Phys. **103**, 8577 (1995).

[105] P. G. Kusalik and I. M. Svishchev, Science **265**, 1219 (1994).

[106] N. Metropolis, A. W. Rosenbluth, M. N. Rosenbluth, A. H. Teller, and E. Teller, J. Chem. Phys. **21**, 1087 (1953).

[107] H. Kumar, C. Dasgupta, and P. K. Maiti, RSC Adv. **5**, 1893 (2015).

[108] C. Vega, E. Sanz, and J. L. F. Abascal, J. Chem. Phys. **122**, 114507 (2005).

[109] N. Agmon, Acc. Chem. Res. **45**, 63 (2012).

[110] H. Kumar, C. Dasgupta, and P. K. Maiti, Langmuir **34**, 12199 (2018).

[111] L. A. Curtiss, D. J. Frurip, and M. Blander, J. Chem. Phys. **71**, 2703 (1979).

[112] P. Atkins and J. de Paula, *Physical Chemistry, Volume 1: Thermodynamics and Kinetics* (Macmillan Higher Education, 2016).

[113] P. Atkins, *Molecules in motion: ion transport and molecular diffusion* (1978) pp. 819–848.

[114] J. Yang, S. Meng, L. F. Xu, and E. G. Wang, Phys. Rev. Lett. **92**, 146102 (2004).

[115] K. V. Agrawal, S. Shimizu, L. W. Drahushuk, D. Kilcoyne, and M. S. Strano, Nat. Nanotechnol. **12**, 267 (2017).

water model	temperatures (K)
SPCE	200 207 214 222 232 244 256 269 283 296 313 329 345 364 381 398 418 438 460 479 499 518 538 557 577 592 606 624
TIP3P	200 207 215 224 233 243 254 266 277 289 302 315 329 343 359 375 392 409 427 443 458 473 488 502 516 532 551 571 594 617
TIP4P	200 207 216 224 234 245 256 268 281 293 305 318 332 346 359 374 389 403 415 424 434 448 464 482 499 518 539 559 583 607
TIP4P/ICE	200 207 216 225 235 246 258 270 281 295 308 322 338 354 371 389 407 425 443 460 478 493 505 515 529 545 564 582 604 627
TIP5P	200 206 213 221 229 238 247 256 266 276 286 297 309 322 335 349 362 376 393 409 423 439 455 474 493 512 533 553 572 593

TABLE I. Temperature distributions used in REMD simulations for water inside graphene nanocapillaries for different water models SPCE, TIP3P, TIP4P, TIP4P/ICE, and TIP5P. In total, every REMD simulation is 20 ns long.

Pressure (MPa)	SPCE	TIP3P	TIP4P	TIP4P/Ice	TIP5P
0.1	12.98	12.93	11.89	13.17	11.49
1000	13.84	13.70	13.59	13.83	13.55

TABLE II. Density of water confined in graphene nanocapillaries (molecules per nm^2) for different water models. For $T = 300$ K and for graphene–water interaction parameters $\eta = 1$ kJ/mol and $\delta = 1$.

	structure	water model	$\langle\mu\rangle$	α	E_{W-W}	E_{W-C}
a	FNS	SPCE	0.05	75 90 105 165	-45.66	-20.02
b	FR	SPCE	0.75	77 103 152 179	-45.01	-19.99
c	FR	TIP3P	0.74	77 80 100 103 156 179	-45.47	-20.14
d	PNS	TIP4P	0.09	75 81 90 99 105 163	-43.68	-19.76
e	PR	TIP4P	0.02	75 85 95 105 152 168	-42.96	-19.41
f	PNS	TIP4P/ICE	0.03	75 90 105 156 165	-57.83	-19.60
g	FR	TIP5P	0.97	71 101 116 172	-36.90	-19.98
h	PR	TIP5P	0.94	60 71 82 100 109 118 131 169	-36.70	-19.79

TABLE III. Different minimum energy quasi–2D ice structures found for water confined in graphene nanocapillaries simulated with different water models. The structures are characterized by their polarizations $\langle\mu\rangle$ (dimensionless) and H-bond networks characterized by angle α (degree). Finally, E_{W-W} (kJ/mol) and E_{W-C} (kJ/mol) denote the water–water and water–carbon potential energies per molecule, respectively. The structures are denoted as follows: F = flat; P = puckered; N = nearly; S= square and R = rhombic. Note that these structures are also shown in Figs. 4, 5.

		SPCE	TIP3P	TIP4P	TIP4P/ICE	TIP5P	Expt.
T_m	Bulk water[a]	215	145.6	232	272.2	273.9	273.15
T_m	Confined water	577	532	424	515	297	–
ΔE	Bulk water[a]	3.1	1.3	4.4	5.4	7.3	6.029
ΔE	Confined water	4.0	3.4	3.3	3.8	0.23	–

TABLE IV. Melting temperatures (K) and latent heats (kJ/mol) of bulk ice and quasi–2D confined ice (P = 1000 MPa) simulated using different water models versus experimental values. [a] From Ref. [108] (SPCE, TIP3P,TIP4P,TIP5P), Ref. [88] (TIP4P/ICE)

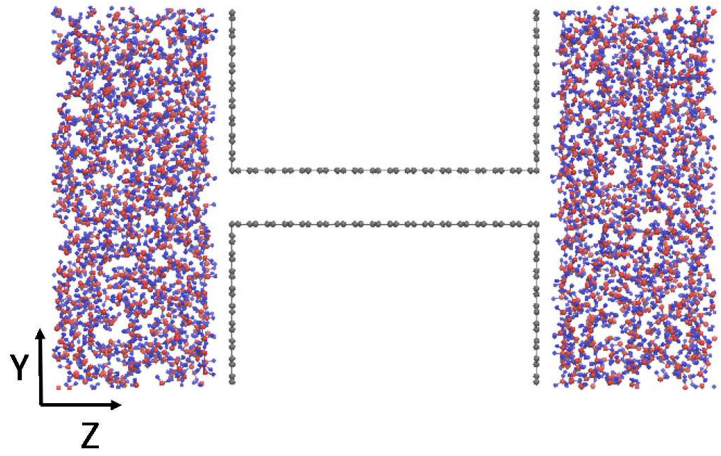

FIG. 1. Configuration for MD filling simulations to obtain the water densities confined inside graphene nanocapillaries. The MD simulation system initially contains 1000 molecules on each side.

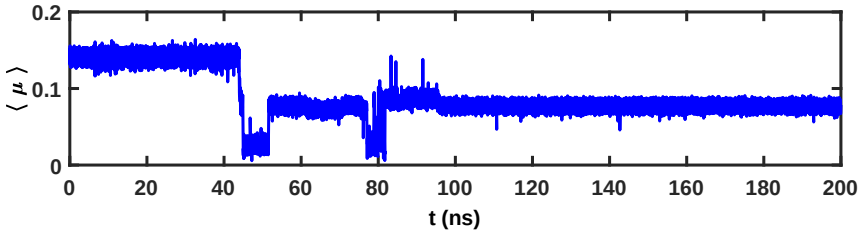

FIG. 2. Time evolution of dimensionless polarization for 467 water molecules (SPCE) inside a graphene nanocapillary for T =300 K. Note the metastable phases extending over tens of nanoseconds.

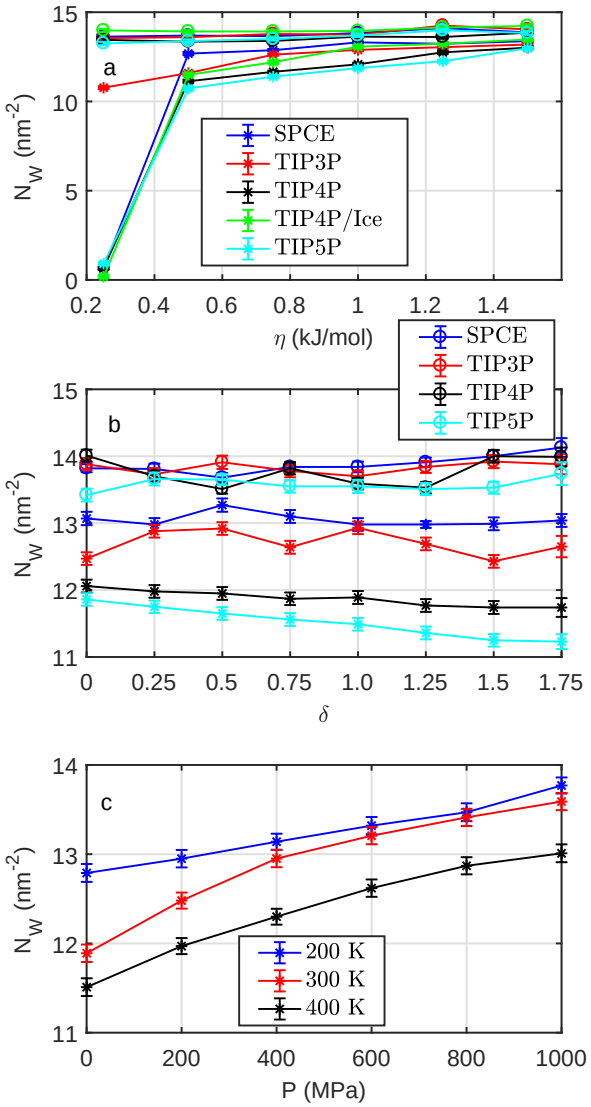

FIG. 3. (a) Influence of water models on water occupancy, N_W, of a graphene nanocapillary, as a function of the water–carbon interaction strength η, for isotropic interaction, $\delta = 0$, $T = 300$ K and two different pressure 0.1 MPa (stars) or $P = 1000$ MPa (circles). (b) Influence of anisotropy parameter δ on water occupancy, N_W, for fixed interaction strength, $\eta = 1$ kJ/mol, for $T = 300$ K, and $P = 0.1$ MPa (stars) or $P = 1000$ MPa (circles). (c) Influence of pressure and temperature on water occupancy, N_W, for fixed anisotropy, $\delta = 1$, $\eta = 1$ kJ/mol, and for TIP4P water model.

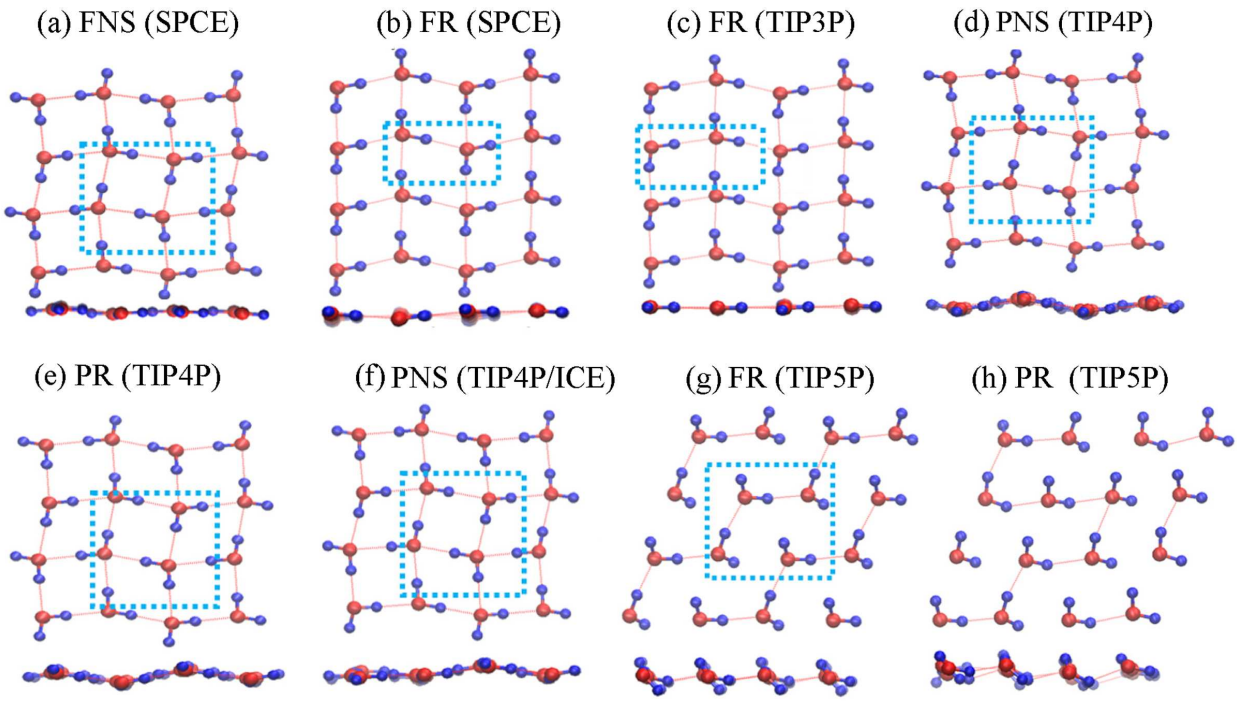

FIG. 4. Minimum energy structures of water confined inside a graphene nanocapillary for various water models indicated in brackets. Here, the blue rectangles are unit cells. The structures are denoted as follows: F = flat; P = puckered; N = nearly; S= square and R = rhombic, respectively. Note that these structures are also characterized in Fig. 5 and in Tab. III

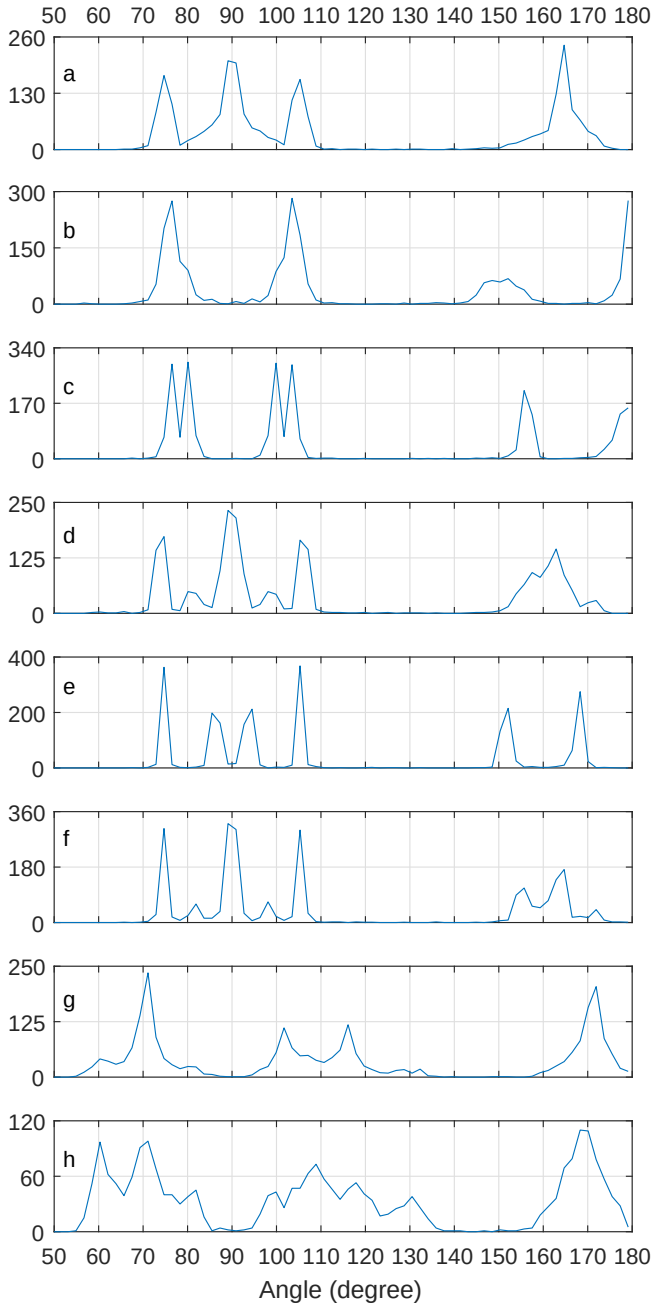

FIG. 5. Distribution of oxygen angles α of quasi–2D water confined inside a graphene nanocapillary. Distributions are obtained from minimum energy structures found for SPCE (a,b), TIP3P(c), TIP4P(d,e), TIP4P/ICE(f), and TIP5P(g,h) water model.

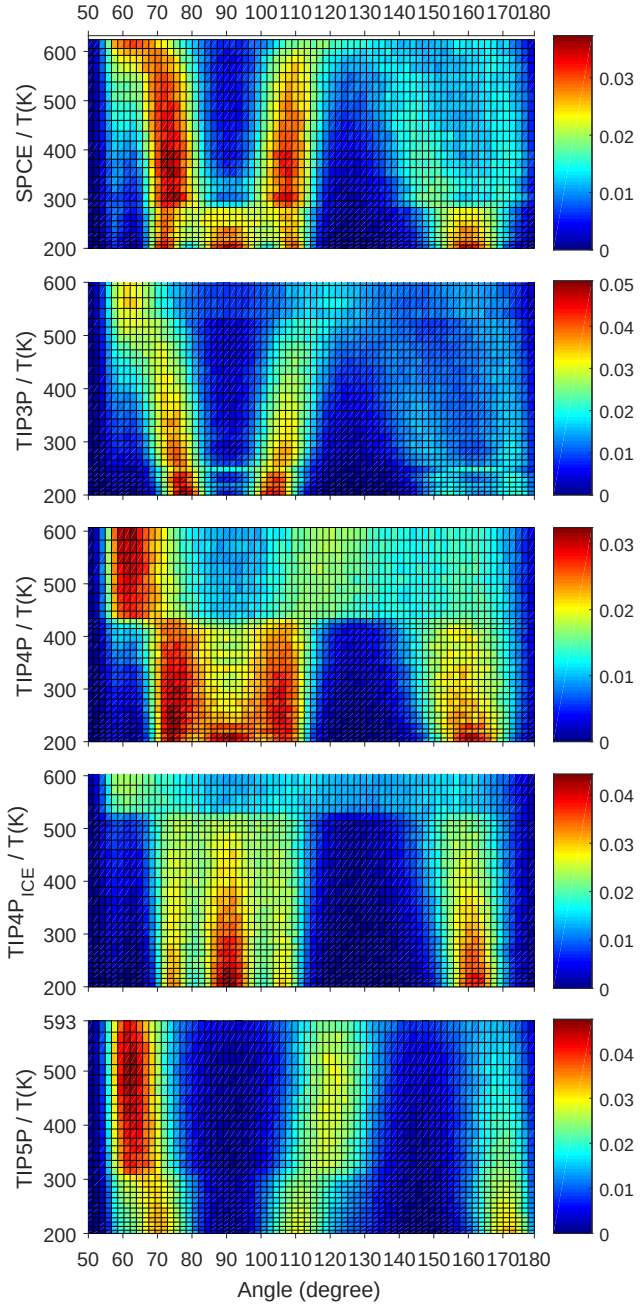

FIG. 6. Distribution of oxygen angles α for quasi–2D water confined inside a graphene nanocapillary as a function of temperature. Obtained from REMD simulations with $\eta = 1$ kJ/mol, $\delta = 1$, and for the SPCE, TIP3P, TIP4P, TIP4P/ICE, and TIP5P water models from top to bottom for a pressure of 1000 MPa.

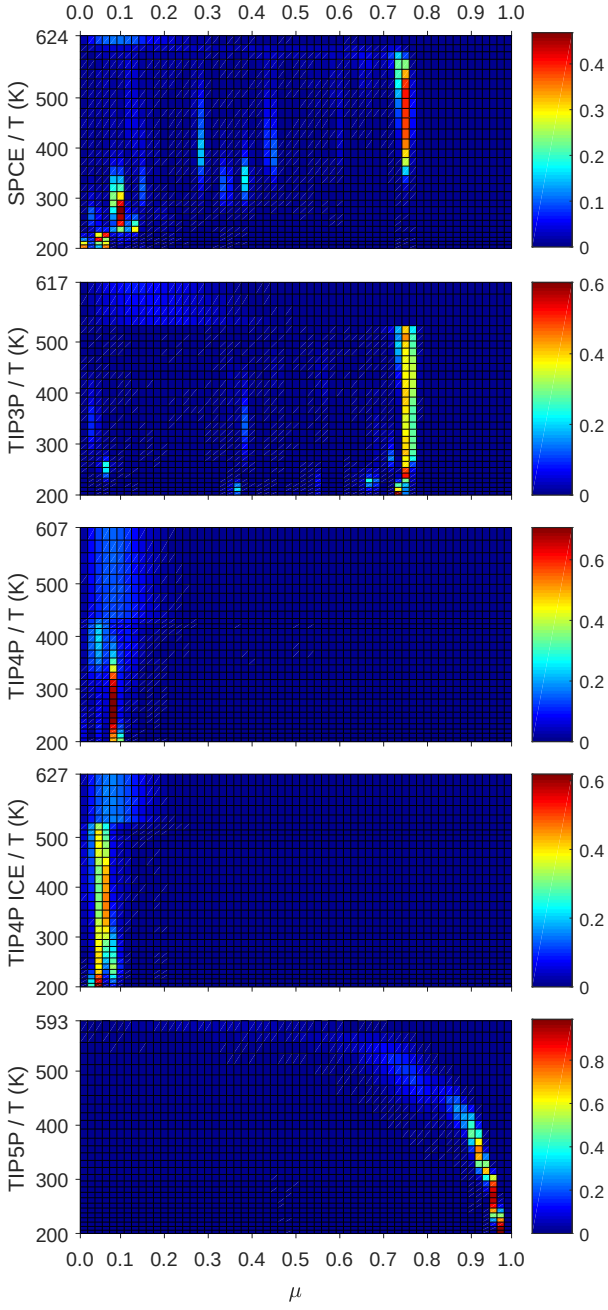

FIG. 7. Distribution of polarizations $\langle\mu\rangle$ for water confined inside a graphene nanocapillary as a function of temperature. Obtained from REMD simulations with $\eta = 1$ kJ/mol, $\delta = 1$, and for the SPCE, TIP3P, TIP4P, TIP4P/ICE, and TIP5P water models from top to bottom for a pressure of 1000 MPa.

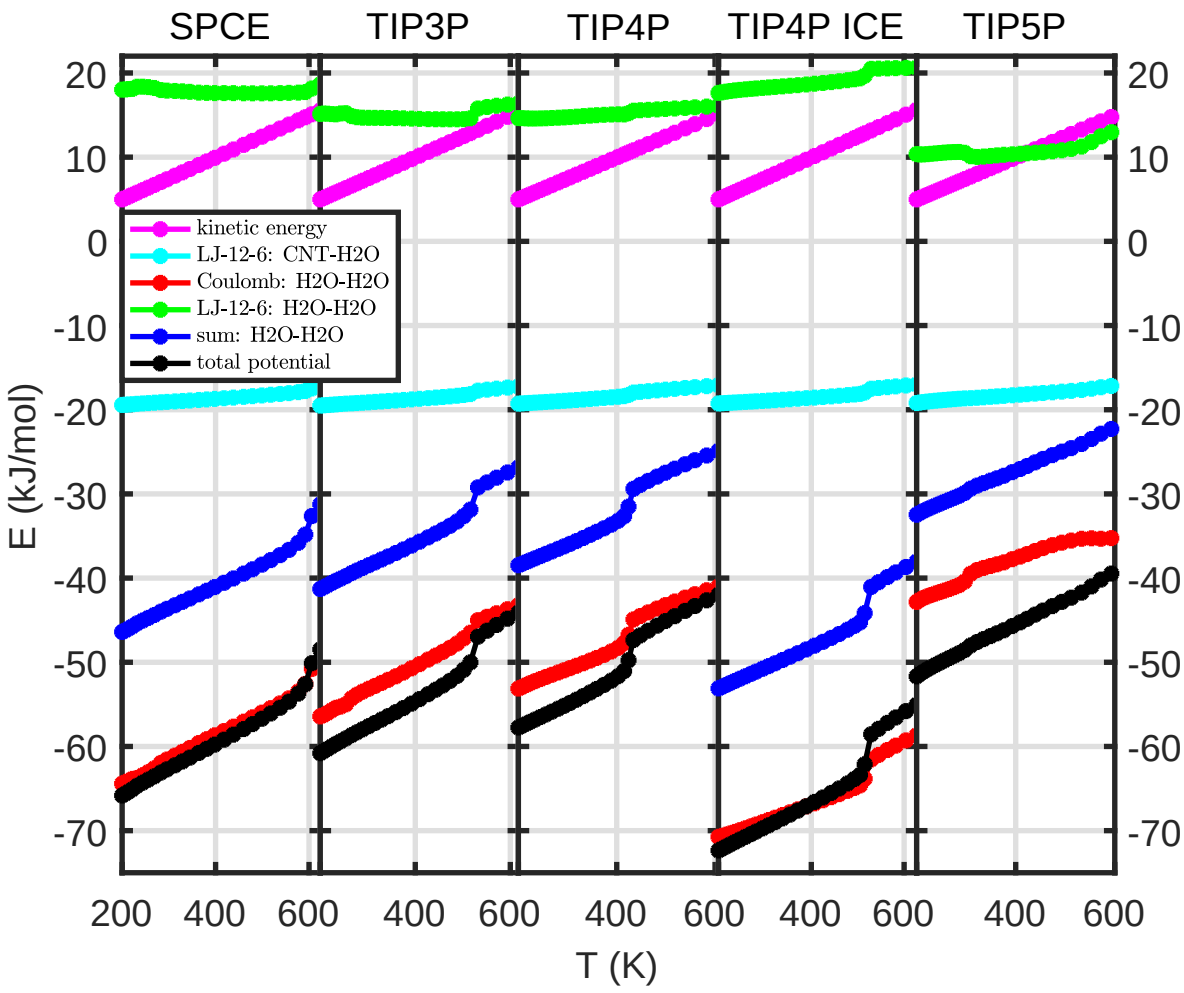

FIG. 8. Decomposition of total energy in REMD simulations of water confined inside a graphene nanocapillary as a function of temperature. For $\eta = 1$ kJ/mol, $\delta = 1$, and for SPCE, TIP3P, TIP4P, TIP4P/ICE, and TIP5P water model.

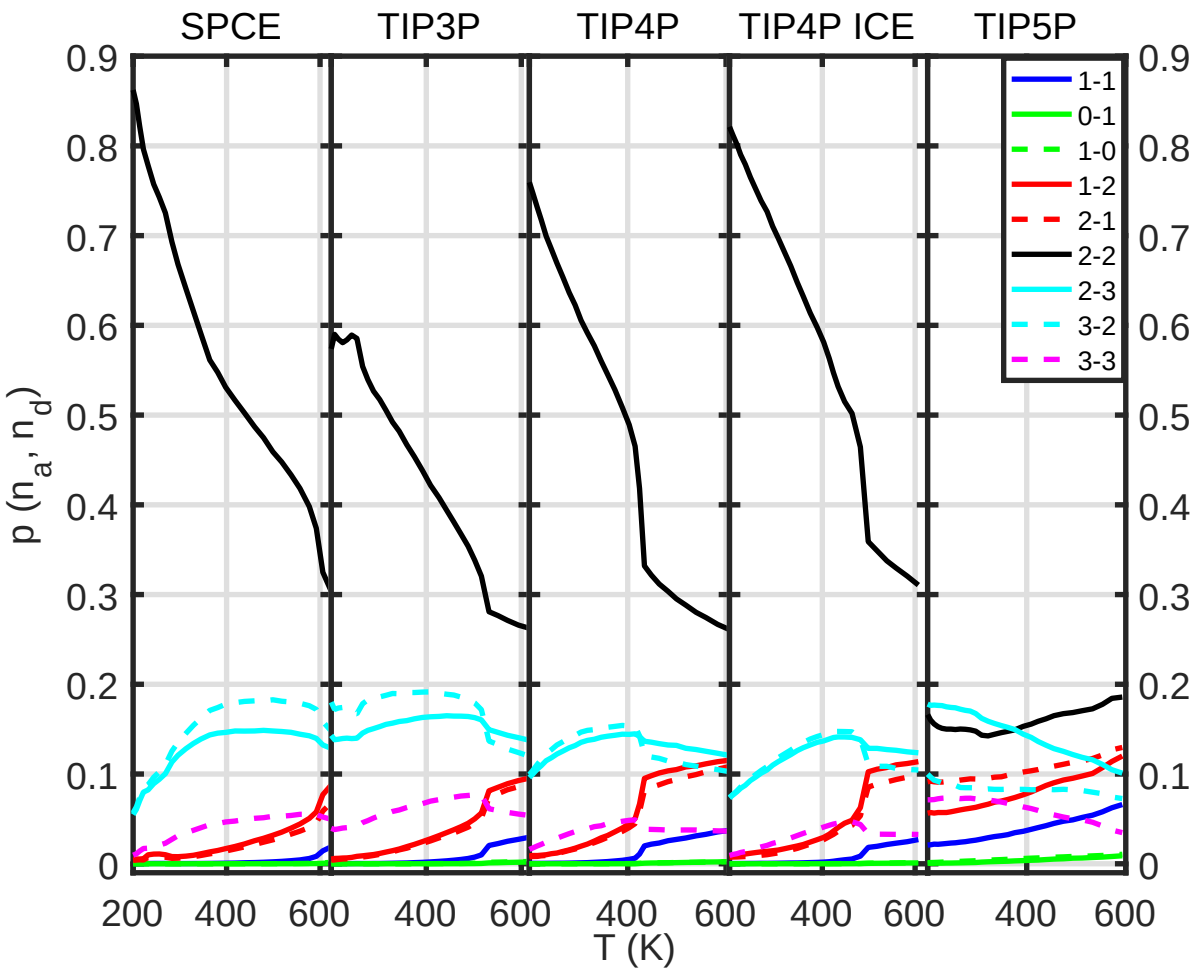

FIG. 9. H–bonding pattern of water confined inside a graphene nanocapillary as a function of temperature. Obtained from REMD simulations with $\eta = 1$ kJ/mol, $\delta = 1$, and for SPCE, TIP3P, TIP4P, TIP4P/ICE, and TIP5P water models. The curves indicate the joint probabilities, p_{n_a,n_b}, of a water molecule acting n_a times as an acceptor and n_d times as a donor, as indicated in the figure legend.

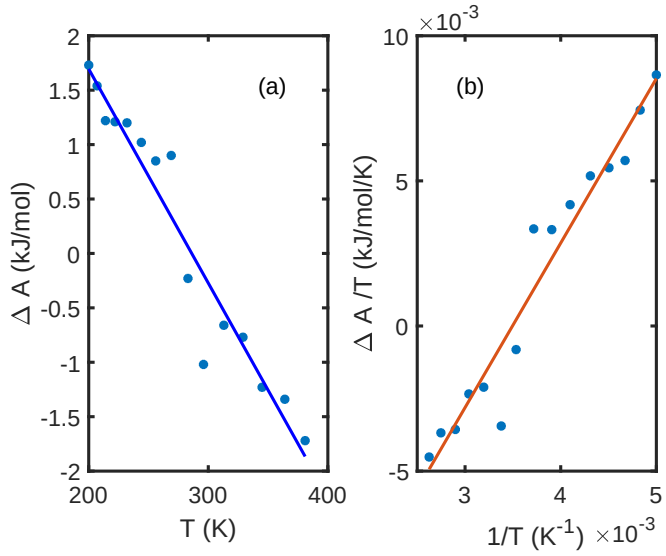

FIG. 10. (a) Helmholtz free energy difference ΔA between FNS and FR ice phases as a function of temperature between 200 K and 381 K, with the slope yielding the entropy difference, ΔS , see main text. (b) Gibbs–Helmholtz representation of $\Delta A/T$ versus $1/T$, leading to ΔU.

Chapter 4

Summary

The goal of this dissertation was to understand the structure and dynamics of quasi–1D and quasi–2D water confined in low dimensional carbon materials by the use of molecular dynamics simulation methods combined with enhanced sampling strategies. For this goal, a first step was to derive simple but reliable LJ potential models for the interaction between water and carbon sheets of different curvature. These effective models then can be used to carry out a series of MD investigations on water confined inside CNTs and graphene capillaries, comprising the variation of the water model.

Because of the large number of particles typically involved in MD simulations of water in CNTs and graphene sheets, practically all previous work was based on empirical force fields. In addition, structure and dynamics of quasi–1D water confined inside CNTs[63, 124] and quasi–2D water between graphene sheets[82, 108] were found to depend sensitively on the parameters of LJ potentials. Hence, it is of crucial importance to obtain quantitatively correct values for those parameters.[154, 171–173]

In paper A1, we were able to derive two sets of effective and reliable LJ parameters for water inside and outside CNTs of different curvature, by fitting to our high quality DFLCCSD(T) quantum chemistry results. In particular, by adding dummy particles that mimic the polarizability of the oxygen atom, we improved the quality of atom-centered LJ models. These LJ models are used to calculate the water adsorption energies of larger CNTs, approaching the graphene limit, thus bridging the gap between CNTs of increasing radius and flat graphene sheets. Each of two sets of parameters can reproduce three out of four minima of the effective potential curves reasonably well. Finally, we mention that, in agreement with our previous findings for water interacting with graphene,[124], the overall water–carbon interaction strength obtained from fitting to the DF-LCCSD(T) results is considerably stronger than assumed in most of the previous classical MD simulations.[24, 48, 51, 58, 61, 62, 70, 174] Hence, the present work suggests that CNTs may be less hydrophobic than expected.

Moreover, the results for the water—carbon interaction showed a rather strong anisotropy with respect to the water orientation, which was not considered in most of the previous work either, for an exception see Ref. [175].

Next, we will summarize the key results of our second investigations. In paper A2, quasi–one dimensional water inside CNTs was studied by means of MD simulations with SPC, SPCE, TIP3P, TIP4P, and TIP5P water models inside CNTs with diameters from 0.54 nm to 2.7 nm and with a length of nearly 10 nm. We investigated the water occupancy of open–ended armchair and zigzag CNTs immersed in water and found that the water model and the anisotropy parameter δ have only a minor influence on the water density as shown in Fig. 4.1. However, varying the total water–carbon interaction strength η can cause a clear threshold separating a hydrophobic and a hydrophilic regime.

For the force field parameters being $\eta = 1$ kJ/mol, $\delta = 1$ and for the TIP5P water model, our main simulations of water filling were conducted for 30 different CNTs of considerable length ($L \approx 10$ nm), with diameters d between 0.54 nm and 2.7 nm, both zigzag $(n,0)$ with $8 \leq n \leq 20$ and armchair (n,n) nanotubes with $4 \leq n \leq 20$. Our results for the dependence of the number of water molecules, N_W, on the CNT diameter are given in Fig. 4.2.

Based on the filling simulations, we performed REMD simulation techniques under NVT conditions for water encapsulated in armchair CNTs (n,n), $5 \leq n \leq 10$ with water model TIP5P. The minimum energy INTs structures are trigonal, pentagonal, hexagonal and octagonal for water confined inside CNT $(7,7)$, $(8,8)$, $(9,9)$ and $(10,10)$, respectively. Different helicity of the networks formed by the O-atoms was detected, e.g., single helical structures for $7 \leq n \leq 10$, double helical structures for $n = 8$ and prism–like structures for $8 \leq n \leq 10$.

In addition to this O–atom arrangement, we are also interested in the question: whether INTs can be ferroelectric. We found highly ferroelectric, quasi–1D water chains inside the smallest nanotubes $(n = 5,6)$ and different single-walled INTs inside other CNTs $(n \geq 7)$, see Fig. 4.3 and Tab. 4.1. The polarization value 0.91 for single helix INT $\langle 3,1\rangle$ inside CNT $(7,7)$ is the highest from all INTs we investigated, thus rendering this structure highly FE. The minimum energy structure $\langle 5,0\rangle$ for water inside CNT (8,8) can be assigned as ferroelectric structure with all water dipoles pointing toward the same direction and ferrielectric structure with the proton ordering is reversed where the proton ordering is reversed in one or two of the five water strands along prism edges; but for the helical structures $\langle 5,1\rangle$ and $\langle 5,2\rangle$ inside CNT (8,8) only ferroelectric proton ordering is observed. For water inside CNT $(9,9)$, the minimum energy structure $\langle 6,0\rangle$ features prisms exhibiting ferroelectric, ferrielectric and antiferroelectric proton arrangement. In contrast, the $\langle 6,1\rangle$ structure exhibits only ferroelectric ordering. For water inside CNT $(10,10)$, octagonal INT structures are found, the structure $\langle 8,0\rangle$ consists of prisms exhibiting ferroelectric, ferrielectric and antiferroelectric proton arrangement. The helical $\langle 8,1\rangle$ structure exhibits only ferroelectric ordering.

Furthermore, different transition phenomena such as first–order melting–like (solid–liquid) and

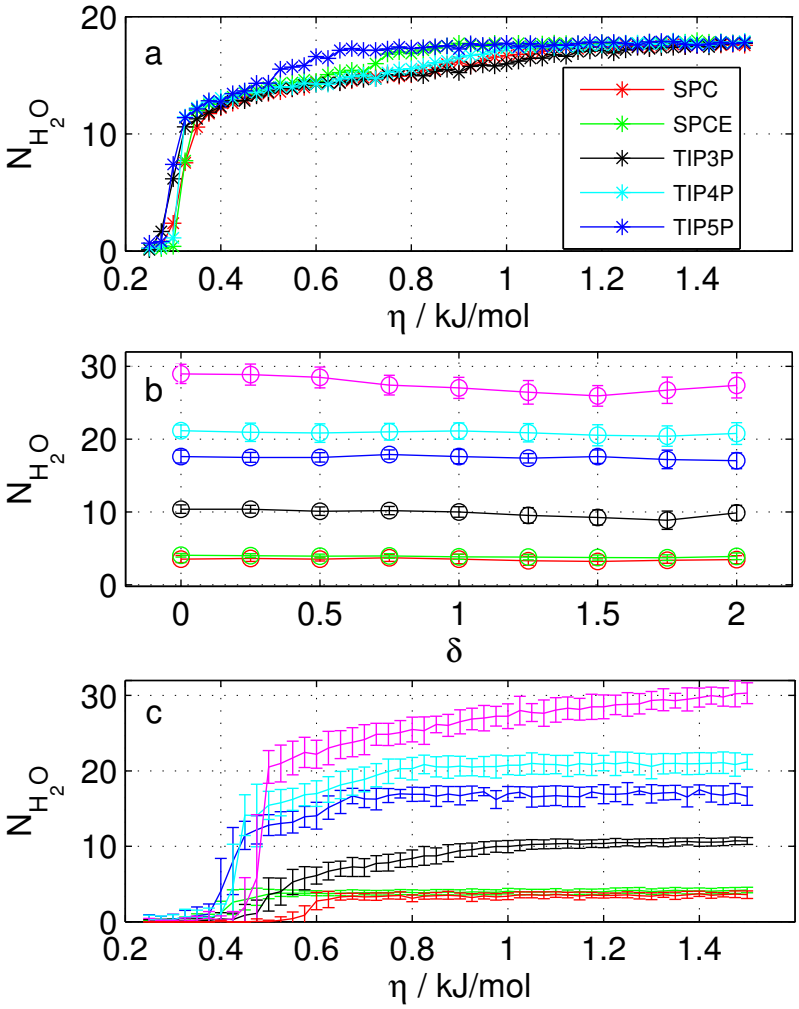

Figure 4.1: (a) Influence of water models on water occupancy, N_W, inside CNT (8,8), as a function of the water—carbon interaction strength η, for isotropic interaction, $\delta = 0$. (b) Influence of anisotropy parameter δ on water occupancy, N_W, for fixed water—carbon interaction strength, $\eta = 1$ kJ/ mol, and for TIP5P water model. (c) Influence of interaction strength η on water occupancy N_W, for fixed anisotropy, $\delta = 1$, and for TIP5P water–model. Red, green, black, blue, cyan, and magenta curves are for CNT (5,5), CNT (6,6), CNT (7,7), CNT (8,8), CNT (9,9), and CNT (10,10), respectively, in (b) and (c).

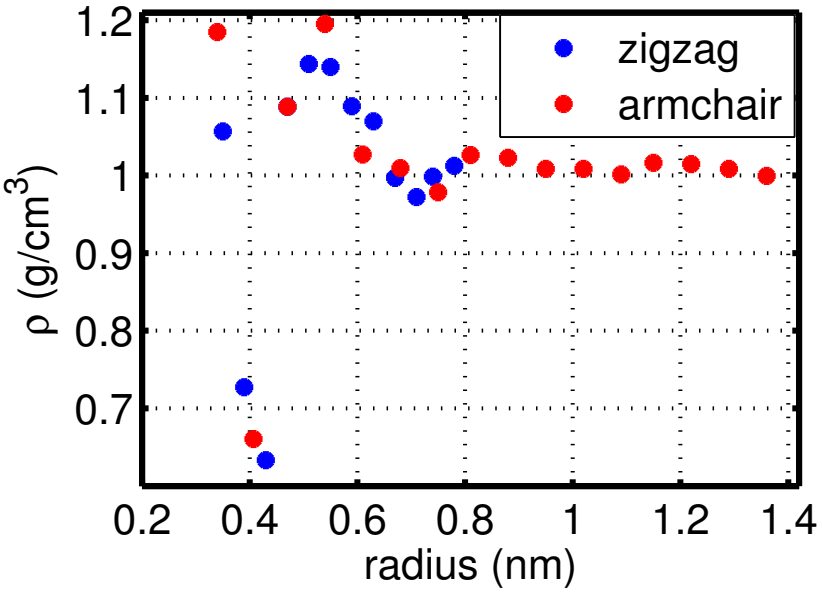

Figure 4.2: Water density $\rho = M/V$ versus CNT diameter d, for various armchair (red) and zigzag (blue) CNTs for $T = 300K$, $P = 10^5 Pa$, $\delta = 1$ and $\eta = 1$ kJ/mol and for the TIP5P water model. For the underlying water occupancy numbers, N_W, see paper A1. For the calculation of the inner CNT volume V, see paper A1.

(n,m)	R(nm)	N_{H_2O} (nm^{-1})	(n,m)	R(nm)	N_{H_2O} (nm^{-1})	(n,m)	R(nm)	N_{H_2O} (nm^{-1})
(4,4)	0.27	0.00	(8,8)	0.54	17.18	(20,0)	0.78	39.67
(8,0)	0.31	0.00	(14,0)	0.55	17.28	(12,12)	0.81	44.27
(5,5)	0.34	3.59	(15,0)	0.59	20.25	(13,13)	0.88	54.19
(9,0)	0.35	3.59	(9,9)	0.61	20.90	(14,14)	0.95	64.52
(10,0)	0.39	3.70	(16,0)	0.63	23.82	(15,15)	1.02	76.69
(6,6)	0.41	3.91	(17,0)	0.67	26.18	(16,16)	1.09	89.16
(11,0)	0.43	4.50	(10,10)	0.68	27.61	(17,17)	1.15	102.66
(12,0)	0.47	10.33	(18,0)	0.71	29.86	(18,18)	1.22	117.69
(7,7)	0.47	10.33	(19,0)	0.74	34.15	(19,19)	1.29	133.03
(13,0)	0.51	13.91	(11,11)	0.75	34.66	(20,20)	1.36	148.88

Table 4.1: Water occupancy of different armchair (n,n) and zigzag $(n,0)$ CNTs with radii R for $T = 300$ K, $P = 1$ bar, $\delta = 1$ and $\eta = 1kJ/mol$ and for the TIP5P water model. Here, N_{H_2O} denotes the number of water molecules per unit length of 1 nm.

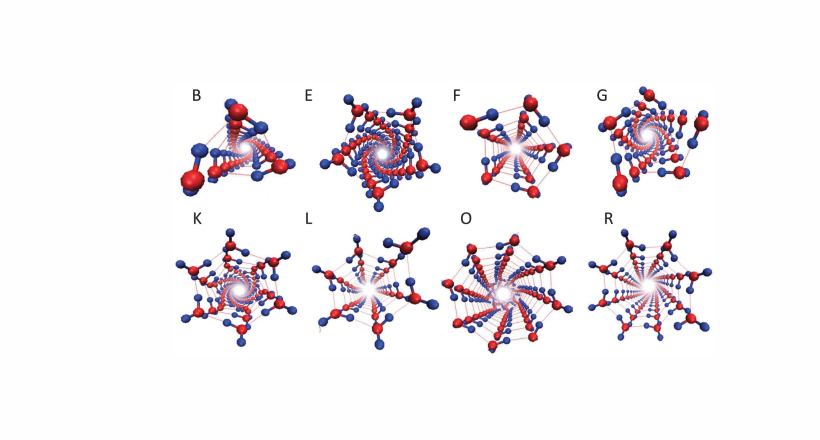

Figure 4.3: End views of selected minimum energy structures of INTs confined inside low diameter CNTs. (B): INT$< 3,1 >$ inside CNT (7,7); (E–G): INT $< 5,0 >$, $< 5,1 >$, $< 5,2 >$ inside CNT (8,8); (K, L): INT $< 6,0 >$, $< 6,1 >$ inside CNT (9,9); (O, R): INT $< 8,0 >$, $< 8,1 >$ inside CNT (10,10).

second–order (solid–solid) phase transitions transitions were detected. These transitions could be either abrupt first–order or smooth transitions. Raman spectroscopy experiments[176] demonstrate that the solid-liquid phase transitions of confined water in CNTs are extremely diameter dependent, freezing transitions at temperatures between 378 K and 424 K for 1.05 nm SWCNTs were observed. These results are in good agreement with our theoretical predictions: as shown in Fig. 4.4, phase transition temperatures exhibit extreme sensitivity to the diameter of CNTs. We also observed that the phase transition temperature decreases as the diameter of CNTs increases. The phase transition temperatures observed in our MD simulations are substantially higher than the values predicted by previous MD simulations[58, 62, 70] and can be attributed to the different potentials employed in the MD simulations.

Additionally, we showed that neither a clear transition temperature nor a latent heat can be defined for water in 0.95 nm diameter CNT (7,7). We observed only a slight inflection of the curve of energy representation for water inside 1.08 nm diameter CNT $(8,8)$. This conclusion is consistent with the publication[176] that reported the existence of a continuous freezing transition in CNTs of diameter 1.06 nm. In our MD simulations, we detected first–order melting–like phase transitions at temperatures 362 K and 285 K for water inside 1.22 nm diameter CNT (9,9) and 1.35 nm diameter CNT(10,10). These solid–liquid critical points were confirmed in the experimental results of Ref. [176], and prove that first–order transitions occur in larger tubes of diameter 1.15 nm - 1.52 nm.

Our observation of the existence of ferroelectric INTs at high temperatures is counterintuitive, when taking into account the temperature range 57 K–66 K of bulk ferroelectric ice. We observe substantial ferroelectric INTs around ambient temperature for CNTs (8,8), (9,9) and (10, 10), providing theoretical support for possible applications to fuel-cells and electrolyzers.[70, 71, 177]

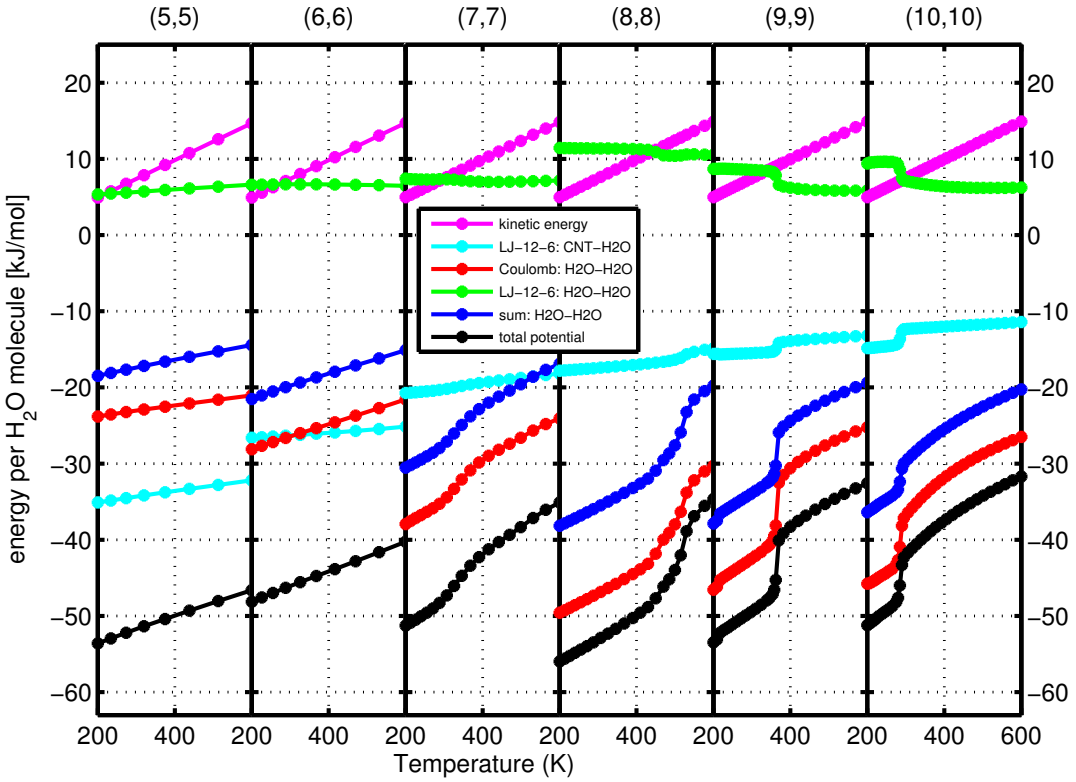

Figure 4.4: Decomposition of total energy in REMD simulations of water confined inside armchair CNT (n, n), $5 \leq n \leq 10$ as a function of temperature. For $\eta = 1$ kJ/mol, $\delta = 1$, and for the TIP5P water model.

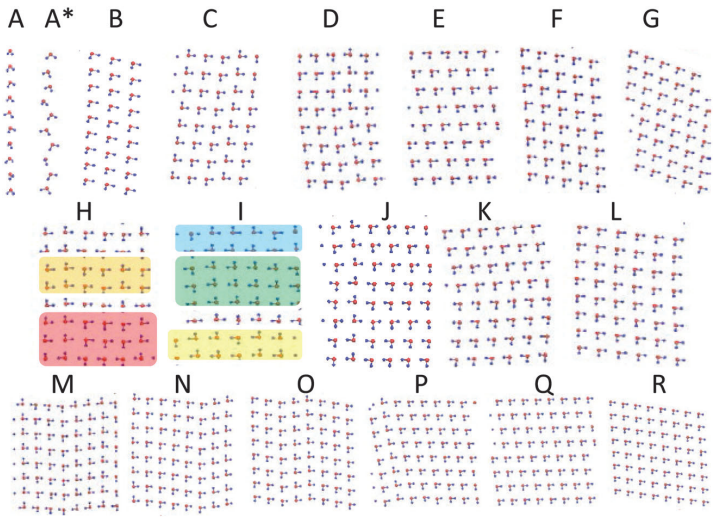

Figure 4.5: End views of selected minimum energy structures of INTs confined inside low diameter CNTs. (C): INT $\langle 3,1\rangle$ inside CNT (7,7); (E-G): INT $\langle 5,0\rangle$, $\langle 5,1\rangle$, $\langle 5,2\rangle$ inside CNT (8,8); (K-L): INT $\langle 6,0\rangle$, $\langle 6,1\rangle$ inside CNT (9,9); (Q-S): INT $\langle 8,0\rangle$, $\langle 8,1\rangle$ inside CNT (10,10).

On the one hand, motivated by the finding of nearly square quasi–2D ice structures[82] 2015, we investigated quasi–2D water between two layers of graphene at a distance of 0.65 nm using SPCE, TIP3P, TIP4P, TIP4P/ICE and TIP5P water models. In a first series of simulation, we demonstrated that neither total water–carbon interaction strength η, nor the corresponding anisotropy parameter δ, have notable effects on the water occupancy at high pressure (1000 MPa). We determined the water occupancy of a 0.65 nm graphene slit under high presssure (P=1000 MPa) using the water–carbon force field parameter $\eta = 1$ kJ/mol and $\delta = 1$, using the five water models stated above.

In the second series of REMD simulation we utilized the water occupancies from the filling simulation and found tetragonal arrangements instead of hexagonal structure in bulk water. These tetragonals arrangements are classified as nearly square or rhombic, and they are water model–dependent. For example, nearly square and rhombic arrangements are found for the SPCE and TIP4P water models, but only nearly square patterns are found for the TIP4P/ICE water model; only rhombic patterns are detected in the case of TIP3P and TIP5P water models.

Interestingly, these 2D water structures shown in paper A3 are similar with the water networks of paper A2 when unrolling the single–walled ice nanotubes. We can conclude that the near–zero, medium, or strong tilt of the tetragons shown in Fig. 4.6 are comparable with the unrolled INT structures classified as prism-like, single helix, or double helix, respectively displayed in Fig. 4.5.

The second novel propery for the quasi–2D ices is they exhibit proton ordering behaviour, as shown by the presence of ferroelectric, ferrielectric and antiferroelectric structures. As with the oxygen network, the proton ordering is also water model-dependent. Antiferroelectric structures are found for SPCE, TIP4P and TIP4P/ICE, ferrielectric arrangements are found for SPCE and TIP3P, whereas, fer-

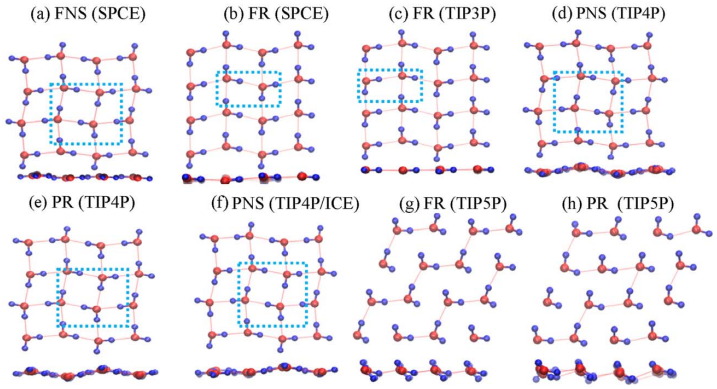

Figure 4.6: Minimum energy structures of water confined inside a graphene nanocapillary for various water models indicated in brackets. Here, the blue rectangles are unit cells. The structures are denoted as follows: F = flat; P = puckered; N = nearly; S= square and R = rhombic, respectively.

roelectric quasi-2D ice is detected only for TIP5P.

In addition to different oxygen arrangements and proton ordering of 2D–ice, the phase transitions between them were investigated and classified as first–order and second–order transitions. The temperatures of these phase transitions are strongly dependent on the water models. The first–order phase transition temperatures range between 424 K (TIP4P) and 577 K (SPCE). All of these phase transition temperatures are much higher by a factor of between 1.5 and 3 than the corresponding temperatures found in simulations of bulk water using the same water models. There is an exception for the phase transition temperature and energy which are 297 K and 0.23 kJ/mol for TIP5P. A possible explanation is that the water molecules in the TIP5P model form significantly weaker hydrogen bonds, as shown in Fig. 4.7.

Another intriguing class of temperature-dependent phase transitions are the second–order ice–ice transitions that do not involve latent heat. Some examples are the FNS–FR transition found for the SPCE water model between $T = 283K$ and $T = 296K$, the PNS–PR transition found for TIP4P between $T = 245K$ and $T = 256K$ and the FR–PR transition found for TIP5P between $T = 229K$ and $T = 238K$. For the example of the SPCE water model, we further quantitatively investigated the thermodynamic stability of FR versus FNS ice by analysing the free energy difference ΔA, at different simulation temperatures. We obtained the entropy difference ΔS ($\approx$ 0.02kJ/mol/K) as well as the enthalpy difference ($\approx$ 5.66 kJ/mol), see Fig. 4.8 (a). Alternatively, ΔU can also be obtained via the Gibbs—Helmholtz equation,[178] which yields approximately 5.73kJ/mol, see Fig. 4.8 (b). Hence, the FNS ice phase is enthalpically favorable. However, the entropy of the FR phase is higher. Thus, the transition from phase FNS to FR is spontaneous whenΔA becomes negetive for $T > 283$ K.

In conclusion, in this thesis, I co–derived two sets of LJ parameters for the interaction of water–carbon sheets with different curvature, by fitting to our high quality DF-LCCSD(T) quantum chem-

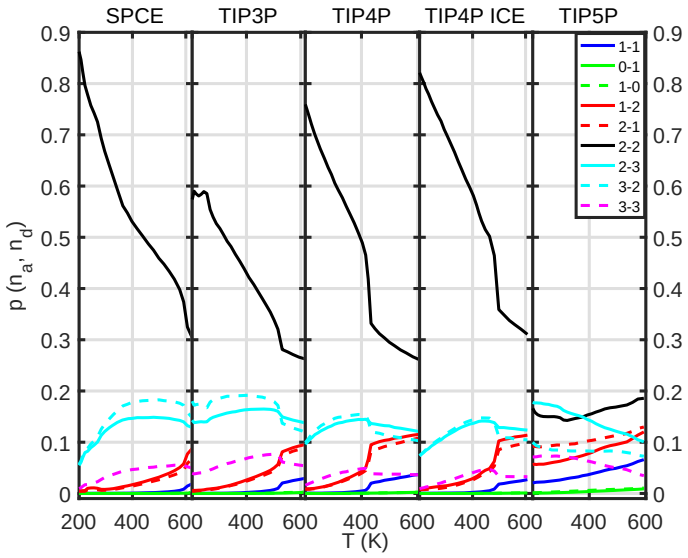

Figure 4.7: H–bonding pattern of water confined inside a graphene nanocapillary as a function of temperature. Obtained from REMD simulations with $\eta = 1$ kJ/mol, $\delta = 1$, and for SPCE, TIP3P, TIP4P, TIP4P/ICE, and TIP5P water models. The curves indicate the joint probabilities, p_{n_a,n_b}, of a water molecule acting n_a times as an acceptor and n_d times as a donor, as indicated in the figure legend.

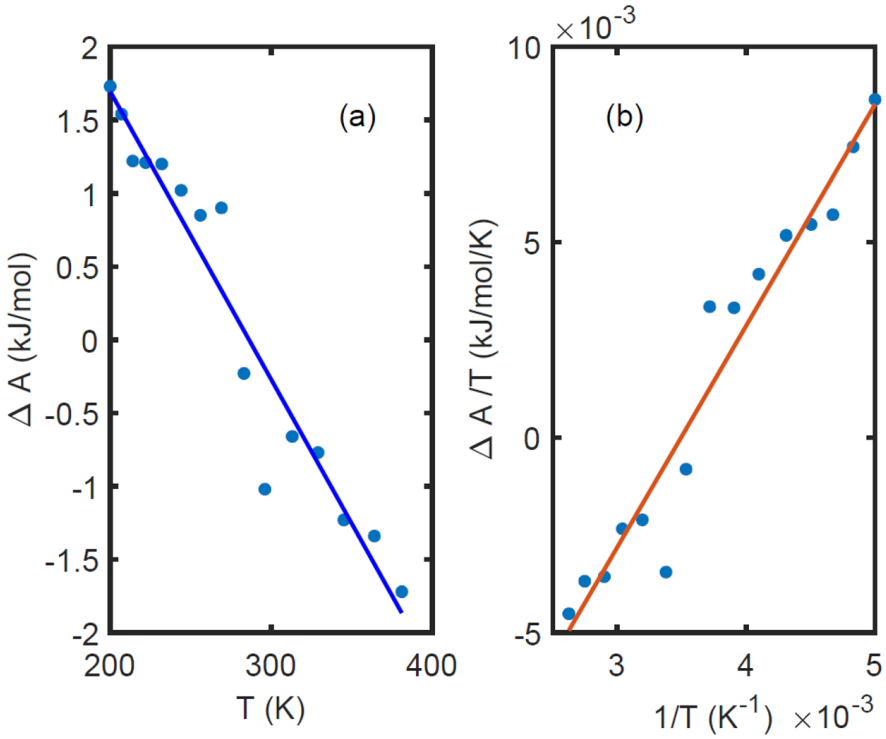

Figure 4.8: Helmholtz free energy difference ΔA between FNS and FR ice phases as a function of temperature between 200 K and 381 K, the slope corresponds to the entropy difference. The linear regression provides entropy and enthalpy difference, see main text. (b) Gibbs–Helmholtz representation of $\Delta A/T$ versus $1/T$ leading to ΔU.

istry results. The another aim of this thesis is to provide a systematic comparison between the water occupancy and structure properities predicted under carbon material nanoscopic confinement by different water–carbon interaction strength and five widely employed classical water models. And our study showed a complete study of quasi-1D ice confined inside CNTs and quasi-2D ice confined between two graphene layers at different pressures and various temperatures from both classical relaxation and classical molecular dynamics (also employing the REMD method). In this thesis, an exhaustive analysis of the water occupancy of open-ended CNTs and graphene capillaries was carried out. This analysis showed that the anisotropy parameter δ of water–carbond interaction does not have significant influence on water occupancy for either CNTs or graphene capillaries. However, the analysis shows that the total water–carbon interaction strength parameter η exhibits a clear threshold that separates a hydrophobic regime from a hydrophilic regime for CNTs. This threshold is not observed for graphene capillaries. A key finding of our analysis is that using different water models has only a minor influence on water occupancy for both CNTs and graphene capillaries. On the other hand, our results showed that oxygen arrangements, proton ordering and phase transition properties (not only between different networks of the oxygen atoms but also between different proton–ordering patterns), including the temperatures of melting–like transitions and latent heat, do depend significantly on the water model used. We reported second–order phase transitions by the use of the enhanced sampling method (REMD) to overcome sampling problems related to rare events which cannot be overcome by conventional MD simulations on a nanosecond timescale. We conclude that there is not a single water model able to reproduce all the water properties.

Chapter 5

Outlook

In this thesis, we presented the results of systematic investigation of the structures predicted by water models under confinement inside carbon nanomaterials. Many important questions still remain. Future work will seek to address these questions.

First, the high fluidity of water in confined geometries is an important direction and worth to investigate using MD simulation. Due to it relevants to the processes ranging from tribology to protein folding, and its molecular mobility in pores and slits.[179] Moreover, the physical nature behind the high circulation characteristics is not yet clear, e.g., what happens to the structure of confined water when changes from high fluidity to ordinary fluidity?

Second, Transport of molecules through molecular pores is essential for many biological and technical processes.[51] Molecular transport through these low–dimensional pores is highly collective, since motion of a molecule requires concomitant motion of all molecules in the file.[5, 180] My another interesting focus could be the chirality effect of CNTs on the water transport behavior. And how to develop the application for the promising high-selectivity and high-flux membranes in molecular separation devices.

Third, Nanoconfined water fast proton transport through CNTs suggests a good application prospect[38] in fuel cell. Proton-conducting materials are used as the electrolyte for low- and intermediate temperature fuel cells, which are currently attracting significant interest. The electrolyte is the heart of any fuel cell,[181] this component effectively separates the anode and cathode gases or liquids. The electrochemical reaction occurring at the electrodes through conducting a specific ion at very high rates during the operation of the fuel cell.

Last but not least significant application value is water desalination using CNTs–enhanced membrane distillation.[182] CNTs in different types of membranes alter the solute-membrane interactions, which is one of the major physicochemical factors affecting the permeability and selectivity of a membrane.

Bibliography

[1] G. S. Kell, "Density, thermal expansivity, and compressibility of liquid water from 0.deg. to 150.deg.. correlations and tables for atmospheric pressure and saturation reviewed and expressed on 1968 temperature scale", J. Chem. Eng. Data **20**, 97–105 (1975) (cit. on p. 1).

[2] Q. Zheng, D. J. Durben, G. H. Wolf, and C. A. Angell, "Liquids at large negative pressures: water at the homogeneous nucleation limit", Science **254**, 829–832 (1991) (cit. on p. 1).

[3] P. H. Poole, F. Sciortino, U. Essmann, and H. E. Stanley, "Phase behaviour of metastable water", Nature **360**, 324–328 (1992) (cit. on p. 1).

[4] T. Ohba, "Size-dependent water structures in carbon nanotubes", Angew. Chemie - Int. Ed. **53**, 8032–8036 (2014) (cit. on p. 1).

[5] K. Falk, F. Sedlmeier, L. Joly, R. R. Netz, and L. Bocquet, "Molecular origin of fast water transport in carbon nanotube membranes: superlubricity versus curvature dependent friction", Nano Lett. **10**, 4067–4073 (2010) (cit. on pp. 1, 103).

[6] J. L. Finney, "Water? what's so special about it?", Philos. Trans. R. Soc. B Biol. Sci. **359**, 1145–1165 (2004) (cit. on p. 1).

[7] D. Chandler, "Interfaces and the driving force of hydrophobic assembly", Nature **437**, 640–647 (2005) (cit. on p. 1).

[8] C. E. Bertrand, Y. Zhang, and S.-H. Chen, "Deeply-cooled water under strong confinement: neutron scattering investigations and the liquid–liquid critical point hypothesis", Phys. Chem. Chem. Phys. **15**, 721–745 (2013) (cit. on p. 1).

[9] J. Carrasco, A. Hodgson, and A. Michaelides, "A molecular perspective of water at metal interfaces", Nat. Mater. **11**, 667–674 (2012) (cit. on p. 1).

[10] Y. Gao, S. Kim, S. Zhou, H.-C. Chiu, D. Nélias, C. Berger, W. de Heer, L. Polloni, R. Sordan, A. Bongiorno, and E. Riedo, "Elastic coupling between layers in two-dimensional materials", Nat. Mater. **14**, 714–720 (2015) (cit. on p. 1).

[11] W. L. Jorgensen and J. Tirado-Rives, "The opls potential functions for proteins. energy minimizations for crystals of cyclic peptides and crambin", J. Am. Chem. Soc. **110**, 1657–1666 (1988) (cit. on pp. 2, 10).

[12] W. L. Jorgensen, D. S. Maxwell, and J. Tirado-Rives, "Development and testing of the opls all-atom force field on conformational energetics and properties of organic liquids", J. Am. Chem. Soc. **118**, 11225–11236 (1996) (cit. on p. 2).

[13] H. Berendsen, D. van der Spoel, and R. Drunen, "A message-passing parallel molecular dynamics implementation.", Computer Physics Communications **91**, 43–56 (1995) (cit. on p. 2).

[14] E. Lindahl, B. Hess, and D. van der Spoel, "Gromacs 3.0: a package for molecular simulation and trajectory analysis", J. Mol. Model. **7**, 306–317 (2001) (cit. on p. 2).

[15] B. Hess, C. Kutzner, D. Van Der Spoel, and E. Lindahl, "Grgmacs 4: algorithms for highly efficient, load-balanced, and scalable molecular simulation", J. Chem. Theory Comput. **4**, 435–447 (2008) (cit. on p. 2).

[16] E. Voloshina, D. Usvyat, M. Schütz, Y. Dedkov, and B. Paulus, "On the physisorption of water on graphene: a ccsd(t) study.", Phys. Chem. Chem. Phys. **13**, 12041–12047 (2011) (cit. on p. 2).

[17] S. Iijima, "Helical microtubules of graphitic carbon", Nature **354**, 56–58 (1991) (cit. on p. 3).

[18] A. K. Geim and K. S. Novoselov, "The rise of graphene.", Nat. Mater. **6**, 183–191 (2007) (cit. on p. 3).

[19] G Dresselhaus, S. Riichiro, et al., *Physical properties of carbon nanotubes* (World scientific, 1998) (cit. on p. 3).

[20] S. Reich, C. Thomsen, and J. Maultzsch, *Carbon nanotubes: basic concepts and physical properties* (John Wiley & Sons, 2008) (cit. on p. 3).

[21] A. Kalra, S. Garde, and G. Hummer, "Osmotic water transport through carbon nanotube membranes.", Proc. Natl. Acad. Sci. U. S. A. **100**, 10175–10180 (2003) (cit. on p. 3).

[22] J. K. Holt, H. G. Park, Y. Wang, M. Stadermann, A. B. Artyukhin, C. P. Grigoropoulos, A. Noy, and O. Bakajin, "Fast mass transport through sub-2-nanometer carbon nanotubes.", Science **312**, 1034–1037 (2006) (cit. on p. 3).

[23] X. Qin, Q. Yuan, Y. Zhao, S. Xie, and Z. Liu, "Measurement of the rate of water translocation through carbon nanotubes", Nano Lett. **11**, 2173–2177 (2011) (cit. on p. 3).

[24] G. Hummer, J. C. Rasaiah, and J. P. Noworyta, "Water conduction through the hydrophobic channel of a carbon nanotube.", Nature **414**, 188–190 (2001) (cit. on pp. 3, 91).

[25] F. Zhu and K. Schulten, "Water and proton conduction through carbon nanotubes as models for biological channels.", Biophys. J. **85**, 236–244 (2003) (cit. on p. 3).

[26] M. Majumder, N. Chopra, R. Andrews, and B. J. Hinds, "Nanoscale hydrodynamics: enhanced flow in carbon nanotubes", Nature **438**, 44 (2005) (cit. on p. 3).

[27] S. Joseph and N. R. Aluru, "Why are carbon nanotubes fast transporters of water?", Nano Lett. **8**, 452–458 (2008) (cit. on p. 3).

[28] J. Thomas and A. McGaughey, "Water flow in carbon nanotubes: transition to subcontinuum transport", Phys. Rev. Lett. **102**, 1–4 (2009) (cit. on p. 3).

[29] M. Melillo, F. Zhu, M. A. Snyder, and J. Mittal, "Water transport through nanotubes with varying interaction strength between tube wall and water", J. Phys. Chem. Lett. **2**, 2978–2983 (2011) (cit. on p. 3).

[30] D. J. Bonthuis, K. F. Rinne, K. Falk, C Nadir Kaplan, D. Horinek, A Nihat Berker, L. Bocquet, and R. R. Netz, "Theory and simulations of water flow through carbon nanotubes: prospects and pitfalls.", J. Phys. Condens. Matter **23**, 184110 (2011) (cit. on p. 3).

[31] A. Kolesnikov, J.-M. Zanotti, C.-K. Loong, P. Thiyagarajan, A. Moravsky, R. Loutfy, and C. Burnham, "Anomalously soft dynamics of water in a nanotube: a revelation of nanoscale confinement", Phys. Rev. Lett. **93**, 35503 (2004) (cit. on p. 3).

[32] H. Kyakuno, M. Fukasawa, R. Ichimura, K. Matsuda, Y. Nakai, Y. Miyata, T. Saito, and Y. Maniwa, "Diameter-dependent hydrophobicity in carbon nanotubes", J. Chem. Phys. **145**, 064514 (2016) (cit. on p. 3).

[33] H. Kyakuno, K. Matsuda, H. Yahiro, Y. Inami, T. Fukuoka, Y. Miyata, K. Yanagi, Y. Maniwa, H. Kataura, T. Saito, M. Yumura, and S. Iijima, "Confined water inside single-walled carbon nanotubes: global phase diagram and effect of finite length", J. Chem. Phys. **134**, 244501 (2011) (cit. on pp. 3, 4).

[34] S. Cambré, B. Schoeters, S. Luyckx, E. Goovaerts, and W. Wenseleers, "Experimental observation of single-file water filling of thin single-wall carbon nanotubes down to chiral index (5,3)", Phys. Rev. Lett. **104**, 207401 (2010) (cit. on p. 3).

[35] H.-J. Wang, X.-K. Xi, A. Kleinhammes, and Y. Wu, "Temperature-induced hydrophobic-hydrophilic transition observed by water adsorption.", Science **322**, 80–83 (2008) (cit. on p. 3).

[36] Y. Maniwa, H. Kataura, M. Abe, S. Suzuki, Y. Achiba, H. Kira, and K. Matsuda, "Phase transition in confined water inside carbon nanotubes", J. Phys. Soc. Japan **71**, 2863–2866 (2002) (cit. on p. 3).

[37] A.I. Kolesnikov, C.-K. Loong, N. R. de Souza, C. J. Burnham, and A. P. Moravsky, "Anomalously soft dynamics of water in carbon nanotubes", Phys. B Condens. Matter **385-386**, 272–274 (2006) (cit. on p. 3).

[38] J. K. Holt, H. G. Park, Y. Wang, M. Stadermann, A. B. Artyukhin, C. P. Grigoropoulos, A. Noy, and O. Bakajin, "Fast mass transport through sub-2-nanometer carbon nanotubes.", Science **312**, 1034–1037 (2006) (cit. on pp. 3, 103).

[39] O. Byl, J.-C. Liu, Y. Wang, W.-L. Yim, J. K. Johnson, and J. T. Yates, "Unusual hydrogen bonding in water-filled carbon nanotubes.", J. Am. Chem. Soc. **128**, 12090–12097 (2006) (cit. on p. 3).

[40] Y. Maniwa, H. Kataura, M. Abe, A. Udaka, S. Suzuki, Y. Achiba, H. Kira, K. Matsuda, H. Kadowaki, and Y. Okabe, "Ordered water inside carbon nanotubes: formation of pentagonal to octagonal ice-nanotubes", Chem. Phys. Lett. **401**, 534–538 (2005) (cit. on p. 3).

[41] J. Martí and M. C. Gordillo, "Effects of confinement on the vibrational spectra of liquid water adsorbed in carbon nanotubes", Phys. Rev. B **63**, 165430 (2001) (cit. on p. 3).

[42] J. Martí and M. C. Gordillo, "Temperature effects on the static and dynamic properties of liquid water inside nanotubes", Phys. Rev. E **64**, 021504 (2001) (cit. on p. 3).

[43] J. Martí and M. C. Gordillo, "Time-dependent properties of liquid water isotopes adsorbed in carbon nanotubes", J. Chem. Phys. **114**, 10486 (2001) (cit. on p. 3).

[44] L. Wu, F. Wu, J. Kou, H. Lu, and Y. Liu, "Effect of the position of constriction on water permeation across a single-walled carbon nanotube", Phys. Rev. E - Stat. Nonlinear, Soft Matter Phys. **83**, 1–8 (2011) (cit. on p. 3).

[45] Z. He, J. Zhou, X. Lu, and B. Corry, "Ice-like water structure in carbon nanotube (8,8) induces cationic hydration enhancement", J. Phys. Chem. C **117**, 11412–11420 (2013) (cit. on p. 3).

[46] W. Zhao, L. Wang, J. Bai, J. S. Francisco, and X. C. Zeng, "Spontaneous formation of one-dimensional hydrogen gas hydrate in carbon nanotubes", J. Am. Chem. Soc. **136**, 10661–10668 (2014) (cit. on p. 3).

[47] M. C. Gordillo and J Martí, "Hydrogen bond structure of liquid water confined in nanotubes", Chem. Phys. Lett. **329**, 341–345 (2000) (cit. on p. 3).

[48] A. Alexiadis and S. Kassinos, "Molecular simulation of water in carbon nanotubes", Chem. Rev. **108**, 5014–5034 (2008) (cit. on pp. 3, 91).

[49] L. Xu and V. Molinero, "Is There a Liquid–Liquid Transition in Confined Water?", J. Phys. Chem. B **115**, 14210–14216 (2011) (cit. on pp. 3, 5).

[50] F. Klameth and M. Vogel, "Structure and dynamics of supercooled water in neutral confinements", J. Chem. Phys. **138**, 134503 (2013) (cit. on p. 3).

[51] A. Berezhkovskii and G. Hummer, "Single-file transport of water molecules through a carbon nanotube", Phys. Rev. Lett. **89**, 064503 (2002) (cit. on pp. 3, 91, 103).

[52] C. Dellago, M. Naor, and G. Hummer, "Proton transport through water-filled carbon nanotubes", Phys. Rev. Lett. **90**, 105902 (2003) (cit. on p. 3).

[53] J. Köfinger, G. Hummer, and C. Dellago, "Macroscopically ordered water in nanopores.", Proc. Natl. Acad. Sci. U. S. A. **105**, 13218–13222 (2008) (cit. on pp. 3, 4).

[54] L. Wang, J. Zhao, F. Li, H. Fang, and J. P. Lu, "First-principles study of water chains encapsulated in single-walled carbon nanotube", J. Phys. Chem. C **113**, 5368–5375 (2009) (cit. on p. 3).

[55] W. H. Noon, K. D. Ausman, R. E. Smalley, and J. Ma, "Helical ice-sheets inside carbon nanotubes in the physiological condition", Chem. Phys. Lett. **355**, 445–448 (2002) (cit. on p. 3).

[56] J. Wang, Y. Zhu, J. Zhou, and X.-H. Lu, "Diameter and helicity effects on static properties of water molecules confined in carbon nanotubes", Phys. Chem. Chem. Phys. **6**, 829 (2004) (cit. on p. 3).

[57] J. Bai, J. Wang, and X. C. Zeng, "Multiwalled ice helixes and ice nanotubes.", Proc. Natl. Acad. Sci. U. S. A. **103**, 19664–19667 (2006) (cit. on p. 3).

[58] D. Takaiwa, I. Hatano, K. Koga, and H. Tanaka, "Phase diagram of water in carbon nanotubes.", Proc. Natl. Acad. Sci. U. S. A. **105**, 39–43 (2008) (cit. on pp. 3, 4, 91, 96).

[59] A. Alexiadis and S. Kassinos, "Molecular simulation of water in carbon nanotubes.", Chem. Rev. **108**, 5014–5034 (2008) (cit. on p. 3).

[60] J. Bai, C.-R. Su, R. D. Parra, X. C. Zeng, H. Tanaka, K. Koga, and J.-M. Li, "Ab initio studies of quasi-one-dimensional pentagon and hexagon ice nanotubes", J. Chem. Phys. **118**, 3913 (2003) (cit. on p. 3).

[61] K. Koga, R. D. Parra, H. Tanaka, and X. C. Zeng, "Ice nanotube: what does the unit cell look like?", J. Chem. Phys. **113**, 5037 (2000) (cit. on pp. 3, 91).

[62] K Koga, G. T. Gao, H Tanaka, and X. C. Zeng, "Formation of ordered ice nanotubes inside carbon nanotubes.", Nature **412**, 802–805 (2001) (cit. on pp. 3, 4, 91, 96).

[63] S. Li and B. Schmidt, "Molecular dynamics simulations of proton-ordered water confined in low-diameter carbon nanotubes", Phys. Chem. Chem. Phys. **17**, 7303–7316 (2015) (cit. on pp. 3–5, 91).

[64] Y. Liu, Q. Wang, T. Wu, and L. Zhang, "Fluid structure and transport properties of water inside carbon nanotubes.", J. Chem. Phys. **123**, 234701 (2005) (cit. on p. 3).

[65] Y. Liu and Q. Wang, "Transport behavior of water confined in carbon nanotubes", Phys. Rev. B **72**, 085420 (2005) (cit. on p. 3).

[66] R. J. Mashl, S. Joseph, N. R. Aluru, and E. Jakobsson, "Anomalously immobilized water: a new water phase induced by confinement in nanotubes", Nano Lett. **3**, 589–592 (2003) (cit. on p. 3).

[67] R. J. Mashl, S. Joseph, N. R. Aluru, and E. Jakobsson, "Anomalously immobilized water: a new water phase induced by confinement in nanotubes", Nano Lett. **3**, 589–592 (2003) (cit. on p. 3).

[68] J. Bai, C. R. Su, R. D. Parra, X. C. Zeng, H. Tanaka, K. Koga, and J. M. Li, "Ab initio studies of quasi-one-dimensional pentagon and hexagon ice nanotubes", J. Chem. Phys. **118**, 3913–3916 (2003) (cit. on p. 3).

[69] R. J. Mashl, S. Joseph, N. R. Aluru, and E. Jakobsson, "Anomalously immobilized water: a new water phase induced by confinement in nanotubes", Nano Lett. **3**, 589–592 (2003) (cit. on p. 3).

[70] C. Luo, W. Fa, J. Zhou, J. Dong, and X. C. Zeng, "Ferroelectric ordering in ice nanotubes confined in carbon nanotubes.", Nano Lett. **8**, 2607–2612 (2008) (cit. on pp. 3, 91, 96).

[71] F. Mikami, K. Matsuda, H. Kataura, and Y. Maniwa, "Dielectric properties of water inside single-walled carbon nanotubes.", ACS Nano **3**, 1279–87 (2009) (cit. on pp. 3, 96).

[72] J. Wang, Y. Zhu, J. Zhou, and X.-H. Lu, "Diameter and helicity effects on static properties of water molecules confined in carbon nanotubes", Phys. Chem. Chem. Phys. **6**, 829 (2004) (cit. on p. 3).

[73] Y. Nakamura and T. Ohno, "Ferroelectric mobile water", Phys. Chem. Chem. Phys. **13**, 1064–1069 (2011) (cit. on p. 3).

[74] L. Pauling, "The structure and entropy of ice and of other crystals with some randomness of atomic arrangement", J. Am. Chem. Soc. **57**, 2680–2684 (1935) (cit. on p. 4).

[75] Y. Nakamura and T. Ohno, "Structure of water confined inside carbon nanotubes and water models", Mater. Chem. Phys. **132**, 682–687 (2012) (cit. on p. 4).

[76] J. Shiomi, T. Kimura, and S. Maruyama, "Molecular dynamics of ice-nanotube formation inside carbon nanotubes", J. Phys. Chem. C **111**, 12188–12193 (2007) (cit. on p. 4).

[77] M Sadeghi and G. A. Parsafar, "Toward an equation of state for water inside carbon nanotubes.", J. Phys. Chem. B **116**, 4943–4951 (2012) (cit. on p. 4).

[78] K. T. He, J. D. Wood, G. P. Doidge, E. Pop, and J. W. Lyding, "Scanning tunneling microscopy study and nanomanipulation of graphene-coated water on mica", Nano Lett. **12**, 2665–2672 (2012) (cit. on p. 4).

[79] D.-S. Yang and A. H. Zewail, "Ordered water structure at hydrophobic graphite interfaces observed by 4d, ultrafast electron crystallography", Proc. Natl. Acad. Sci. **106**, 4122–4126 (2009) (cit. on p. 4).

[80] Y. Zheng, C. Su, J. Lu, and K. P. Loh, "Room-temperature ice growth on graphite seeded by nano-graphene oxide", Angew. Chemie Int. Ed. **52**, 8708–8712 (2013) (cit. on p. 4).

[81] G. a. Kimmel, J. Matthiesen, M. Baer, C. J. Mundy, N. G. Petrik, R. S. Smith, Z. Dohnalek, and B. D. Kay, "No confinement needed: observation of a metastable hydrophobic wetting two-layer ice on graphene", J. Am. Chem. Soc. **131**, 12838–12844 (2009) (cit. on p. 4).

[82] G. Algara-Siller, O. Lehtinen, F. C. Wang, R. R. Nair, U. Kaiser, H. A. Wu, A. K. Geim, and I. V. Grigorieva, "Square ice in graphene nanocapillaries", Nature **519**, 443–445 (2015) (cit. on pp. 4, 91, 96).

[83] R. Zangi, "Water confined to a slab geometry: a review of recent computer simulation studies", J. Phys. Condens. Matter **16**, S5371–S5388 (2004) (cit. on p. 4).

[84] R. Zangi and A. E. Mark, "Electrofreezing of confined water", J. Chem. Phys. **120**, 7123 (2004) (cit. on p. 4).

[85] J. C. Johnston, N. Kastelowitz, and V. Molinero, "Liquid to quasicrystal transition in bilayer water", J. Chem. Phys. **133**, 154516 (2010) (cit. on p. 4).

[86] R. Zangi and A. E. Mark, "Monolayer ice", Phys. Rev. Lett. **91**, 025502 (2003) (cit. on pp. 4, 5).

[87] R. Zangi and A. E. Mark, "Bilayer ice and alternate liquid phases of confined water", J. Chem. Phys. **119**, 1694–1700 (2003) (cit. on p. 4).

[88] T. Kaneko, J. Bai, K. Yasuoka, A. Mitsutake, and X. C. Zeng, "Liquid-solid and solid-solid phase transition of monolayer water: high-density rhombic monolayer ice", J. Chem. Phys. **140**, 184507 (2014) (cit. on pp. 4, 5).

[89] F. de los Santos and G. Franzese, "Relations between the diffusion anomaly and cooperative rearranging regions in a hydrophobically nanoconfined water monolayer", Phys. Rev. E **85**, 010602 (2012) (cit. on p. 4).

[90] E. G. Strekalova, M. G. Mazza, H. E. Stanley, and G. Franzese, "Large decrease of fluctuations for supercooled water in hydrophobic nanoconfinement", Phys. Rev. Lett. **106**, 145701 (2011) (cit. on p. 4).

[91] M. G. Mazza, K. Stokely, H. E. Stanley, and G. Franzese, "Effect of pressure on the anomalous response functions of a confined water monolayer at low temperature", J. Chem. Phys. **137**, 204502 (2012) (cit. on p. 4).

[92] S. Han, M. Y. Choi, P. Kumar, and H. E. Stanley, "Phase transitions in confined water nanofilms", Nat. Phys. **6**, 685–689 (2010) (cit. on pp. 4, 5).

[93] J. Bai and X. C. Zeng, "Polymorphism and polyamorphism in bilayer water confined to slit nanopore under high pressure", Proc. Natl. Acad. Sci. **109**, 21240–21245 (2012) (cit. on p. 4).

[94] N. Giovambattista, P. J. Rossky, and P. G. Debenedetti, "Phase transitions induced by nanoconfinement in liquid water", Phys. Rev. Lett. **102**, 050603 (2009) (cit. on pp. 4, 5).

[95] J. Bai, X. C. Zeng, K. Koga, and H. Tanaka, "Formation of quasi two-dimensional bilayer ice in hydrophobic slits: a possible candidate for ice xiii?", Mol. Simul. **29**, 619–626 (2003) (cit. on p. 4).

[96] L. B. Krott and M. C. Barbosa, "Anomalies in a waterlike model confined between plates", J. Chem. Phys. **138**, 084505 (2013) (cit. on p. 4).

[97] K. Koga, X. C. Zeng, and H. Tanaka, "Freezing of confined water: a bilayer ice phase in hydrophobic nanopores", Phys. Rev. Lett. **79**, 5262–5265 (1997) (cit. on p. 4).

[98] N. Giovambattista, P. J. Rossky, and P. G. Debenedetti, "Effect of pressure on the phase behavior and structure of water confined between nanoscale hydrophobic and hydrophilic plates", Phys. Rev. E **73**, 041604 (2006) (cit. on p. 4).

[99] P. Kumar, S. V. Buldyrev, F. W. Starr, N. Giovambattista, and H. E. Stanley, "Thermodynamics, structure, and dynamics of water confined between hydrophobic plates", Phys. Rev. E **72**, 051503 (2005) (cit. on p. 4).

[100] M. Meyer and H. E. Stanley, "Liquidliquid phase transition in confined water: a monte carlo study", J. Phys. Chem. B **103**, 9728–9730 (1999) (cit. on p. 4).

[101] P. Kumar, F. W. Starr, S. V. Buldyrev, and H. E. Stanley, "Effect of water-wall interaction potential on the properties of nanoconfined water", Phys. Rev. E **75**, 011202 (2007) (cit. on p. 4).

[102] H. Mosaddeghi, S. Alavi, M. H. Kowsari, and B. Najafi, "Simulations of structural and dynamic anisotropy in nano-confined water between parallel graphite plates", J. Chem. Phys. **137**, 184703 (2012) (cit. on p. 4).

[103] F. Corsetti, J. Zubeltzu, and E. Artacho, "Enhanced configurational entropy in high-density nanoconfined bilayer ice", Phys. Rev. Lett. **116**, 1–5 (2016) (cit. on p. 4).

[104] W.-H. Zhao, J. Bai, L. Wang, L.-F. Yuan, J. Yang, J. S. Francisco, and X. C. Zeng, "Formation of bilayer clathrate hydrates", J. Mater. Chem. A **3**, 5547–5555 (2015) (cit. on p. 4).

[105] K. Koga, H. Tanaka, and X. C. Zeng, "First-order transition in confined water between high-density liquid and low-density amorphous phases", Nature **408**, 564–567 (2000) (cit. on pp. 4, 5).

[106] K. Koga and H. Tanaka, "Phase diagram of water between hydrophobic surfaces", J. Chem. Phys. **122**, 104711 (2005) (cit. on pp. 4, 5).

[107] T. Werder, J. H. Walther, R. L. Jaffe, T. Halicioglu, and P. Koumoutsakos, "On the watercarbon interaction for use in molecular dynamics simulations of graphite and carbon nanotubes", J. Phys. Chem. B **107**, 1345–1352 (2003) (cit. on p. 4).

[108] Y. Zhu, F. Wang, J. Bai, X. C. Zeng, and H. Wu, "Compression limit of two-dimensional water constrained in graphene nanocapillaries", ACS Nano **9**, 12197–12204 (2015) (cit. on pp. 4, 5, 91).

[109] W.-H. Zhao, L. Wang, J. Bai, L.-F. Yuan, J. Yang, and X. C. Zeng, "Highly confined water: two-dimensional ice, amorphous ice, and clathrate hydrates", Acc. Chem. Res. **47**, 2505–2513 (2014) (cit. on p. 4).

[110] G. Cicero, J. C. Grossman, E. Schwegler, F. Gygi, and G. Galli, "Water confined in nanotubes and between graphene sheets : a first principle study", J. Am. Chem. Soc **130**, 1871–1878 (2008) (cit. on p. 4).

[111] A. L. Ferguson, N. Giovambattista, P. J. Rossky, A. Z. Panagiotopoulos, and P. G. Debenedetti, "A computational investigation of the phase behavior and capillary sublimation of water confined between nanoscale hydrophobic plates", J. Chem. Phys. **137**, 144501 (2012) (cit. on pp. 4, 5).

[112] T. Kaneko, J. Bai, K. Yasuoka, A. Mitsutake, and X. C. Zeng, "New computational approach to determine liquid–solid phase equilibria of water confined to slit nanopores", J. Chem. Theory Comput. **9**, 3299–3310 (2013) (cit. on p. 4).

[113] H. Qiu and W. Guo, "Electromelting of confined monolayer ice", Phys. Rev. Lett. **110**, 195701 (2013) (cit. on p. 4).

[114] I. Strauss, H. Chan, and P. Král, "Ultralong polarization chains induced by ions solvated in confined water monolayers", J. Am. Chem. Soc. **136**, 1170–1173 (2014) (cit. on p. 4).

[115] W.-H. Zhao, J. Bai, L.-F. Yuan, J. Yang, and X. C. Zeng, "Ferroelectric hexagonal and rhombic monolayer ice phases", Chem. Sci. **5**, 1757 (2014) (cit. on pp. 4, 5).

[116] M. Sobrino Fernandez Mario, M. Neek-Amal, and F. M. Peeters, "Aa-stacked bilayer square ice between graphene layers", Phys. Rev. B **92**, 245428 (2015) (cit. on p. 4).

[117] F. Corsetti, P. Matthews, and E. Artacho, "Structural and configurational properties of nanoconfined monolayer ice from first principles", Sci. Rep. **6**, 18651 (2016) (cit. on p. 4).

[118] J. Chen, G. Schusteritsch, C. J. Pickard, C. G. Salzmann, and A. Michaelides, "Two dimensional ice from first principles: structures and phase transitions", Phys. Rev. Lett. **116**, 025501 (2016) (cit. on pp. 4, 5).

[119] J. Bai, C. A. Angell, and X. C. Zeng, "Guest-free monolayer clathrate and its coexistence with two-dimensional high-density ice", Proc. Natl. Acad. Sci. **107**, 5718–5722 (2010) (cit. on p. 5).

[120] X. Su, L Lianos, Y Shen, and G. Somorjai, "Surface-induced ferroelectric ice on pt(111)", Phys. Rev. Lett. **80**, 1533–1536 (1998) (cit. on p. 5).

[121] M. J. Iedema, M. J. Dresser, D. L. Doering, J. B. Rowland, W. P. Hess, A. A. Tsekouras, and J. P. Cowin, "Ferroelectricity in water ice", J. Phys. Chem. B **102**, 9203–9214 (1998) (cit. on p. 5).

[122] D. N. LeBard and D. V. Matyushov, "Ferroelectric hydration shells around proteins: electrostatics of the proteinwater interface", J. Phys. Chem. B **114**, 9246–9258 (2010) (cit. on p. 5).

[123] C. Spagnoli, K. Loos, A. Ulman, and M. K. Cowman, "Imaging structured water and bound polysaccharide on mica surface at ambient temperature", J. Am. Chem. Soc. **125**, 7124–7128 (2003) (cit. on p. 5).

[124] G. Pérez-Hernández and B. Schmidt, "Anisotropy of the water-carbon interaction: molecular simulations of water in low-diameter carbon nanotubes.", Phys. Chem. Chem. Phys. **15**, 4995–5006 (2013) (cit. on pp. 5, 12, 91).

[125] S. Lei, B. Paulus, S. Li, and B. Schmidt, "Curvature-dependent adsorption of water inside and outside armchair carbon nanotubes", J. Comput. Chem. **37**, 1313–1320 (2016) (cit. on pp. 5, 13).

[126] H. J. C. Berendsen, J. R. Grigera, and T. P. Straatsma, "The missing term in effective pair potentials", J. Phys. Chem. **91**, 6269–6271 (1987) (cit. on pp. 5, 13).

[127] W. L. Jorgensen, J. Chandrasekhar, J. D. Madura, R. W. Impey, and M. L. Klein, "Comparison of simple potential functions for simulating liquid water", J. Chem. Phys. **79**, 926–935 (1983) (cit. on pp. 5, 13).

[128] W. L. Jorgensen and J. D. Madura, "Temperature and size dependence for monte carlo simulations of tip4p water", Mol. Phys. **56**, 1381–1392 (1985) (cit. on pp. 5, 13).

[129] J. L. F. Abascal, E. Sanz, and G. Fernández, (cit. on pp. 5, 13).

[130] M. W. Mahoney and W. L. Jorgensen, "A five-site model for liquid water and the reproduction of the density anomaly by rigid, nonpolarizable potential functions", J. Chem. Phys. **112**, 8910–8922 (2000) (cit. on pp. 5, 13).

[131] R. Swendsen and J. Wang, "Replica monte carlo simulation of spin glasses.", Phys. Rev. Lett. **57**, 2607–2609 (1986) (cit. on pp. 6, 11).

[132] U. H. Hansmann, "Parallel tempering algorithm for conformational studies of biological molecules", Chem. Phys. Lett. **281**, 140–150 (1997) (cit. on pp. 6, 11).

[133] Y. Sugita and Y. Okamoto, "Replica-exchange molecular dynamics method for protein folding", Chem. Phys. Lett. **314**, 141–151 (1999) (cit. on pp. 6, 11).

[134] S. Trebst, M. Troyer, and U. H. E. Hansmann, "Optimized parallel tempering simulations of proteins.", J. Chem. Phys. **124**, 174903 (2006) (cit. on p. 6).

[135] G. J. Willard, *Elementary principles in statistical mechanics* (1902) (cit. on p. 9).

[136] M. Carlo, *Mania* (Los Alamos Sci., 1942) (cit. on p. 9).

[137] D. Frenkel and B. Smit, *Understanding molecular simulation: from algorithms to applications*, Vol. 1 (Elsevier (formerly published by Academic Press), 2002) (cit. on pp. 9, 11–13).

[138] B. J. Alder and T. E. Wainwright, "Phase Transition for a Hard Sphere System", J. Chem. Phys. **27**, 1208–1209 (1957) (cit. on p. 9).

[139] M. Allen, *Tildesley. dj computer simulation of liquids* (Oxford: Clarendon Press, 1987) (cit. on pp. 9, 10).

[140] H. J. Berendsen, *Simulating the physical world: hierarchical modeling from quantum mechanics to fluid dynamics* (Cambridge University Press, 2007) (cit. on p. 9).

[141] F. Jensen, *Introduction to computational chemistry* (John wiley & sons, 2017) (cit. on p. 9).

[142] A. R. Leach and A. R. Leach, *Molecular modelling: principles and applications* (Pearson education, 2001) (cit. on pp. 9, 12).

[143] D. C. Rapaport and D. C. R. Rapaport, *The art of molecular dynamics simulation* (Cambridge university press, 2004) (cit. on p. 10).

[144] D. Frenkel, B. Smit, J. Tobochnik, S. R. McKay, and W. Christian, *Understanding molecular simulation*, Vol. 11, 4 (AIP, 1997), pp. 351–354 (cit. on p. 10).

[145] W. C. Swope, H. C. Andersen, P. H. Berens, and K. R. Wilson, *A computer simulation method for the calculation of equilibrium constants for the formation of physical clusters of molecules: application to small water clusters*, Vol. 76, 1 (AIP, 1982), pp. 637–649 (cit. on p. 10).

[146] C. Schütte and M. Sarich, *Metastability and markov state models in molecular dynamics: modeling, analysis, algorithmic approaches*, Vol. 24 (American Mathematical Soc., 2013) (cit. on p. 11).

[147] G. M. Torrie and J. P. Valleau, "Nonphysical sampling distributions in Monte Carlo free-energy estimation: Umbrella sampling", J. Comput. Phys. **23**, 187–199 (1977) (cit. on p. 11).

[148] N. Metropolis, A. W. Rosenbluth, M. N. Rosenbluth, A. H. Teller, and E. Teller, "Equation of State Calculations by Fast Computing Machines", J. Chem. Phys. **21**, 1087–1092 (1953) (cit. on p. 11).

[149] R. Swendsen and J. Wang, "Replica monte carlo simulation of spin glasses.", Phys. Rev. Lett. **57**, 2607–2609 (1986) (cit. on p. 11).

[150] R. J. Sadus, *Molecular simulation of fluids* (Elsevier, 2002) (cit. on pp. 12, 13).

[151] J. E. Jones, *On the determination of molecular fields.—ii. from the equation of state of a gas*, Vol. 106, 738 (The Royal Society London, 1924), pp. 463–477 (cit. on p. 12).

[152] T. Werder, J. H. Walther, R. L. Jaffe, T. Halicioglu, F. Noca, and P. Koumoutsakos, "Molecular Dynamics Simulation of Contact Angles of Water Droplets in Carbon Nanotubes", Nano Lett. **1**, 697–702 (2001) (cit. on p. 12).

[153] E. R. Cruz-Chu, A. Aksimentiev, and K. Schulten, "Water-silica force field for simulating nanodevices", J. Phys. Chem. B **110**, 21497–21508 (2006) (cit. on p. 12).

[154] E. Voloshina, D. Usvyat, M. Schütz, Y. Dedkov, and B. Paulus, "On the physisorption of water on graphene: a ccsd(t) study.", Phys. Chem. Chem. Phys. **13**, 12041–12047 (2011) (cit. on pp. 12, 91).

[155] T. Darden, D. York, and L. Pedersen, "Particle mesh ewald: an n·log(n) method for ewald sums in large systems", J. Chem. Phys. **98**, 10089–10092 (1993) (cit. on pp. 13, 15).

[156] W. F.v. G. H. J. C. Berendsen, J. P. M. Postma and J. Hermans, "Interactionmodelsforwaterinrelationtoproteinhydration", Intermol. Forces, 331 (1981) (cit. on p. 13).

[157] W. L. Jorgensen, J. Chandrasekhar, J. D. Madura, R. W. Impey, and M. L. Klein, "Comparison of simple potential functions for simulating liquid water", J. Chem. Phys. **79**, 926 (1983) (cit. on pp. 13, 16).

[158] L. Woodcock, "Isothermal molecular dynamics calculations for liquid salts", Chem. Phys. Lett. **10**, 257–261 (1971) (cit. on p. 14).

[159] H. J. C. Berendsen, J. P. M. Postma, W. F. van Gunsteren, A. DiNola, and J. R. Haak, "Molecular dynamics with coupling to an external bath", J. Chem. Phys. **81**, 3684–3690 (1984) (cit. on pp. 14–16).

[160] S. Nosé, "A molecular dynamics method for simulations in the canonical ensemble", Mol. Phys. **52**, 255–268 (1984) (cit. on pp. 14, 16).

[161] W. G. Hoover, "Canonical dynamics: equilibrium phase-space distributions", Phys. Rev. A **31**, 1695–1697 (1985) (cit. on pp. 14, 16).

[162] M. Parrinello and A. Rahman, "Polymorphic transitions in single crystals: a new molecular dynamics method", J. Appl. Phys. **52**, 7182–7190 (1981) (cit. on pp. 14, 16).

[163] S. Nosé and M. L. Klein, "Constant pressure molecular dynamics for molecular systems", Mol. Phys. **50**, 1055–1076 (1983) (cit. on pp. 14, 15).

[164] M. Parrinello and A. Rahman, "Polymorphic transitions in single crystals: A new molecular dynamics method", J. Appl. Phys. **52**, 7182–7190 (1981) (cit. on p. 14).

[165] D. Van Der Spoel, E. Lindahl, B. Hess, G. Groenhof, A. E. Mark, and H. J. Berendsen, *Gromacs: fast, flexible, and free*, Vol. 26, 16 (Wiley Online Library, 2005), pp. 1701–1718 (cit. on p. 15).

[166] M. Allen and D. Tildesley, *Computer simulation of liquids oxford university press oxford 385* (1987) (cit. on p. 15).

[167] B. Hess, C. Kutzner, D. van der Spoel, and E. Lindahl, "Gromacs 4: algorithms for highly efficient, load-balanced, and scalable molecular simulation", J. Chem. Theory Comput. **4**, 435–447 (2008) (cit. on pp. 15–17).

[168] U. Essmann, L. Perera, M. L. Berkowitz, T. Darden, H. Lee, and L. G. Pedersen, "A smooth particle mesh ewald method", J. Chem. Phys. **103**, 8577 (1995) (cit. on p. 15).

[169] G. Bussi, D. Donadio, and M. Parrinello, "Canonical sampling through velocity rescaling.", J. Chem. Phys. **126**, 014101 (2007) (cit. on pp. 15, 16).

[170] S. Miyamoto and P. A. Kollman, "Settle: an analytical version of the shake and rattle algorithm for rigid water models", J. Comput. Chem. **13**, 952–962 (1992) (cit. on p. 15).

[171] M Kaukonen, A Gulans, P Havu, and E Kauppinen, "Lennard-jones parameters for small diameter carbon nanotubes and water for molecular mechanics simulations from van der waals density functional calculations.", J. Comput. Chem. **33**, 652–658 (2012) (cit. on p. 91).

[172] J. Kleis, E. Schröder, and P. Hyldgaard, "Nature and strength of bonding in a crystal of semiconducting nanotubes: van der waals density functional calculations and analytical results", Phys. Rev. B - Condens. Matter Mater. Phys. **77**, 1–10 (2008) (cit. on p. 91).

[173] A. Gulans, M. J. Puska, and R. M. Nieminen, "Linear-scaling self-consistent implementation of the van der waals density functional", Phys. Rev. B - Condens. Matter Mater. Phys. **79**, 1–4 (2009) (cit. on p. 91).

[174] A. Alexiadis and S. Kassinos, "The density of water in carbon nanotubes", Chem. Eng. Sci. **63**, 2047–2056 (2008) (cit. on p. 91).

[175] M. Kaukonen, A. Gulans, P. Havu, and E. Kauppinen, "Lennard-jones parameters for small diameter carbon nanotubes and water for molecular mechanics simulations from van der waals density functional calculations", J. Comput. Chem. **33**, 652–658 (2012) (cit. on p. 91).

[176] K. V. Agrawal, S. Shimizu, L. W. Drahushuk, D. Kilcoyne, and M. S. Strano, "Observation of extreme phase transition temperatures of water confined inside isolated carbon nanotubes", Nat. Nanotechnol. **12**, 267–273 (2017) (cit. on pp. 94, 96).

[177] R. H. Tunuguntla, F. I. Allen, K. Kim, A. Belliveau, and A. Noy, "Ultrafast proton transport in sub-1-nm diameter carbon nanotube porins", Nat. Nanotechnol. **11**, 639–644 (2016) (cit. on p. 96).

[178] P. Atkins, *Molecules in motion: ion transport and molecular diffusion* (1978), pp. 819–848 (cit. on p. 100).

[179] U. Raviv, P. Laurat, and J. Klein, "Fluidity of water confined to subnanometre films", Nature **413**, 51–54 (2001) (cit. on p. 103).

[180] D. G. Levitt, "Dynamics of a single-file pore: Non-fickian behavior", Phys. Rev. A **8**, 3050–3054 (1973) (cit. on p. 103).

[181] K.-D. Kreuer, S. J. Paddison, E. Spohr, and M. Schuster, "Transport in Proton Conductors for Fuel-Cell Applications: Simulations, Elementary Reactions, and Phenomenology", Chem. Rev. **104**, 4637–4678 (2004) (cit. on p. 103).

[182] K. Gethard, O. Sae-Khow, and S. Mitra, "Water desalination using carbon-nanotube-enhanced membrane distillation", ACS Appl. Mater. Interfaces **3**, 110–114 (2011) (cit. on p. 103).

Acknowledgement

Firstly, I would like to express my sincerest thanks to my supervisor, PD. Dr. Burkhard Schmidt, for giving me this valuable chance to study abroad for a meaningful project. He is always patient to answer all my questions and provides many great discussions and coorperations.

Secondly, I would like to give my much thanks to Prof. Dr. Beate Paulus for her kind support and make it possible to register in her group. I am also very appreciate that she gave me many support for attending international conference.

I am also very grateful for the financial support from the China Scholarship Council.

I would also like to thank all my group memebrs and all my friends in Berlin for their kind help and accompany during my happy and hard time. Special thanks to Jun Zhang, Chunmei Liu, Marjan S. Mirahmadi, Wei Zhang, Chenglie Han, Stefan Rüdrich and Randolf Altmeyer for their help in creating my thesis.

Finally, I would like to thank my dear parents for their endless love, and especially to my lover - Shulai for his always understanding and supportive. In particularly, I am very happy to have a little sunny boy. He brings me lots of happiness to be a mother and makes my life in Berlin memorable.